From a causal representation of multiloop scattering amplitudes to quantum computing in the Loop-Tree Duality

Thesis submitted for the Degree of Doctor of Physics

Author:

Norma Selomit Ramírez Uribe

Directors:

Germán V. Rodrigo García
German F. R. Sborlini
Roger J. Hernández Pinto

Universitat de València

3126 Programa de Doctorat en Física

Instituto de Física Corpuscular, Departament de Física Teòrica
Universitat de València – Consejo Superior de Investigaciones Científicas

January 2023

Declaration of authorship

I, Norma Selomit Ramírez Uribe, hereby certify that this thesis, titled *From a causal representation of multiloop scattering amplitudes to quantum computing in the Loop-Tree Duality*, has been composed by myself. All the work contained herein is my own except where explicitly stated otherwise, and all main sources of help have been properly referenced and acknowledged.

The work presented in this thesis is based on original results previously published by myself, in collaboration with Germán Rodrigo, German F. R. Sborlini, Roger J. Hernández-Pinto, William J. Torres Bobadilla, J. Jesús Aguilera-Verdugo, Andrés E. Rentería-Olivo, Luiz Vale Silva, Judith Plenter, Félix Driencourt-Mangin, Szymon Tracz, Giuseppe Clemente, Arianna Crippa and Karl Jansen. Chapters 4, 5, 6 and 7, in particular, are based on the following publications:

Articles

[1] S. Ramírez-Uribe, R. J. Hernández-Pinto, G. Rodrigo and G. F. R. Sborlini, *From five-loop scattering amplitudes to open trees with the Loop-Tree Duality*, *Symmetry* **14** (2022)[2211.03163].

[2] G. Clemente, A. Crippa, K. Jansen, S. Ramírez-Uribe, A. E. Rentería-Olivo, G. Rodrigo, G. F. R. Sborlini and L. Vale Silva, *Variational quantum eigensolver for causal loop Feynman diagrams and acyclic directed graphs*, [2210.13240].

[3] S. Ramírez-Uribe, A. E. Rentería-Olivo, G. Rodrigo, G. F. R. Sborlini and L. Vale Silva, *Quantum algorithm for Feynman loop integrals*, *JHEP* **05** (2022) 100, [2105.08703].

[4] J. Aguilera-Verdugo et al., *A Stroll through the Loop-Tree Duality*,

Symmetry **13** (2021) 1029, [2104.14621].

[5] S. Ramírez-Uribe, R. J. Hernández-Pinto, G. Rodrigo, G. F. R. Sborlini and W. J. Torres Bobadilla, *Universal opening of four-loop scattering amplitudes to trees*, *JHEP* **04** (2021) 129, [2006.13818].

[6] J. J. Aguilera-Verdugo, F. Driencourt-Mangin, R. J. Hernández-Pinto, J. Plenter, S. Ramirez-Uribe, A. E. Renteria Olivo et al., *Open Loop Amplitudes and Causality to All Orders and Powers from the Loop-Tree Duality*, *Phys. Rev. Lett.* **124** (2020) 211602, [2001.03564].

[7] J. J. Aguilera-Verdugo, F. Driencourt-Mangin, J. Plenter,S. Ramírez-Uribe, G. Rodrigo, G. F. R. Sborlini et al., *Causality, unitarity thresholds, anomalous thresholds and infrared singularities from the loop-tree duality at higher orders*, *JHEP* **12** (2019) 163, [1904.08389].

[8] FCC collaboration, A. Abada et al., *HE-LHC: The High-Energy Large Hadron Collider: Future Circular Collider Conceptual Design Report Volume 4*, *Eur. Phys. J. ST* **228** (2019) no.5, 1109-1382.

[9] FCC collaboration, A. Abada et al., *FCC-hh: FCC-hh: The Hadron Collider: Future Circular Collider Conceptual Design Report Volume 3*, *Eur. Phys. J. ST* **228** (2019) no.4, 755-1107.

[10] FCC collaboration, A. Abada et al., *FCC-ee: The Lepton Collider: Future Circular Collider Conceptual Design Report Volume 2*, *Eur. Phys. J. ST* **228** (2019) no.2, 261-623.

[11] FCC collaboration, A. Abada et al., *FCC Physics Opportunities: Future Circular Collider Conceptual Design Report Volume 1*, *Eur. Phys. J. C* **79** (2019) 474.

Proceedings

[12] S. Ramírez-Uribe, *Quantum algorithm for querying causality of multi-loop scattering amplitudes*, *Pos* ICHEP2022 (11, 2022), 418, [2211.05487].

[13] S. Ramírez-Uribe, R. J. Hernández-Pinto, A. E. Rentería-Olivo, G. Rodrigo, G. F. R. Sborlini, W. J. T. Bobadilla and L. V. Silva, *Four-loop scattering amplitudes journey into the forest*, *Pos* EPS-HEP2021 (2022), 732, [2110.10605].

[14] S. R. Uribe, *Four-loop scattering amplitudes through the loop-tree duality*, *Rev. Mex. Fis. Suppl.* **3** (2022) no.2, 020720, [2112.05584].

[15] S. Ramírez-Uribe, *From Causal Representation of Multiloop Scattering Amplitudes to Quantum Computing*, *Acta Phys. Polon. Supp.* **15** (2022) no.2, 1, [2201.04381].

[16] A. Blondel, J. Gluza, S. Jadach, P. Janot, T. Riemann, S. Abreu, J. J. Aguilera-Verdugo, A. B. Arbuzov, J. Baglio and S. D. Bakshi, *et al.*, *Theory for the FCC-ee: Report on the 11th FCC-ee Workshop Theory and Experiments*, *CERN* (2020) ISBN 978-92-9083-560-8, 978-92-9083-559-2, [1905.05078].

[17] J. J. Aguilera-Verdugo, F. Driencourt-Mangin, J. Plenter, S. Ramírez-Uribe, G. Rodrigo, G. F. R. Sborlini, W. J. Torres Bobadilla and S. Tracz, *Unsubtractions at NNLO*, *CERN Yellow Reports: Monographs* **3** (2020), 169-176.

[18] N. Selomit Ramírez-Uribe, R. J. Hernández-Pinto and G. Rodrigo, *QED and QCD self-energy corrections through the loop-tree duality*, *J. Phys. Conf. Ser.* **912**(2017) no.1, 012013, [1709.07802].

Different talks about the topic were also given at the following conferences:

- CPAN 2022, *National Centre for Particle, Astroparticle and Nuclear Physics*, Bilbao (Spain), November 2022.
- ICHEP 2022, *International Conference on High Energy Physics*, Bologna (Italy), July 2022.
- @FlipPhysics, *Flip Physics Workshop*, Valencia (Spain), March 2022.
- Matter To The Depeest, *Matter To The Deepest Recent Developments In Physics Of Fundamental Interactions XLIV International Conference of Theoretical Physics*, Online conference, September 2021.
- XIX MSPF, *XIX Mexican School of Particles and Fields*, Online conference, August 2021.

- EPS-HEP 2021, *European Physical Society conference on high energy physics 2021*, Online conference, July 2021.
- PARTICLEFACE 2021, *Working Group Meeting and MC Meeting of the COST Action CA16201*, Zagreb (Croatia), July 2021.
- *5to Congreso Internacional de Física, Matemáticas y Electrónica*, Culiacán (México), October 2020.
- PARTICLEFACE 2020, *Working Group Meeting and MC Meeting of the COST Action CA16201*, Kraców (Poland), February 2020.

Abstract

The perturbative approach to Quantum Field Theories has successfully provided incredibly accurate theoretical predictions in high-energy physics. Despite the development of several techniques to boost the efficiency of these calculations, some ingredients remain a hard bottleneck. This is the case of multiloop scattering amplitudes, describing the quantum fluctuations at high-energy scattering processes. The Loop-Tree Duality (LTD) is a novel method aimed to overcome these difficulties by opening the loop amplitudes into connected tree-level diagrams. In this thesis we present three core achievements: the reformulation of the Loop-Tree Duality to all orders in the perturbative expansion, a general methodology to obtain LTD expressions which are manifestly causal, and the first flagship application of a quantum algorithm to Feynman loop integrals. The proposed strategy to implement the LTD framework consists in the iterated application of the Cauchy's residue theorem to a series of mutiloop topologies with arbitrary internal configurations. We derive a LTD representation exhibiting a factorized cascade form in terms of simpler subtopologies characterized by a well-known causal behaviour. Moreover, through a clever approach we extract analytic dual representations that are explicitly free of noncausal singularities. These properties enable to open any scattering amplitude of up to five loops in a factorized form, with a better numerical stability than in other representations due to the absence of noncausal singularities. Last but not least, we establish the connection between Feynman loop integrals and quantum computing by encoding the two on-shell states of a Feynman propagator through the two states of a qubit. We propose a modified Grover's quantum algorithm to unfold the causal singular configurations of multiloop Feynman diagrams used to bootstrap the causal LTD representation of multiloop topologies.

Resumen

La teoría cuántica de campos con enfoque perturbativo ha logrado de manera exitosa proporcionar predicciones teóricas increíblemente precisas en física de altas energías. A pesar del desarrollo de diversas técnicas con el objetivo de incrementar la eficiencia de estos cálculos, algunos ingredientes continuan siendo un verdadero reto. Este es el caso de las amplitudes de dispersión con lazos múltiples, las cuales describen las fluctuaciones cuánticas en los procesos de dispersión a altas energías. La Dualidad Lazo-Árbol (LTD) es un método innovador, propuesto con el objetivo de afrontar estas dificultades abriendo las amplitudes de lazo a amplitudes conectadas de tipo árbol. En esta tesis presentamos tres logros fundamentales: la reformulación de la Dualidad Lazo-Árbol a todos los órdenes en la expansión perturbativa, una metodología general para obtener expresiones LTD con un comportamiento manifiestamente causal, y la primera aplicación de un algoritmo cuántico a integrales de lazo de Feynman. El cambio de estrategia propuesto para implementar la metodología LTD, consiste en la aplicación iterada del teorema del residuo de Cauchy a un conjunto de topologías con lazos múltiples y configuraciones internas arbitrarias. La representación LTD que se obtiene, sigue una estructura factorizada en términos de subtopologías más simples, caracterizada por un comportamiento causal bien conocido. Además, a través de un proceso avanzado desarrollamos representaciones duales analíticas explícitamente libres de singularidades no causales. Estas propiedades permiten escribir cualquier amplitud de dispersión, hasta cinco lazos, de forma factorizada con una mejor estabilidad numérica en comparación con otras representaciones, debido a la ausencia de singularidades no causales. Por último, establecemos la conexión entre las integrales de lazo de Feynman y la computación cuántica, mediante la asociación de los dos estados sobre la capa de masas de un propagador de Feynman con los dos estados de un qubit. Proponemos una modificación del algoritmo cuántico de Grover para encontrar las configuraciones singulares causales de los diagramas de Feynman con lazos múltiples. Estas configuraciones son requeridas para establecer la representación causal de topologías con lazos múltiples.

Resum

L'enfocament pertorbatiu de la teoria quàntica de camps ha aconseguit proporcionar prediccions teòriques increïblement precises en física d'altes energies. Malgrat el desenvolupament de diverses tècniques amb l'objectiu d'incrementar l'eficiència d'aquests càlculs, alguns ingredients continuen sent un vertader repte. Aquest és el cas de les amplituds de dispersió amb llaços múltiples, les quals descriuen les fluctuacions quàntiques en processos de dispersió a altes energies. La dualitat llaç-arbre (LTD en anglés), és un mètode innovador, que té com a objectiu afrontar aquestes dificultats obrint les amplituds de llaç a amplituds connectades de tipus arbre. En aquesta tesi presentem tres èxits fonamentals: la reformulació de la dualitat llaç-arbre a tots els ordres en l'expansió pertorbativa, una metodologia general per obtenir expressions LTD manifestament causals, i la primera aplicació d'un algoritme quàntic a integrals de llaç de Feynman. El canvi d'estratègia proposat per implementar la metodologia LTD consisteix en l'aplicació iterada del teorema del residu de Cauchy a un conjunt de topologies amb llaços múltiples i configuracions internes arbitràries. Així obtenim una representació LTD que segueix una estructura factoritzada en termes de subtopologies més senzilles, caracteritzada per un comportament causal ben conegut. A més, mitjançant un procés avançat desenvolupem representacions duals analítiques explícitament lliures de singularitats no causals. Aquestes propietats fan possible obrir qualsevol amplitud de dispersió de fins a cinc llaços, d'una forma factoritzada, amb millor estabilitat numèrica que en altres representacions, gracies a l'absència de singularitats no causals. Finalment, establim la connexió entre les integrals de llaç de Feynman i la computació quàntica associant els dos estats on-shell d'un propagador de Feynman amb els dos estats d'un qbit. Proposem una modificació de l'algoritme quàntic de Grover per trobar les configuracions singulars causals dels diagrames de Feynman amb llaços múltiples. Aquestes configuracions són necessàries per a establir la representació causal de topologies amb llaços múltiples.

Acknowledgements

The experiences that I have gained from doing this PhD are much more than I could have ever imagined, not just in an academic sense but also personal. It is true that it has been required a great effort of my part and that the conquests I have achieved are not few, but to be honest, this do not belong to me only. Honour to whom honour is due, I want to thank those who have been supporting me in one way or another.

I can not start the following lines with any one else, Germán Rodrigo, not just a brilliant and dedicated scientific but also a caring person. I am aware that not many people has the opportunity to work under the guidance of a patient and supportive person. Thank you very much *Big Boss*, you are a model to follow, you teach with facts not just with words. In that very same direction, I am very grateful to my co-directors (more than that, friends) for all the academic support, but most of all, for always reminding me that the results are just a matter of keep working and time.

This would certainly not have been possible without the constant financial support provided for Consejo Nacional de Ciencia y Tecnología and Universidad Autónoma de Sinaloa. Additionally, the economical support of the following projects allowed me to participate on schools, workshops, conferences and academic stays: MCIN/AEI/10.13039/501100011033, Grants No. PID2020-114473GB-I00 and FPA2017-84445-P, COST Action CA16201 PARTICLEFACE, and Project No. A1- S-33202 (Ciencia Básica).

I would like to continue by thanking all my dear friends. To all of them who, even at distance, always made me feel their presence, never letting me forget that they were waiting for my return to the very same side of the lake. And what can I say about those who over the course of more than four years, shared the day-to-day of a life in Valencia. Honestly, I could thank

them for so many things, but on this occasion I just want to let them know the most important one: you have become to me friends for life.

Last but clearly not least, my family. Anyone who knows me a little bit is aware that an essential piece of my life is my family, my four angels and attachments. I do not need more than one memory of them to immediately smile. Thank you for always being patient with me, I know there have been times when I have not been the most cordial and understanding person; for supporting my decisions even without agreeing, in a four words summary ... thank you for all.

Contents

Chapter 1

Introduction

The impressive evolution in recent years in the understanding of the fundamental interactions and components of Nature is due to the feasibility to obtain accurate theoretical predictions from Quantum Field Theories (QFT). Precision modelling in particle physics relies mostly on perturbative frameworks, which have proven a remarkable efficiency for that purpose. However, the ongoing effort to evolve towards higher perturbative orders with the aim of obtaining more accurate predictions has uncovered challenging tasks.

The main bottleneck in perturbative Quantum Field Theory is the description of quantum fluctuations in high-energy scattering processes by the calculation of multiloop and multileg scattering amplitudes. The intrinsic mathematical structure in Feynman loop diagrams exhibit a complex behaviour of physical and unphysical singularities, preventing a straightforward numerical calculation. Regarding experimental scenarios, the rigorous demands that high-energy physics will meet in the Run 3 of the CERN's Large Hadron Collider (LHC) [19], the forthcoming high-luminosity phase [20], and the planned future colliders [8–11,16,21–24] are pushing the precision frontier towards even more accurate theoretical predictions and a better understanding of the behaviour of such quantum objects.

Proper treatment of singularities is required to achieve a robust numerical evaluation of integrals at multiloop level. In accordance with this need there has been a remarkable effort in the field to provide suitable frameworks [25] to deal with this challenge. However, the work is far from finished; new methodologies and strategies are needed to confront the theoretical preci-

sion required at high-energy colliders. In order to address these demands, this thesis delves into a novel framework which opens any loop diagram into a sum of connected tree-level diagrams, and explores alternative approaches to provide suitable and more comprehensive solutions.

1.1 Outline of the thesis

The content of this thesis is structured as follows. In Chapter 2 we start with a brief overview of the most astonishing discoveries in particle physics and some fundamental aspects of the theory behind them. We present the ingredients needed to bind together the representation of a cross section and the description of the general procedure to address the calculation of it through a perturbative approach. We close the chapter highlighting the problem due to the arising of singularities in the process. Moving to Chapter 3, the assembly of the most relevant features of the Loop-Tree Duality (LTD) methodology is reviewed, specially those related with the singular structure of loop integrals and scattering amplitudes. Besides, we present some important applications developed through a LTD scenario supporting the computation of physical processes. In Chapter 4 we introduce the generalization of the LTD framework to all perturbative orders. The methodology is applied to selected multiloop topologies with arbitrary internal configurations up to three loops, writing the associated LTD representation in terms of simpler subtopologies. Furthermore, we show their implicit singular structure in the LTD scenario has a remarkable feature, the LTD representation is manifestly free of noncausal singularities. In Chapters 5 and 6, we continue with the study of the next multiloop topology in complexity. The LTD framework is applied to the topologies appearing for the first time at four and five loops respectively. The first flagship application of a quantum algorithm to Feynman loop integrals is presented in Chapter 7. Explicitly, we develop two quantum algorithms based in a suitable modification of Grover's quantum algorithm used to unfold the causal singular configuration of multiloop Feynman diagrams. The first proposal is characterised by comparing adjacent propagators through the use of binary clauses, whereas the second one manages to make the comparison without binary clauses. Finally, the work exposed in this thesis is summarised in Chapter 8. Also, we mention an important upcoming project related with the computation of physical cross section, which has been motivated by the knowledge acquired through the work developed in this thesis.

Chapter 2

Theory behind particle physics

Before we dive into the theoretical foundation supporting particle physics, I want us to take a pause and reassemble some of the most memorable discoveries that have allowed us to reach the state of the art of particle physics. It is admirable when we realize that the trigger for all these events has been the desire to answer one single question: the most innocent and fundamental question in science that revolutionised the way of seeing, and understanding all that surrounds us ...

What is matter made of?

This following section provides a historical journey [26] through the field of elementary particle physics, taking as a start point the discovery of the electron and closing with the long awaited discovery of the Higgs boson.

2.1 A glimpse of Particle Physics

Let us start with the first piece in the puzzle of the fundamental blocks to describe nature; the discovery of the electron made its appearance in 1887 through the study of cathode ray properties by J. J. Thomson. The turn of the first proton observation was in 1898 by W. Wien in streams of ionized gas, nevertheless, it was not until 1920 that Rutherford postulated the hydrogen nucleus to be a new particle, which he called proton. Following

with the final piece in what is known as the classical period (1987-1932) in elementary particle physics, the neutron was theoretically predicted in 1920 by E. Rutherford, given the name in 1921 by W. D. Harkins, proposed by S. A. de Mayolo in 1924 and, finally discovered and documented in the paper "Possible existence of the neutron" by J. Chadwick in 1932 [27].

In the early 1930s, P. A. M. Dirac formulated the first relativistic theory [28] describing the interaction of photons with matter, which was the base for what is known today as Quantum Electrodynamics (QED). In the same period, W. Pauli postulated the existence of neutrinos to compensate the apparent loss of energy and linear momentum in the β decay of neutrons. A generalization of Dirac formulation was introduced by E. Fermi in 1933 [29], where the β decay was included by incorporating the neutron and neutrino into the original model.

The first significant theory of the strong force was proposed in 1934 by H. Yukawa [30], who interpreted the short range of the strong interactions in terms of the exchange particles with mass. In 1937, a massive elementary particle was discovered in cosmic rays, but based on Yukawa's conjecture it interacted too weakly with the nuclei to be the strong force mediator. The particle found was the muon (μ) [31], the first member of the second family of elementary particles. The rest of the decade was spent confronting

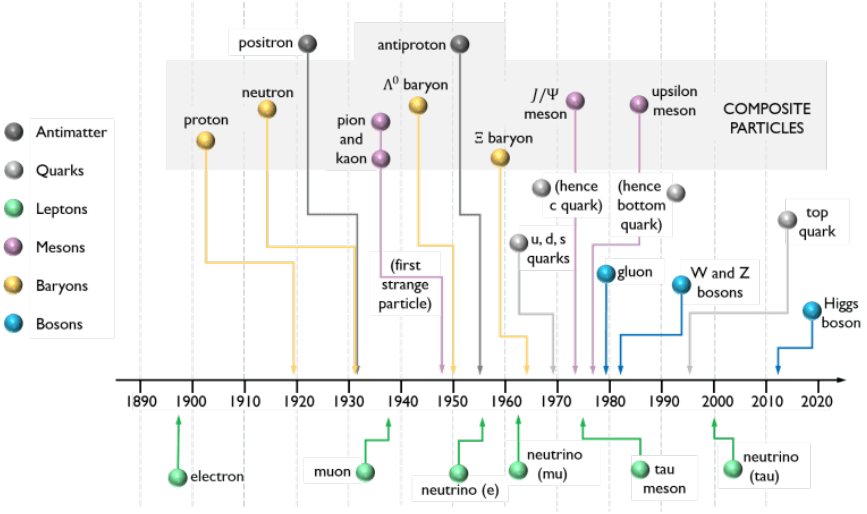

Figure 2.1: Timeline of particle discoveries. Image: sciencebydegrees.com.

the theoretical difficulties associated with QED, ending with the remarkable suggestion of O. Klein of gauge theories as the core cause of β decay.

During the decade of 1940s, R. Feynman, J. Schwinger, and S. Tomonaga, proposed the understanding of the computational rules of QED in terms of renormalization, allowing to deal with divergences that arise through the calculation of perturbative contributions in QED. This approach was generalised by F. Dyson in 1949 [32] and supported by astonishing evidence provided by calculations and measurements of the anomalous magnetic moment of the electron and the Lamb shift. The particle that Yukawa proposed was discovered in 1947, the π meson. That very same year, a heavier meson decaying into two pions was discovered by C. Butler and G. Rochester [33], the K meson.

The lambda particle, Λ, was discovered in 1950 by V. D. Hopper and S. Biswas [34]. Experiments showed that its production was much faster than its decay, suggesting that the mechanism behind each process did not follow the same nature. This fact provided evidence of a new kind of interaction, currently called the weak force. This particle would be the first of the new strongly-interaction particles having two main features: always produced in pairs and with a slow decay rate. These properties were interpreted by M. Gell-Mann [35] as evidence of a new quantum number, strangeness. In early 1954, C. N. Yang and R. L. Mills extended the concept of the electromagnetic $U(1)$ gauge theory to non-Abelian groups [36] to provide an explanation for strong interactions.

Moving on to the second half of the decade, the Pauli conjecture was verified with the neutrino detection [37] in 1956 by C. Cowan and F. Reines at the Savannah River fission reactor. Experiments to test parity violation by the weak interactions were proposed [38] by T. D. Lee and C. N. Yang. In 1956 the experimental validation was conducted by C. S. Wu and by V. Telegdi who observed an asymmetry indicating parity violation. At the very begining of the following year, F. Marshak and E. C. G. Sudarshan identified the source of parity violation in terms of the $V - A$ vector and axial vector interactions [39]; the idea was supported and also published by R. Feynman and M. Gell-Mann [40]. Encouraged by the work of C. N. Yang and R. L. Mills, theorists soon realized the possibility that weak interactions could be caused by a new massive vector particle, the W-boson.

The decade of 1960 started with the appearance of $SU(3)$ in the Physics world: Y. Ne'eman and M. Gell-Mann organized the strongly interacting particles in terms of this symmetry group [41]. Based on this classification, in 1964 M. Gell-Mann [42] and also G. Zweig [43] postulated the existence of three elementary fermionic constituents: the up, down, and strange quarks as the building blocks of baryonic matter. In that very same year Y. Nambu proposed that quarks interact with one another through a $SU(3)$ Yang-Mills theory. The beginning of this decade also witnessed the notion of spontaneous symmetry breaking in elementary particle physics, first introduced by Y. Nambu and generalized by J. Goldstone. This idea allowed to understand the pions as the approximate Nambu–Goldstone bosons of spontaneously broken axial-vector symmetries associated with the masslessness of quarks. Shortly afterwards, P. W. Higgs, R. Brout and F. Englert showed that the spontaneous breaking of gauge symmetries generates massive gauge bosons from massless ones. The extension to the Gell-Mann–Zweig model was proposed less than a year later. In 1964 S. Glashow and J. Bjorken introduced for the first time the idea of a fourth quark flavor [44], calling it charm; this modification allowed a better description of the weak interaction.

Some of the developments of that decade motivated and enabled the emergence of the electroweak formulation in its modern form. J. Schwinger was the first to suggest an electroweak gauge theory [45], an $SU(2)$ gauge group spontaneously broken to electromagnetic $U(1)$ at long distances. This model was extended by S. Glashow [46] by including a short range neutral current, the Z boson; the resulting symmetry structure proposed forms the basis of the accepted theory of the electroweak interactions. In 1964, A. Salam and J. C. Ward worked on a gauge theory for the weak and electromagnetic interactions, subsequently obtaining $SU(2) \times U(1)$ model [47]. A. Salam was convinced that all the elementary particle interactions were actually gauge interactions. Finally in 1967, S. Weinberg proposed a model of unification of electromagnetism and nuclear weak forces with the masses of the force-carriers of the weak part of the interaction being explained by spontaneous symmetry breaking [48]. All these works gave rise to a model of electroweak lepton interactions, which after spontaneous electroweak symmetry breaking, reduces to QED.

Regarding experimental achievements, in 1962 G. Danby et al. showed the existence of a non-electron type of neutrino [49], the muon neutrino. In 1964 J. Cronin and V. Fitch examined the decay of K-mesons particles [50]

whose result violated the symmetry between matter and antimatter; the phenomenon of CP violation was discovered. At the end of the decade, Bjorken discovered what is known as light-cone scaling [51], a phenomenon in the deep inelastic scattering of hadrons. Experimentally observed hadrons behave as collections of virtually independent point-like constituents when probed at high energies; this observation was critical to the recognition of quarks as actual elementary particles.

In 1970, S. Glashow, J. Iliopoulos and L. Maiani introduced the so-called "GIM mechanism" [52], recalling the idea of the charm quark, they presented a specific prediction of the existence of this new elementary particle. This particle could explain the absence of flavor-changing neutral interactions, adding theoretical evidence for a second family. This is followed by the achievement of G. t'Hooft (at that time PhD candidate under the supervision of M. Veltman), showing that the Glashow-Salam-Weinberg model was in fact renormalizable [53]. In 1972 there was demonstrated, by C. Bouchiat, J. Iliopoulos and P. Meyer, that the mathematical coherence of the Standard Model required symmetry between quarks and leptons to cancel the anomalies in axial symmetries constraints. The concept of colour charge quantum number was introduced by M. Gell-Mann and H. Fritzsch [54], allowing the understanding of the decay rate of pions. In 1973, H. Fritzsch and H. Leutwyler in collaboration with M. Gell-Mann formulated the modern version of quark dynamics: Quantum Chromodynamics [55].

The phenomenon of asymptotic freedom had been observed in different scenarios: in quantum electrodynamics with a charged vector field by V.S. Vanyashin and M.V. Terent'ev in 1965, in Yang–Mills theory by I. Khriplovich in 1969, and by G. 't Hooft in 1972. Nevertheless, it was not until 1973 with the discovery of asymptotic freedom in QCD by D. Gross, F. Wilczek and D. Politzer [56, 57], that its physical significance was understood, explaining the remarkable scaling results found by experiments in the late sixties. This showed that all interactions, strong, weak and electromagnetic, could be explained with Yang-Mills vector exchange theories.

In 1973, M. Kobayashi and T. Maskawa anticipated the requirement of at least three generations of quarks and, as implication of the existence of a third generation, CP-violation [58]. The prediction of the third family was confirmed experimentally in 1977 by the discovery of the bottom quark at Fermilab by Leon M. Lederman. The year of 1973 also witnessed

Gargamelle Collaboration presenting the first direct evidence of the weak neutral current [59], considered a crucial experimental support for the unification of electromagnetic and weak interactions in electroweak theory. The first two families of elementary particles were completed in 1974, by the discovery of the J/Ψ charmed quark-antiquark bound state at Brookhaven and SLAC. Furthermore, in 1975 M. Perl discovered the τ [60], the lepton member of the third family. Related to the parity structure of the neutral current, in 1978 parity-violation in the neutral currents was discovered in electron-nucleon scattering at SLAC [61, 62]. By the end of the decade, the final formulation of the Standard Model was generally accepted as the paradigm of elementary particle physics. Nevertheless, the work was not finished since many of the Standard Model's predictions were still waiting to be observed.

The decade of the 1980's started with the discovery of the electroweak gauge bosons, the charged W [63] and the neutral Z [64] bosons at CERN. With these findings, the Large Electron-Positron collider at CERN was used as a W and Z factory to extensively test the Standard Model, providing important evidence to support the assumption of the existence of three families only. The rest of the decade was focused on experimental validation of the Standard Model and on the search for the three remaining particles predicted, the top quark, the tau neutrino and the Higgs boson. The last relevant report during that decade was the detection of large $B-\bar{B}$ mixing, suggesting a very heavy top quark.

Finally the top quark makes its appearance; the discovery was in 1995 by the CDF [65] and D0 [66] experiments at the Fermilab's Tevatron. Regarding the search of the tau neutrino, it required the collaboration of a group with over fourty physicists to propose an experiment designed to uniquely establish its existence. The DONUT experiment was built during the 1990's and the discovery of the tau neutrino [67] was announced in 2000 by the DONUT collaboration.

Up to this point, the Higgs boson was the last unobserved fundamental particle in the Standard Model of particle physics. Aiming for the detection of this elusive particle, the world's largest and highest-energy particle collider was built by the European Organization for Nuclear Research (CERN) between 1998 and 2008 in collaboration with over 10,000 scientists and hundreds of universities and laboratories, as well as more than 100 countries.

Finally, in 2012 CERN's Large Hadron Collider (LHC) achieved the detection of a particle compatible with the Higgs particle [68, 69]. The major question about the Higgs boson found outstanding evidence to state openly:

The Higgs mechanism could be "real"!

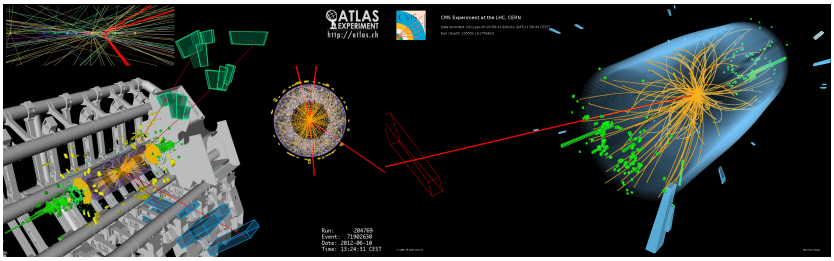

Figure 2.2: Events recorded by ATLAS (left) and CMS (right) in 2012. Image: CERN for the ATLAS and CMS collaborations.

The numerous events presented in this section would not have been possible without the close and committed collaboration between theoretical and experimental research groups. The path that Particle Physics has undertaken to its current state allowed to achieve a *new* periodic table composed by elementary particles interacting among themselves through properties of quantum fields, known as gauge invariance and symmetries. Therefore, the understanding of the subatomic world is based in this outstanding particle classification and their interactions. The most precise model to describe nature is called Standard Model which accounts for the prediction of a wide variety of phenomena and the correct interpretation of almost all experimental measurements obtained to date.

2.2 The Standard Model in detail

The Standard Model is a theory that explains with high accuracy three of the four fundamental forces of nature: the strong nuclear force, the weak nuclear force and the electromagnetic force[1]. The particle classification in this theory is structured in four groups: quarks, leptons, gauge bosons and Higgs boson. Regarding particle dynamics, the main features used to characterize them are the electric charge and the spin.

[1]There are still attempts to consistently include the gravitational force, nevertheless, fitting the description of the micro and macro world in the same framework remains a challenge.

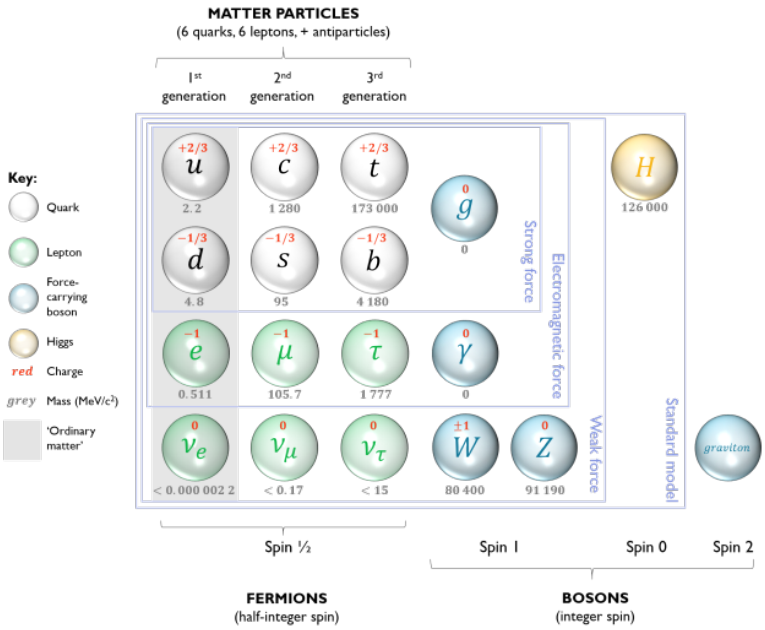

Figure 2.3: Elementary particles in the Standard Model. Image: sciencebydegrees.com.

Quarks and leptons are fermions, half-integer spin, consisting of six members (*flavors*) each and grouped in pairs called *generations*. The lightest and most stable particles compose the first generation, whereas the heavier and less stable particles represent the second and third generations. Quarks are particles affected by the strong interaction with fractional electric charge, clustered into the three generations as follows,

$$\begin{pmatrix} u \\ d \end{pmatrix}_{1^{st}}, \qquad \begin{pmatrix} c \\ s \end{pmatrix}_{2^{nd}}, \qquad \begin{pmatrix} t \\ b \end{pmatrix}_{3^{rd}}. \tag{2.1}$$

Additionally, quarks come in three different *colours* and they mix to generate colourless objects called hadrons. Leptons are affected by the electromagnetic and weak forces with integer electric charge. The three generations are distributed as follows,

$$\begin{pmatrix} e \\ \nu \end{pmatrix}_{1^{st}}, \qquad \begin{pmatrix} \mu \\ \nu_\mu \end{pmatrix}_{2^{nd}}, \qquad \begin{pmatrix} \tau \\ \nu_\tau \end{pmatrix}_{3^{rd}}, \tag{2.2}$$

where the first element of each generation, e, μ and τ have electric charge and sizeable mass, while neutrinos are electrically neutral and have a very tiny mass difficult to detect at the time.

Regarding the particles responsible for mediating the interactions, the gauge bosons are spin-1 particles which give rise to the three fundamental forces: the strong and electromagnetic forces are carried by the gluons and photons respectively, and the $W^{\pm}$ and Z bosons are the ones responsible for the weak force. The graviton, yet to be found, should be the particle responsible for the gravitational force. Last but not least, the Higgs boson is a massive scalar boson particle which accounts by generating the mass of all the particles included in the Standard Model.

Delving into the theoretical foundations of the Standard Model, this theory is based on Quantum Field Theories, a mathematical framework that combines classical field theory, special relativity and quantum mechanics. The most important QFT for describing elementary particle physics are gauge theories. The local gauge symmetry of the SM is given by

$$SU(3)_C \times SU(2)_L \times U(1)_Y \ , \tag{2.3}$$

where $SU(3)_C$ is the gauge group of the strong interaction, $SU(2)_L$ the gauge group of the weak interaction and $U(1)_Y$ the gauge group of the electromagnetic interaction. The interaction behaviour described by the Standard Model is established by imposing its Lagrangian to be invariant under any $SU(3)_C \times SU(2)_L \times U(1)_Y$ local transformation, leading to the bosons responsible for carrying the different forces, those known as gauge fields.

The first known gauge theory is Quantum Electrodynamics (QED) [70], this theory is an Abelian $U(1)$ group theory which describes the electromagnetic interaction between fermions and photons. The Lagrangian of QED obtained by imposing the invariance under a local $U(1)$ symmetry on the Lagrangian of a Dirac fermion is written as

$$\mathcal{L}_{\text{QED}} = \bar{\psi}\,(i\,\gamma^{\mu} D_{\mu} - m)\,\psi - \frac{1}{4} F_{\mu\nu}\,F^{\mu\nu} \ , \tag{2.4}$$

with ψ the fermion field. The covariant derivative denoted as D_μ is defined as

$$D_\mu = \partial_\mu - i\, eA_\mu \ , \tag{2.5}$$

where the electric charge of the fermion field is represented with e. The electromagnetic field strength tensor, $F_{\mu\nu}$, is written in terms of the gauge field A_μ as follows

$$F_{\mu\nu} = \partial_\mu A_\nu - \partial_\nu A_\mu \ , \tag{2.6}$$

with the gauge field A_μ interpreted as the photon field.

Unlike QED, Quantum Chromodynamics (QCD) is a non-Abelian $SU(3)$ gauge theory. This theory regulates the strong interactions between quarks and gluons, and the procedure to obtain the QCD Lagrangian is similar to QED, imposing the invariance on the Lagrangian under $SU(3)$ symmetry. The QCD Lagrangian reads as

$$\mathcal{L}_{\text{QCD}} = \bar{\psi}\,(i\,\gamma^\mu D_\mu - m)\,\psi - \frac{1}{4} G^a_{\mu\nu}\, G^{\mu\nu}_a \ , \tag{2.7}$$

where ψ is the quark field. The covariant derivative, D_μ, is defined as

$$D_\mu = \partial_\mu - i\, g_S\, A^a_\mu\, T_a \ , \tag{2.8}$$

with g_S standing for the strong coupling and T_a as generators in the fundamental representation. The strong field strength tensor is written as

$$G^a_{\mu\nu} = \partial_\mu A^a_\nu - \partial_\nu A^a_\mu + g_S\, f^a_{bc}\, A^b_\mu\, A^c_\nu \ , \tag{2.9}$$

where the tensor A^a_μ stands for the gluon fields which live in the adjoint representation of $SU(3)$ gauge group, and are identified with the index a. For the $SU(3)$ group there are eight generators, $\mathbf{T}^a$, where $a = \{1, \ldots, N_C^2 - 1\}$ with $N_C = 3$, therefore eight different gluon fields satisfying the following conditions,

$$\text{Tr}\left(\mathbf{T}^a \mathbf{T}^b\right) = \frac{1}{2}\delta^{ab} \qquad \text{and} \qquad \left[\mathbf{T}^a, \mathbf{T}^b\right] = i\, f^{abc} \mathbf{T}_c \ , \tag{2.10}$$

with δ^{ab} the Kronecker delta and f^{abc} the structure constants of $SU(3)$.

The implication of the specific structure from the non-Abelian theory of QCD is exhibited with the third term in the r.h.s. of Eq. (2.10), the one accountable of the origin of the gluon self-interactions. The relevance of

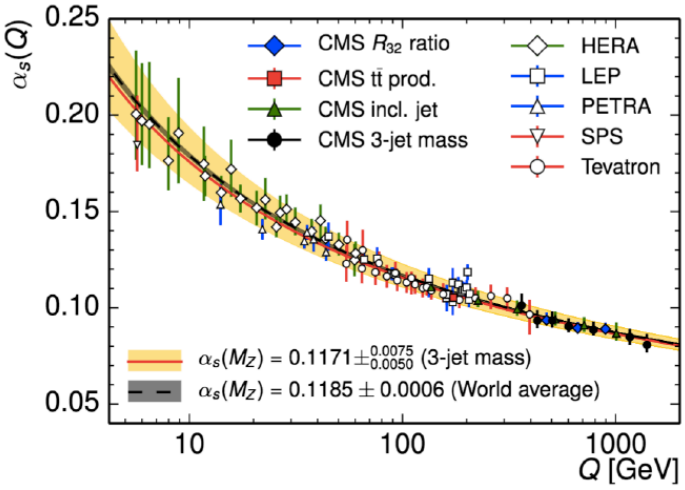

Figure 2.4: Running of the strong coupling. Plot from CERN for the CMS collaborations.

this unique feature is associated with the emergence of the two remarkable properties distinguishing QCD: *confinement* and *asymptotic freedom*. Confinement [71] occurs at low energy or long distances, and refers to the impossibility to entirely separate and isolate quarks and gluons from another hadron. From the experimental side no observations of free quarks or gluons have been reported, nevertheless, a theoretical proof is still missing. Regarding asymptotic freedom, it takes place at high energy or very short distances, where quarks and gluons behave essentially as free particles.

These two features are justified by the running of the strong coupling $\alpha_S = g_S^2/(4\pi)$, which value depends on the characteristic energy scale of the scattering process. It has been shown [72] that, the strong coupling given a reference energy scale μ_0 turns out to be

$$\alpha_S(\mu) \approx \frac{\alpha_S(\mu_0)}{1 + \alpha_S(\mu_0)(11N_C - 2\,n_f)\,\log(\mu^2/\mu_0^2)/(12\pi)}\ , \tag{2.11}$$

with $N_C = 3$ the number of colours, n_f the number of flavours and $\alpha_S(\mu_0)$ taken typically at $\mu_0 = m_Z$ as reference. The evolution of Eq. (2.11) is in accordance with QCD in the Standard Model, therefore, increasing (reducing) at low (high) energies, Fig. 2.4.

Moving a step forward into the understanding and description of elementary particles and the behaviour of the interaction among them, it is crucial to confront theoretical predictions and experimental measurements. This demand is addressed through the computation of the *cross section*, a mathematical object related to all the experimental measurements in the field of high-energy physics. It is important to remark that the computation of this mathematical object is not exact for arbitrary processes, the estimation provided by Quantum Chromodynamics requires pertubative approaches, therefore, the main challenge relies on the achievable levels of precision of the cross section. In particular, the path to calculate this physical observable to a certain order implies several difficulties, mainly, those related with the knowledge of its singular structure and the strategies to deal with it.

The remainder of this chapter recalls the core ideas for the construction of the cross section[1] which support discerning whether or not the fundamental theory explains the experimental data. The process to calculate a cross section in QFT through a perturbative approach and Feynman diagrams is described. We illustrate the emergence of singularities in the context of pursuing predictions in a scalar theory. Finally, a well known physical process is presented together with the way singularities cancel out.

2.3 Scattering and decay of elementary particles

In a scattering experiment the likelihood of a particular process is given in terms of a cross section. Regarding the theoretical side, the prediction of a scattering cross section is based on the S-matrix elements which contains all the information about the evolution in time from an initial state to a final state. An important assumption to remark is that both states have to be considered to be asymptotically free.

The probability that given an initial state of n particles $|i\rangle$ with momenta $\{p_1, \ldots, p_n\}$ evolves into a final state of n' particles with momenta $\{p'_1, \ldots, p'_n\}$ is given by the square of the S-matrix element, $\langle f| S |i\rangle$. The S matrix is defined as

$$S = \mathbf{I} + i\mathcal{T}, \tag{2.12}$$

[1] The reader can find a complete development of this topic in [72, 73].

where $\mathbf{I}$ stands for a context with no interactions and $\mathcal{T}$, the transfer matrix, describes deviations from the free theory by the following term

$$\mathcal{T} = (2\pi)^4 \, \delta^4 \left(\sum_j p_j - \sum_k p'_k \right) \mathcal{M} \left(i \to f \right) \ . \tag{2.13}$$

The presence of a δ-function in Eq. (2.13) imposes an overall momentum conservation, and the amplitude $\mathcal{M}(i \to f)$ stores the probabilities of all possible paths that the interacting particles can take to go from state $|i\rangle$ to state $|f\rangle$.

From an applied point of view the processes of interest are those involving two particles in their initial state, therefore, we continue in a scenario of $2 \to n$ process. The S-matrix element of a scattering of two initial particles going to n particles is given by

$$\langle f| \, S \, |i\rangle = \mathbf{I} + \imath \, (2\pi)^4 \, \delta^4 \left(p_1 + p_2 - \sum_{i=1}^{n} p'_i \right) \frac{\mathcal{M} \ (p_1, p_2; p'_1, \ldots, p'_n)}{2(E_1 E_2)^{1/2} \prod_{i=1}^{n} (2E'_i)^{1/2}} \ , \tag{2.14}$$

where $\{p_1, p_2\}$, $\{m_1, m_2\}$ and $\{E_1, E_2\}$ are the momenta, the masses and energy components respectively of the two initial particles; $\{p'_1, \ldots, p'_n\}$ and $\{E'_1, \ldots, E'_n\}$ are the momenta and energy components respectively of the final particles.

Any differential cross section takes into consideration three components: a factor depending on the kinematic of the process, the amplitude $\mathcal{M}(i \to f)$, and the n-body Lorentz-invariant phase space written as,

$$d\Phi \left(p_1 + p_2; p'_1, \ldots, p'_n \right) = (2\pi)^4 \delta^4 \left(p_1 + p_2 - \sum_{i=1}^{n} p'_i \right) \prod_{i=1}^{n} \frac{d^3 p'_i}{(2\pi)^3 \, 2E_i} . \tag{2.15}$$

Gathering all the ingredients together, the differential cross section for a $2 \to n$ scattering process is represented by

$$d\sigma = \frac{|\mathcal{M}|^2}{4\sqrt{(p_1 \cdot p_2)^2 - m_1^2 m_2^2}} \, d\Phi \left(p_1 + p_2; p'_1, \ldots, p'_n \right) \ . \tag{2.16}$$

Another relevant quantity is the decay rate, the probability that an ini-

tial one-particle state with momentum p_1 becomes, after a time T, a final multi-particle state with momentum $\{p_i\}$. This case is not described by the S-matrix given that it is impossible for the incoming particle to be an asymptotic state at $-\infty$, instead, decay rate is calculated in perturbation theory assuming the interactions happen only over a finite time,

$$d\Gamma = \frac{|\mathcal{M}|^2}{2m_1} d\Phi\left(p_1; p_1', \ldots, p_n'\right) \ . \tag{2.17}$$

Going back to Eq. (2.16), an important difficulty in the computation is due to the fact, that, in general, a suitable methodology to obtain an explicit representation for $\mathcal{M}$ and consequently for σ remains unknown. The path taken to address this problem is to obtain an approximation of $\mathcal{M}$ by the implementation of perturbative approaches.

2.4 The cross section and decay rate within a perturbative framework

In the previous section we have introduced two essential concepts, the cross section and the decay rate, the observables that are used to confront theoretical predictions against the experimental data. The way of computing them is based on perturbative approaches, requiring the analysis of a power series expansion given a proper parameter. Concerning the Standard Model we could ask ourselves, which is this parameter? In order to properly answer this question, we will briefly review the perturbative QFT formalism.

The QFT framework is provided with a solid mathematical basis through the Lagrangian formalism, where small perturbations can generate a complicated system to solve given the complexity of the equation of motion. At classical level, the equation of motion describes the variation of the position as a function of time of the particles, whereas for a quantum interpretation it involves a probabilistic perspective. In QFT, the elementary particles are treated as excited states and the cross section is used to determine the probability to take one over all possible paths. The precision in this sense, is understood as estimating the corresponding probability with a concrete level of accuracy.

The usual techniques to extract the coefficients corresponding to a power series are either in analogy to the interaction picture of quantum mechan-

ics, or from the generalization of the path integral of quantum mechanics to QFT. Precisely, the fundamental object of study in QFT is the *generating functional* also known as correlation function, $Z[J]$, which explicitly depends on the Lagrangian density. For a scalar theory, the correlation function is written as

$$Z[J] \equiv \int \mathcal{D}\phi \exp\left[\imath \int d^4x \left[\mathcal{L} + J(x)\phi(x)\right]\right] , \tag{2.18}$$

where $J(x)\phi(x)$ is the *source term*. A way of proceeding to solve Eq. (2.18) is considering $\mathcal{L}$ in terms of a parameter in such a way that makes sense to evaluate an expansion in powers of the selected parameter. The application of this idea allows the estimation of a solution, furthermore, this is the key concept behind perturbative quantum field theories.

Gauge theories are the fundamentals for the understanding of the Standard Model. The relevance of these theories, regarding perturbative approaches, lies in the inherent determination of the couplings between all particles and their propagation. To illustrate this, lets consider the basic example of the Dirac equation describing the free propagation of fermions,

$$\mathcal{L}_D = \bar{\psi}(\imath\,\gamma^\mu\,\partial_\mu - m)\psi \ , \tag{2.19}$$

where ψ is the fermion field, m the mass and γ^μ the Dirac matrices. This Lagrangian is invariant under a global phase transformation,

$$\psi \to \exp[\imath\, q\, \theta]\psi \ , \tag{2.20}$$

with $q = e_f\, g$, where e_f is the electric charge of the fermion field and g a small parameter. However, the difficulties arise dealing with the terms involving derivatives, by trying to impose gauge invariance. In order to handle it, we must introduce a factor that compensates for the difference in phase transformations from one point to another. As a result, the local symmetry is recovered by promoting the ordinary derivative to a covariant derivative,

$$\partial_\mu \to D_\mu = \partial_\mu + \imath\, q A_\mu \ , \tag{2.21}$$

where the vector field, A_μ, transforms under the following local gauge transformation,

$$A_\mu \to A_\mu - \partial_\mu \theta(x) \, . \tag{2.22}$$

In this sense, given the covariant derivative in Eq. (2.21) and the transformation law for A_μ in Eq. (2.22), it is possible to write a gauge invariant Dirac Lagrangian as,

$$\mathcal{L}_D = \bar{\psi}(\imath\,\gamma^\mu D_\mu - m)\psi \ . \tag{2.23}$$

It is important to remark that Eq. (2.23) which allows an independent symmetry transformation at every point in spacetime is not a coincidence, but rather the fundamental principle that determines the form of the Lagrangian. This invariance is the famous and characterized as the *gauge symmetry* of QED.

In order to identify and understand the terms encoded in Eq. (2.23), we restate it in the following form,

$$\mathcal{L}_D = \bar{\psi}(\imath\gamma^\mu\partial_\mu - m)\psi - q\bar{\psi}\gamma^\mu\psi A_\mu \ . \tag{2.24}$$

The first term is precisely Eq. (2.19), the free Dirac equation interpreted as a propagating fermion field interacting with no particles; whereas the second term indicates the interaction between ψ and A_μ[1], having an interaction strength proportional to the electrical charge of the fermion.

To connect the concept of perurbative approaches to the Lagrangian of QED, there must exist a suitable parameter for the proper implementation of power series expansion. In this specific case, the suitable parameter is given by g supported by the fact that it is closely related to the fine-structure constant,

$$\alpha = \frac{g^2}{4\pi} \approx \frac{1}{137} \ , \tag{2.25}$$

therefore, it makes sense to apply the power of series either in α, or g, to calculate the probability of a process occurring *to a certain precision* (truncating the series to the associated order).

Regarding the SM there are three dimensionless couplings considered as proper parameters to perform the series expansions. These couplings, g_1,

[1]The dynamics of the A_μ field are governed by Maxwell's equations which was not introduced in the discussion, but which must be considered for a complete understanding of QED.

g_2 and g_3, are manifested in the series as powers of,

$$\alpha_i = \frac{g_i}{4\pi}\,, \qquad i = 1, 2, 3, \tag{2.26}$$

where each of them is associated to the groups $SU(3)_C$, $SU(2)_L$ and $U(1)_Y$ respectively. Based on this scheme, physically relevant quantities as the S-matrix or Green's functions are power series in the couplings, providing the understanding of the fundamental elements in nature by a perturbative approach. The coupling measures the strength of the interaction and the phenomenological relevance of the following orders of the series.

Considering a general scenario, the SM Lagrangian can be decomposed as

$$\mathcal{L} = \mathcal{L}_0 + \mathcal{L}_{\text{Int}}\ , \tag{2.27}$$

with $\mathcal{L}_0$ the free Lagrangian describing free propagation of particles and $\mathcal{L}_{\text{Int}}$ describing the interaction behaviour. The comprehension and appropriate treatment of these two contributions are essential to build the cross section, one is related to the Green's function and the other to the field's coupling.

i) The Green's function associated to $\mathcal{L}_0$, generates in the momentum space the *propagators* belonging to each kind of particle in the SM. Explicitly they are given by:

- Scalar field propagator

$$\tilde{\Delta}(p, m) = \frac{\imath}{p^2 - m^2 + \imath 0}\ . \tag{2.28}$$

- Fermion field propagator

$$\tilde{S}(p, m) = \frac{\imath(\not{p} + m)}{p^2 - m^2 + \imath 0}\ . \tag{2.29}$$

- Massless vector field propagator

$$\tilde{D}^{\mu\nu}(p) = \frac{-\imath}{p^2 + \imath 0}\left(g^{\mu\nu} - (1-\xi)\frac{p^\mu p^\nu}{p^2}\right)\ . \tag{2.30}$$

with $\not{p} \equiv \gamma^\mu p_\mu$, $g^{\mu\nu} = \text{diag}(1, -1, -1, -1)$, ξ the gauge parameter and m the mass of the propagating particles. The propagator of a massive vector field is analogous to Eq. (2.30). The relevance of these expressions is due to the similarity of their structure, where independently

of the particle involve in the process, the singularities of all of them arise through the denominator.

ii) The Lagrangian responsible for providing how the fields are coupled to each other is $\mathcal{L}_{\text{Int}}$. These terms depend on the α_i couplings and on mathematical structures depending on the symmetry groups of the model. The objects arising from $\mathcal{L}_{\text{Int}}$ are known as *vertices*.

Besides propagators and vertices, it is indispensable to incorporate an additional ingredient, the wave functions associated to the particles. In the case of fermion fields the so-called spinors, for vector fields the polarisation vectors.

Calculating matrix elements from first principles involve an implicit complexity in the process. With this in mind, Richard P. Feynman developed a very efficient pictorial method characterizing these mathematical objects, the so-called *Feynman Diagrams*. These diagrams contain all the required components to construct and calculate the cross section and decay rate of any theory.

The Feynman rules emerging from the Lagrangian in Eq. (2.23) are the following:

- Electron propagator

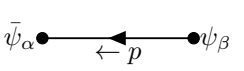

$$= \left[\frac{\imath}{\not{p} - m + \imath 0}\right]_{\alpha\beta} . \tag{2.31}$$

- Positron propagator

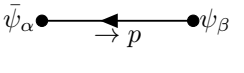

$$= \left[\frac{\imath}{-\not{p} - m + \imath 0}\right]_{\alpha\beta} . \tag{2.32}$$

- Electron-positron-photon vertex

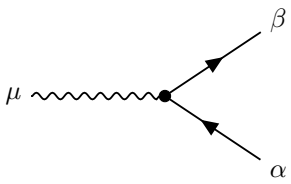

$$= \imath e(\gamma^\mu)_{\alpha\beta} . \tag{2.33}$$

α and β are spinor indices to be "attached" to the spinor solutions

from the Dirac equation[1].

The structure of vertices and propagators depend in the process of study. Putting these pieces together according to the given theory, and incorporating the coupling $\alpha \sim g^{1/2}$, the associated squared amplitude in a perturbative expansion is written as

$$|\mathcal{M}|^2 = \alpha|\mathcal{M}^{(1)}|^2 + \alpha^2|\mathcal{M}^{(2)}|^2 + \alpha^3|\mathcal{M}^{(3)}|^2 + \cdots , \tag{2.34}$$

with $\mathcal{M}^{(1)}$ denoting the leading order (LO) matrix element, $\mathcal{M}^{(2)}$ the next-to-leading order (NLO) correction and $\mathcal{M}^{(3)}$ the next-to-next-to-leading order (N^{2}LO) contribution. Each of these terms can be algorithmically constructed through the previously presented concepts, nevertheless, the difficulty arise when trying to analytically integrate Eq. (2.34). The problem in this expression is the presence of divergences which need to be characterised in order to be removed in the integration process. To have a better understanding of these difficulties, we present in the following section two illustrative examples showing that quantum corrections inevitably lead to a scenario surrounded by singularities.

2.5 Spread of infinities

QFT implies the emergence of divergences in intermediate steps of theoretical calculations. In order to clarify this fact, we present an example in the scalar theory (ϕ) with a massless particle, coupling g and the following Feynman diagrams involved,

- Scalar propagator

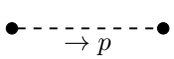

$$= \frac{\imath}{p^2 + \imath 0} . \tag{2.35}$$

- Scalar self interaction

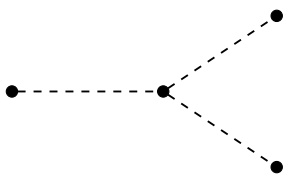

$$= \imath g . \tag{2.36}$$

[1] All the concepts related to the construction of each integrand in $|\mathcal{M}\rangle$ can be consulted in [72].

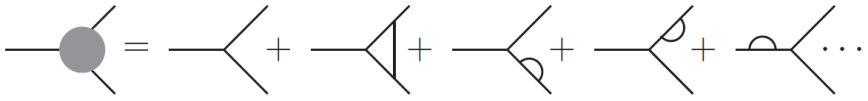

Figure 2.5: The process $\phi \to \phi\phi$ including LO and NLO contributions.

Let us assume the calculation of the process $\phi \to \phi\phi$ to NLO, whose diagrammatic representation is shown in Fig. 2.5. The first element in the series is proportional to $g \sim \alpha^{1/2}$ and the following four elements are proportional to $g^3 \sim \alpha^{3/2}$.

In order to obtain the explicit integrands involved in the computation, it is necessary to assemble the squared amplitude with a pictorial representation shown in Fig. 2.6. The integral sign inserted between the diagrams indicates that the integration has to be applied to all the possible configurations associated to a specific cut. In this sense, we can establish that the first diagram in the r.h.s. is proportional to α and the remaining four are proportional to α^2 in accordance with Eq. (2.34).

Analysing the singular behaviour associated with the contributions in Fig. 2.6 shows, that the integrand related to the first term in the r.h.s., the LO contribution is free of singularities due to the absence of propagators, therefore the integral associated to those structures can be computed without any significant problem. Concerning the rest of the terms in the r.h.s. of Fig. 2.6, the NLO contributions, they include three propagators in each term. The presence of propagators in those contributions opens the path to the singular configurations in the denominators, and the need for proper methodologies to deal with them.

All the integrals required to compute the contributions shown in Fig. 2.6 can be addressed through the customary regularization method, dimensional regularization (DREG) [74, 75]. This framework considers changing the number of space-time dimensions from 4 to $d = 4 - 2\epsilon$, allowing to exhibit the singularities as poles encoded in the limit $\epsilon \to 0$. Furthermore, the first term of the NLO contributions in Fig. 2.5 known as the triangle diagram, generates a singularity proportional to ϵ^{-2} and the rest of NLO contributions vanish when the scalar particles have no mass (massless bubble diagrams) because they are scaleless integrals.

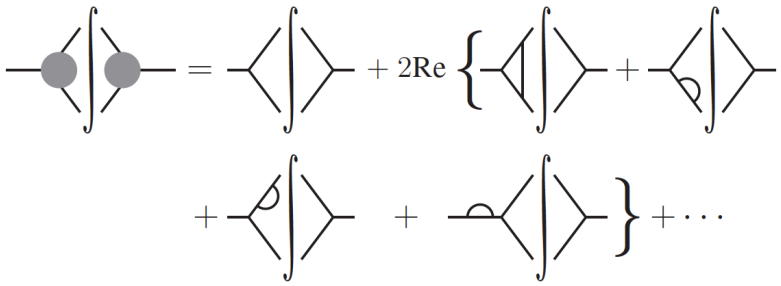

Figure 2.6: Squared amplitude for the process $\phi \to \phi\phi$ at NLO order.

It is important to remark that in order to achieve a finite cross section, these are not the only configurations needed. Additional contributions are required to cancel out the singularities arising from the triangle diagram. Concerning this specific need, the Kinoshita–Lee–Nauenberg (KLN) theorem [76, 77] assures that any quantum field theory with massless fields is free of IR singularities, disappearing after summing over virtual and degenerate initial and final states real contributions. This property is an essential concept in perturbation theory, since it allows to build infrared safe observables at any order. The pictorial representation of the contributions coming from real emissions are shown in Fig. 2.7. They are proportional to α^2, contributing to the NLO elements in terms of the series expansion.

Comparing the topological structure of virtual and real emission contributions, we observe that the first diagram in Fig. 2.7 has a similar structure compared to the triangle diagram in Fig. 2.6, allowing the feasibility of matching the associated IR singularities. Besides all the required contributions, there is a subtlety to have in mind for calculating the NLO contributions to the process. The integration domain from the real and virtual contributions do not correspond to the same kind state multiplicities. The virtual term integrates in a phase space associated to a $1 \to 2$ process, whereas the real phase space corresponds to a $1 \to 3$ process. Therefore, a general way of writing the NLO cross section is given by

$$\sigma^{(\mathrm{NLO})} = \int_{\Omega} d\sigma^{(\mathrm{V})} + \int_{\Omega+1} d\sigma^{(\mathrm{R})}, \tag{2.37}$$

implying that the real contribution considers a configuration space with one more particle than the configuration space of the virtual contribution.

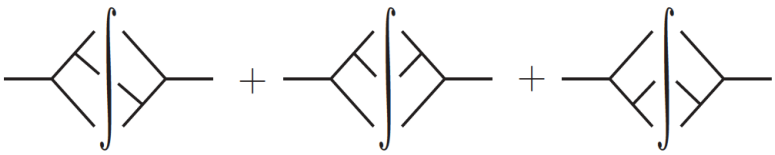

Figure 2.7: Real emission contribution to the cross section to NLO.

Let us take a step forward to the discussion of the computation of NLO corrections to the decay rate for the process $\phi(p_3) \to \phi(p_1) + \phi(p_2)$ by using DREG. Starting with the LO contribution, we have that the LO amplitude is given by

$$|\mathcal{M}^{(0)}(p_1, p_2, p_3)\rangle = \imath g \,, \tag{2.38}$$

and the corresponding LO decay rate,

$$\Gamma^{(\mathrm{LO})} = \frac{1}{2\sqrt{s_{12}}} \int d\Phi_{1\to 2} \, |\mathcal{M}^{(0)}|^2 \,, \tag{2.39}$$

where $s_{12} = (p_1 + p_2)^2 = 2p_1 \cdot p_2$. The phase space in DREG is given by

$$\int d\Phi_{1\to 2} = \frac{\Gamma(1-\epsilon)}{2(4\pi)^{3-2\epsilon}\,\Gamma(2-2\epsilon)} \left(\frac{s_{12}}{\mu^2}\right)^{-\epsilon} \,, \tag{2.40}$$

allowing to write the LO decay rate at first order in terms of ϵ,

$$\Gamma^{(\mathrm{LO})} = \frac{\alpha}{4 s_{12}} + \mathcal{O}(\epsilon) \,, \tag{2.41}$$

with $\alpha = g^2/(4\pi)$. As we observe, this expression is free of singularities. It is important to remark that at this order it is possible to address the computation in $d = 4$ space-time dimensions, nevertheless, for a higher order computation it is required to work with $d = 4 - 2\epsilon$.

Moving forward to NLO, we need to consider the virtual and real contributions. For the virtual matrix element we have,

$$|\mathcal{M}^{(1)}(p_1, p_2, p_3)\rangle = -\imath g^3 s_{12} L^{(1)}(p_1, p_2, p_3) \,. \tag{2.42}$$

The scalar three-point function at one loop

$$L^{(1)}(p_1, p_2, p_3) = -\imath \mu^{2\epsilon} \int \frac{d^d \ell}{(2\pi)^d} \prod_{i=1}^{3} G_F(q_i) \,, \tag{2.43}$$

with $G_F(q_i) = (q_i^2 + \imath 0)^{-1}$ and $q_i = \ell + \sum_{j=1}^{i} p_i$, is given by the well known result [78, 79]

$$L^{(1)}(p_1, p_2, p_3) = -c_\Gamma \frac{\mu^{2\epsilon}}{\epsilon^2} (-s_{12} - \imath 0)^{-1-\epsilon} , \tag{2.44}$$

where the usual loop volume factor is

$$c_\Gamma = \frac{\Gamma(1+\epsilon)\Gamma^2(1-\epsilon)}{(4\pi)^{2-\epsilon}\Gamma(1-2\epsilon)} . \tag{2.45}$$

The result shown in Eq. (2.44) exhibits a singularity in the limit $\epsilon \to 0$.

To compute the virtual contribution to the decay rate, we have

$$\Gamma^{(\mathrm{V})} = \frac{1}{2\sqrt{s_{12}}} \int d\Phi_{1\to 2}\, 2\,\mathrm{Re}\langle \mathcal{M}^{(0)} | \mathcal{M}^{(1)} \rangle , \tag{2.46}$$

expanded as

$$\begin{aligned} \Gamma^{(\mathrm{V})} = \; & \Gamma^{(\mathrm{LO})} \frac{\alpha}{2\pi} \left(\frac{s_{12}}{\mu^2}\right)^{-\epsilon} \left[-\frac{1}{\epsilon^2} + \frac{\gamma_E - \log(4\pi)}{\epsilon} \right. \\ & \left. - \frac{1}{12} \left(6\left(\gamma_E - \log(4\pi)\right)^2 - 7\pi^2 \right) + \mathcal{O}(\epsilon) \right] , \end{aligned} \tag{2.47}$$

where γ_E is the Euler-Mascheroni constant. We have expanded to the order $\mathcal{O}(\epsilon^0)$ to locate the poles of the decay rate's virtual component at NLO.

Regarding the real contribution, the process of interest is $\phi(p_3) \to \phi(p_1') + \phi(p_2') + \phi(p_r')$ and the associated decay rate is given by

$$\Gamma^{(\mathrm{R})} = \frac{1}{2\sqrt{s_{12}}} \int d\Phi_{1\to 3}\, 2\,\mathrm{Re}\langle \mathcal{M}_{2r}^{(0)} | \mathcal{M}_{1r}^{(0)} \rangle , \tag{2.48}$$

where

$$\mathrm{Re}\langle \mathcal{M}_{2r}^{(0)} | \mathcal{M}_{1r}^{(0)} \rangle = g^4 \frac{s_{12}}{s_{1r}' s_{2r}'} . \tag{2.49}$$

The phase space in Eq. (2.48) is

$$\int d\Phi_{1\to 3} = \frac{s_{12}}{2(4\pi)^{3-2\epsilon}\Gamma(2-2\epsilon)} \left(\frac{s_{12}}{\mu^2}\right)^{-\epsilon} (y_{12}' y_{1r}' y_{2r}')^{-\epsilon}\, dy_{1r}'\, dy_{2r}' , \tag{2.50}$$

where $y_{ij}' = s_{ij}'/s_{12}$ with $s_{ij}' = (p_i' + p_j')^2$. Inserting Eqs. (2.49) and (2.50) into Eq. (2.48) we compute and expand the real contribution in a Laurent

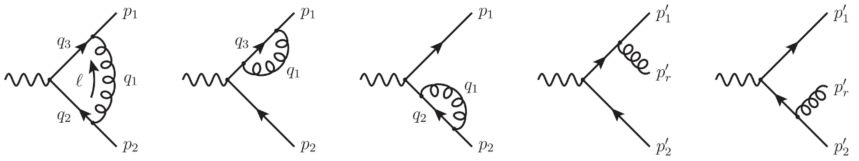

Figure 2.8: Momentum configuration and Feynman diagrams corresponding to the process $\gamma^* \to q\bar{q}(g)$.

series,

$$\Gamma^{(\mathrm{R})} = \Gamma^{(\mathrm{LO})} \frac{\alpha}{2\pi} \left(\frac{s_{12}}{\mu^2}\right)^{-\epsilon} \left[\frac{1}{\epsilon^2} - \frac{\gamma_E - \log(4\pi)}{\epsilon} + \frac{1}{12}\left(6\left(\gamma_E - \log(4\pi)\right)^2 - 7\pi^2\right) + \mathcal{O}(\epsilon)\right] . \tag{2.51}$$

The decay rate computation at NLO is completed by combining the virtual and real contributions in Eqs. (2.47) and (2.51), getting as a final result

$$\Gamma^{(\mathrm{NLO})} = \Gamma^{(\mathrm{V})} + \Gamma^{(\mathrm{R})} = +\mathcal{O}(\epsilon) . \tag{2.52}$$

It is important to remark that obtaining the corresponding NLO correction, which is zero in this case, the cancellation of singularities is required which only occurs by the exact matching among them.

The previous example is used as a reference to illustrate the way of proceeding to compute the NLO corrections for any process. The following example considers the decay rate calculation of a physical process, $\gamma^* \to q\bar{q}(g)$, to NLO in a QCD+QED scenario with massless quarks. The Feynman diagrams involved in this process are shown in Fig. 2.8.

Starting at LO we have that the squared amplitude is given by

$$|\mathcal{M}^{(0)}_{q\bar{q}}|^2 = 2\, C_A\, (e\, e_q)^2\, s_{12}\, (1-\epsilon) , \tag{2.53}$$

where C_A is the quadratic Casimir invariant of $SU(3)$ group in the adjoint representation, e denotes the electromagnetic coupling and e_q the quark electric charge. Given Eq. (2.53) and recalling Eq. (2.39), the LO decay rate is written as

$$\Gamma^{(\mathrm{LO})} = \frac{1}{2}\alpha\, e_q^2\, C_A + \mathcal{O}(\epsilon) . \tag{2.54}$$

Regarding NLO, we need to consider the virtual and real contributions [80]. The expansion of the virtual contribution is given by

$$\Gamma^{(\mathrm{V})} = \Gamma^{(\mathrm{LO})}\, c_\Gamma\, g_\mathrm{S}^2\, C_F \left(\frac{s_{12}}{\mu^2}\right)^{-\epsilon} \left[-\frac{4}{\epsilon^2} - \frac{6}{\epsilon} - 16 + 2\pi^2 + +\mathcal{O}(\epsilon)\right] , \quad (2.55)$$

with g_S the strong coupling and C_F the quadratic Casimir invariant of $SU(3)$ in the fundamental representation. In the case of the real contribution we have that

$$\Gamma^{(\mathrm{R})} = \Gamma^{(\mathrm{LO})}\, c_\Gamma\, g_\mathrm{S}^2\, C_F \left(\frac{s_{12}}{\mu^2}\right)^{-\epsilon} \left[\frac{4}{\epsilon^2} + \frac{6}{\epsilon} + 19 - 2\pi^2 + \mathcal{O}(\epsilon)\right] . \quad (2.56)$$

The virtual and real contributions in Eqs. (2.55) and (2.56) exhibit single and double poles. These singularities cancel each other out by putting them together, allowing to write the NLO decay rate as

$$\Gamma^{(\mathrm{NLO})} = \Gamma^{(\mathrm{V})} + \Gamma^{(\mathrm{R})} = 3\, C_F\, \frac{\alpha_\mathrm{S}}{4\pi}\, \Gamma^{(\mathrm{LO})} . \quad (2.57)$$

Finally, we have all the ingredients needed to present the observable corresponding to the process $\gamma^* \to q\bar{q}(g)$,

$$\Gamma = \Gamma^{(\mathrm{LO})} \left(1 + 3\, C_F\, \frac{\alpha_\mathrm{S}}{4\pi} + \mathcal{O}(\alpha_\mathrm{S}^2)\right) , \quad (2.58)$$

which is the one used for the comparison of theoretical predictions and experimental data. It is important to highlight that the result turns out to be finite just *after* integrating and combining the virtual and real contributions, i.e., at integral level. This scenario implies to integrate expressions involving singularities, demanding numerical evaluation techniques to take extreme care in the treatment of singularities to achieve a proper cancellation and therefore, a finite numerical result.

Similar to the example presented in this section, there are many other processes for which working at integral level (up to certain level of precision) is still manageable. Nevertheless, the real challenge for the theoretical community arises when it comes to achieving higher orders and increasing the number of external particles involved in a process. The complexity arising in Feynman loop integrals by pushing the precision frontier is due to the numerical instabilities emerging in thresholds configurations and singularities that cancel only after putting all the contributions together.

Currently, there is a great effort to developed new methodologies for a more efficient calculation of physical observables at higher orders. Particularly, alternative techniques to improve the numerical evaluation stability give a more suitable treatment of singularities. In this sense, in the following chapter we introduce the Loop-Tree Duality (LTD), a novel method that opens any loop diagram to a forest of connected trees whose core feature is the distinction between physical and unphysical singularities at **integrand** level.

Chapter 3

The Loop-Tree Duality evolution

In this chapter we take a brief journey through the most significant developments and applications that the Loop-Tree Duality has undergone before its most recent major achievement; its reformulation towards higher orders [6]. As a first step we review the fundamental concepts that gave rise to the original LTD representation [81]. Then, we proceed with an analysis of its distinctive features to close this chapter with some relevant applications.

3.1 Fundamental concepts

A critical challenge in perturbative Quantum Field Theory is the description of quantum fluctuations in high-energy scattering processes by the calculation of multiloop scattering amplitudes. With this very special need in the field, the year of 2008 saw the emergence of the Loop-Tree Duality [81], a novel technique that establishes a duality relation between one-loop integrals and phase-space integrals emerging from them through single cuts. The LTD framework was inspired by the Feynman Tree Theorem (FTT) [82,83] which relates perturbative scattering amplitudes and Green's functions at the loop level with analogous quantities at the tree level considering multiple cuts of the original loop Feynman diagram.

To deepen into the LTD framework, we recall some important aspects from Ref. [81], the basic concepts of the FTT at one-loop and its relation with

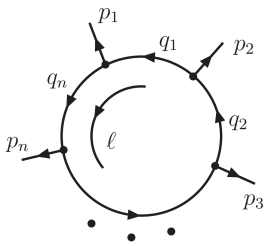

Figure 3.1: The one-loop n-point scalar integral.

the LTD. Without loss of generality, the generic one-loop scalar integral depicted in Fig. 3.1 was studied considering an arbitrary number of external particles (or n internal lines)

$$L^{(1)}(p_1,\ldots,p_n) = \int_\ell \prod_{i=1}^{n} G_F(q_i) \ . \tag{3.1}$$

The integration measure in dimensional regularization [74, 75] reads

$$\int_\ell = -\imath\mu^{4-d} \int \frac{d^d\ell}{(2\pi)^d}, \tag{3.2}$$

with d the number of space-time dimensions and μ an arbitrary energy scale. The momenta of the external particles are denoted by p_i, $i \in \{1,\ldots,n\}$ and $k_i = p_1 + \cdots + p_i$ with $k_n = 0$ due to momentum conservation. The momenta q_i of each Feynman propagator $G_F(q_i)$ are a linear combination of the loop and external momenta, $q_i = \ell + k_i$. The standard definition of a Feynman propagator is given by

$$G_F(q_i) = \frac{1}{q_i^2 - m_i^2 + \imath 0} \ , \tag{3.3}$$

with m_i its mass and $\imath 0$ the usual Feynman's infinitesimal imaginary prescription. Additionally, an alternative and convenient way of writing Eq. (3.3) is in such a way that the location of the poles are shown explicitly,

$$G_F(q_i) = \frac{1}{\left(q_{i,0} - q_{i,0}^{(+)}\right)\left(q_{i,0} + q_{i,0}^{(+)}\right)} \ , \tag{3.4}$$

written in terms of $q_{i,0}$ and $\mathbf{q}_i$, the time and spatial components of the momentum q_i, respectively, and

$$q_{i,0}^{(+)} = \sqrt{\mathbf{q}_i^2 + m_i^2 - \imath 0} \; . \tag{3.5}$$

We recall the concepts of advanced propagators and advanced one-loop integrals. The advanced propagator is defined as

$$G_A(q_i) = \frac{1}{q_i^2 - m_i^2 - \imath 0 \, q_{i,0}} \; , \tag{3.6}$$

and differs from the Feynman propagator in the position of the poles in the complex plane of the variable $q_{i,0}$ as shown in Fig. 3.2. The poles of the advanced propagator are slightly displaced above the real axis independently of the sign of the energy; in the Feynman propagator the pole with positive (negative) energy is slightly displaced below (above) the real axis. The advanced one-loop integral is obtained by replacing the Feynman propagators in Eq. (3.1) by advanced propagators,

$$L_A^{(1)}(p_1, \ldots, p_n) = \int_\ell \prod_{i=1}^{n} G_A(q_i) \; . \tag{3.7}$$

The evaluation of the advanced one-loop integral is given by

$$\begin{aligned} L_A^{(1)}(p_1, \ldots, p_n) &= \int_{\boldsymbol{\ell}} \int_{C_L} \prod_{i=1}^{n} G_A(q_i) \\ &= \int_{\boldsymbol{\ell}} \sum_i \mathrm{Res} \left(\prod_{i=1}^{n} G_A(q_i), \mathrm{Im}(\eta \cdot q_i) < 0 \right) , \end{aligned} \tag{3.8}$$

where the future-like vector is taken as $\eta^\mu = (1, \mathbf{0})$, equivalent to integrating out the loop energy component ℓ_0 along a suitable integration path C_L closed in the lower half-plane of the complex variable ℓ_0, with $\mathrm{Im}(\eta \cdot q_i) < 0$. In Fig. 3.3, a pictorial representation of the singularities of the advanced integrand in the ℓ_0 complex plane is shown; the singularities are the poles located in the upper half-plane. The integral along C_L is equal to the sum of the residues evaluated at the poles in the lower half-plane, therefore we have,

$$L_A^{(1)}(p_1, \ldots, p_n) = 0 \; . \tag{3.9}$$

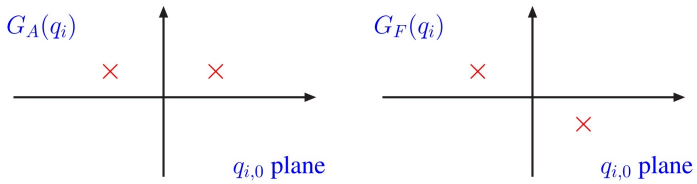

Figure 3.2: Location of the poles of the advanced and Feynman propagators, $G_A(q_i)$ and $G_F(q_i)$, in the complex plane of the variable $q_{i,0}$.

On the other hand, the relation between the advanced and Feynman propagators given by

$$G_A(q_i) = G_F(q_i) + \tilde{\delta}(q_i)\,, \tag{3.10}$$

with $\tilde{\delta}(q_i) = 2\pi\ \imath\ \theta(q_{i,0})\ \delta(q_i^2 - m_i^2)$, is used to establish the relation between the advanced one-loop integral and the original one-loop integral. The Eq. (3.10) is substituted into the r.h.s. of Eq. (3.7) and one obtains the following expression,

$$\begin{aligned} & L_A^{(1)}(p_1,\ldots,p_n) \\ &= \int_\ell \prod_{i=1}^{n} (G_F(q_i) + \tilde{\delta}(q_i)) \\ &= L^{(1)}(p_1,\ldots,p_n) + L^{(1)}_{1-cut}(p_1,\ldots,p_n) + \cdots + L^{(1)}_{n-cut}(p_1,\ldots,p_n)\,, \end{aligned} \tag{3.11}$$

where the m-cut terms, $L_{(m-cut)}$ $(m \leq n)$, are the contributions with precisely m delta functions.

The FTT arises by combining the results of Eq. (3.9) and Eq. (3.11), relating the one-loop integral to the multiple-cut integrals $L^{(1)}_{m-cut}$ as follows,

$$L^{(1)} = -\left(L^{(1)}_{1-cut} + L^{(1)}_{2-cut} + \cdots + L^{(1)}_{n-cut}\right)\,. \tag{3.12}$$

Each delta function in $L^{(1)}_{m-cut}$ replaces the corresponding Feynman propagator in $L^{(1)}$ by cutting the internal line with momentum q_i, i.e., to set the respective particle on shell. Each m-particle cut decomposes the one-loop diagram into m disjoint tree diagrams. In this sense, FTT allows us to calculate loop diagrams from tree-level diagrams.

The extension of the FTT from the one-loop integrals to one-loop scattering amplitudes in perturbative quantum field theories is straightforward,

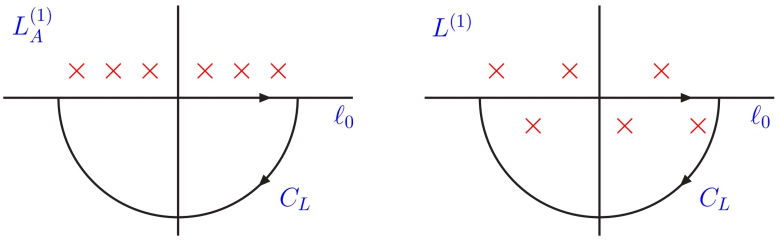

Figure 3.3: Location of the poles and integration contour C_L in the complex ℓ_0-plane for the advanced (left) and Feynman (right) one-loop scattering amplitudes, $L_A^{(1)}$ and $L^{(1)}$.

as long as, the corresponding field theory is unitary and local. The generalization of Eq. (3.12) to any scattering amplitude is given by [82, 83]

$$\mathcal{A}^{(1)} = -\left(\mathcal{A}^{(1)}_{1-cut} + \mathcal{A}^{(1)}_{2-cut} + \cdots + \mathcal{A}^{(1)}_{n-cut}\right) , \tag{3.13}$$

where $\mathcal{A}^{(1)}_{m-cut}$ is obtained in the same way as $L^{(1)}_{m-cut}$, starting from the original scattering amplitude $\mathcal{A}^{(1)}$ and considering all possibel replacements of m Feynman propagators, $G_F(q_i)$, of its loop internal lines with the $\tilde{\delta}(q_i)$.

The similarity of the LTD with the FTT is quite close, nevertheless, there is a crucial difference. The FTT starts from the advanced loop integral $L_A^{(1)}$ whereas in the LTD the residue theorem is directly applied to the computation of the loop integral $L^{(1)}$,

$$\begin{aligned} L^{(1)}(p_1,\ldots,p_n) &= \int_{\boldsymbol{\ell}} \int_{C_L} \prod_{i=1}^{n} G_F(q_i) \\ &= -2\pi\imath \int_{\boldsymbol{\ell}} \sum \text{Res}\left(\prod_{i=1}^{n} G_F(q_i), \text{Im}(\eta\cdot q_i) < 0\right) . \end{aligned} \tag{3.14}$$

In contrast to the advanced propagator each Feynman propagator has single poles in the upper and lower half-planes of the complex variable ℓ_0 (see Fig. 3.3 right). Therefore, the poles located in the lower half-plane contribute to the computation of $L^{(1)}$. The sum over the residues in Eq. (3.14) has contributions from n terms, the residues associated to the poles with negative imaginary part of each propagator $G_F(q_i)$.

The residue at the i-th pole is given by

$$\begin{aligned}\mathrm{Res}_{\{i-\text{th pole}\}}\left[\prod_{j=1}^{n} G_F(q_j)\right] \\ = \left[\mathrm{Res}_{\{i-\text{th pole}\}} G_F(q_i)\right]\left[\prod_{\substack{j=1\\ j\neq i}}^{n} G_F(q_j)\right]_{\{i-\text{th pole}\}}\end{aligned}, \quad (3.15)$$

due to the fact that the propagators $G_F(q_j)$, with $j \neq i$, are not singular at the value of the pole of $G_F(q_i)$. The evaluation of the residue of $G_F(q_i)$ gives

$$\begin{aligned}\left[\mathrm{Res}_{\{i-\text{th pole}\}} G_F(q_i)\right] &= \left[\mathrm{Res}_{\{i-\text{th pole}\}} \frac{1}{q_i^2 - m_i^2 + \imath 0}\right] \\ &= \int_{\ell_0} \theta(q_{i,0})\, \delta(q_i^2 - m_i^2)\ . \end{aligned} \quad (3.16)$$

It shows that taking the residues of the Feynman propagator of the internal line with momentum q_i, corresponds to cut that line by including the associated on-shell propagator, $\delta(q_i^2)$, with a positive-energy mode selection, $\theta(q_{i,0})$. Substituting Eq. (3.16) into Eq. (3.14) provides a representation of the one-loop integral as a linear combination of n single-cut phase-space integrals. The calculation of the second term in the r.h.s of Eq. (3.15) leads to

$$\left[\prod_{j\neq i} G(q_j)\right]_{\{i-\text{th pole}\}} = \prod_{j\neq i} \frac{1}{q_j^2 - m_j^2 - \imath 0\ \eta(q_j - q_i)}\ , \quad (3.17)$$

where the dual propagator is defined as

$$G_D(q_i; q_j) = \frac{1}{q_j^2 - m_j^2 - \imath 0\ \eta k_{ji}} \quad \text{with} \quad k_{ji} = q_j - q_i\ . \quad (3.18)$$

It is important to realize that the calculation of the residue at the pole of the internal line with momentum q_i changes the propagators of the other lines in the loop integral. The singularity of the uncut Feynman propagators in Eq. (3.17), $G_F(q_j) = (q_j^2 - m_j^2 + \imath 0)^{-1}$, is regularized by a modification of the customary Feynman $\imath 0$ prescription, named *dual prescription*. The dual prescription arises from the fact that the original Feynman propagator,

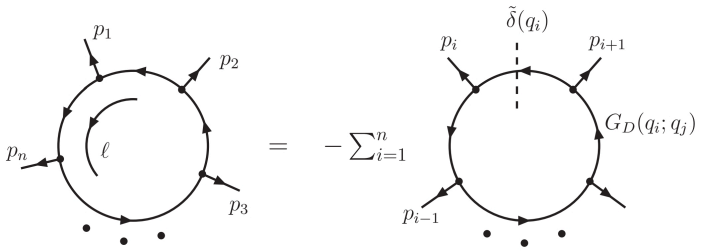

Figure 3.4: One-loop scalar integral with n external legs and its dual opening representation. The dashed line represents the on-shell cut over the i propagator.

$G_F(q_j)$, is evaluated at the complex value of the loop momentum ℓ which is determined by the location of the pole at $q_i^2 - m_i^2 + \imath 0 = 0$. The appearance of the vector η_μ is an implication of the residue theorem evaluation; the η_μ dependence of the $\imath 0$ prescription is because the residues at each of the poles are not Lorentz-invariant quantities. The Lorentz-invariance of the loop integral is restored after summing over all the residues. Furthermore, the momentum difference ηk_{ji} is independent of the integration momentum ℓ, and depends exclusively on the momenta of the external legs.

The duality relation between one-loop integrals and phase-space integrals is obtained by combining Eqs. (3.15) and (3.17),

$$L^{(1)}(p_1,\ldots,p_n) = -\int_\ell \sum_{i=1}^{n} \tilde{\delta}(q_i) \prod_{\substack{j=1 \\ j\neq i}}^{n} G_D(q_i;q_j)\,. \tag{3.19}$$

Contrary to the FTT, the LTD representation only contains single-cut integrals. The absence of multiple cuts is due to the modification of the customary $\imath 0$ prescription of the uncut Feynman propagators by the dual prescription $-\imath 0\ \eta k_{ji}$. The demonstration of Eq. (3.19) and all the details related to this study are presented in Ref. [81].

To extend the Loop-Tree Duality theorem at one-loop to higher-orders [84], it is important to realize the need to deal with several integration loop momenta. In order to set the scenario in a more manageable way, the concept of sets of internal momenta depending on the same integration loop momenta is introduced, which simplifies working with an arbitrary number of propagators. The Feynman, advanced and dual propagators of a set of

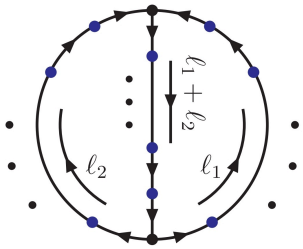

Figure 3.5: Two-loop Feynman diagram with n external legs, which are represented by the dots.

internal momenta, k, are defined as

$$G_{F(A)}(k) = \prod_{i\in k} G_{F(A)}(q_i), \qquad G_D(k) = \sum_{i\in k} \tilde{\delta}(q_i) \prod_{\substack{j\in k \\ j\neq i}} G_D(q_i;q_j). \quad (3.20)$$

For the one-loop case, the set k is given by all the internal momenta of the diagram, $k = \{1, 2, \ldots, n\}$, which depend on the single loop momentum ℓ. If the set k consists only of one propagator ($k = \{i\}$), then the dual propagator is given by $G_D(k) = \tilde{\delta}(q_i)$ with $\tilde{\delta}(q_i) = 2\pi\,\imath\,\theta(q_{i,0})\,\delta(q_i^2 - m_i^2)$. In general, the set k can depend on any linear combination of loop momenta, and several loop lines k are required to label all the internal momenta of an arbitrary multiloop diagram. We also introduce a shorthand notation to denote a set of dual propagators with inverted momentum flow

$$G_D\left(\overline{k}\right) = \sum_{i\in k} \tilde{\delta}\left(-q_i\right) \prod_{\substack{j\in k \\ j\neq i}} G_D\left(-q_i;-q_j\right). \quad (3.21)$$

This is equivalent to select the on-shell modes with negative energy of the corresponding propagators. Particularly for Feynman propagators, it follows that $G_F(\overline{k}) = G_F(k)$ because they encode both energy modes.

In order to enable a straightforward derivation of the duality theorem of a set of internal momenta at one-loop, it is crucial to take into account the connection among the advanced, Feynman and dual propagators. Analogous to Eq. (3.10), the relation among these propagators for any set of internal momenta k is given by

$$G_A(k) = G_F(k) + G_D(k). \quad (3.22)$$

Bringing together the results from Eq. (3.9) and Eq. (3.22) it follows that

$$0 = \int_{\ell_1} G_A(1) = \int_{\ell_1} \left[G_F(1) + G_D(1) \right] , \tag{3.23}$$

where the set 1 labels all the internal momenta depending on ℓ_1. The first term in the r.h.s is the original one-loop integral; therefore,

$$L^{(1)}(1) = -\int_{\ell_1} G_D(1) \tag{3.24}$$

gives the duality relation between one-loop integrals and single-cut phase-space integrals. The scenario of working with sets of internal momenta considers the possibility to attach an arbitrary number of external legs. A change in the notation of a generic loop scalar integral is given in the argument. Now we write the labels of the sets of momenta involved instead of the external particles momenta.

Going to the next step in complexity, it is essential to consider a scenario depending on the union of sets. To obtain the dual opening of two-loop integrals considering sets of loop momenta, two ingredients are required:

- The generalization of Eq. (3.24) to a multiloop diagram,

$$\int_{\ell_i} G_F(1 \cup 2 \cup \ldots \cup n) = -\int_{\ell_i} G_D(1 \cup 2 \cup \ldots \cup n) , \tag{3.25}$$

  where the sets from 1 to n depend on the same integration momentum ℓ_i.

- The dual propagator of the union of any two sets written in terms of propagators of a single set,

$$G_D(i \cup j) = G_D(i)\; G_D(j) + G_D(i)\; G_F(j) + G_F(i)\; G_D(j) . \tag{3.26}$$

Explicitly, the extension of LTD to two loops [84] regards the diagram shown in Fig. 3.5 with three sets of internal momenta and P external particles,

$$L^{(2)}(1,2,3) = \int_{\ell_1,\ell_2} \mathcal{N}(\ell_1,\ell_2)\, G_F(1 \cup 2 \cup 3) . \tag{3.27}$$

We do consider a nonscalar integral with a numerator $\mathcal{N}(\ell_1,\ell_2)$. The three sets of internal momenta: 1, 2 and 3, depend on ℓ_1, ℓ_2 and $\ell_1 + \ell_2$ re-

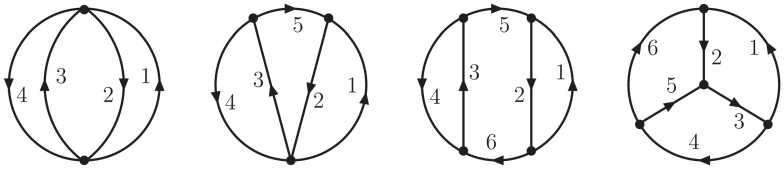

Figure 3.6: Selected three-loop scalar integrals. Each internal line set can consider an arbitrary number of external particles.

spectively. The strategy used was based on the iterative application of Eqs. (3.23), (3.25) and (3.26) which led to the following expression,

$$L^{(2)}(1,2,3) = \int_{\ell_1,\ell_2} \mathcal{N}(\ell_1,\ell_2) \otimes [-G_D(1)\; G_F(2)\; G_D(3) + G_D(1)\; G_D(2\cup 3) + G_D(3)\; G_D(\overline{1}\cup 2)] \;, \quad (3.28)$$

where all the terms in the integrand contain exactly two dual functions, i.e., this representation is written in terms of double-cut integrals only. The convolution symbol $\otimes$ is used to indicate that the on-shell conditions of each term of the integrand operate on the numerator. The integrand is reinterpreted as a sum over tree-level diagrams integrated over a two-body phase-space. However, the integrand in Eq. (3.28) contains several dual functions of two different loop lines, and hence the dual prescription might still depend on the integration momenta and in some cases may change sign within the integration volume, therefore moving up or down the position of the poles in the complex plane.

To avoid the dependence of the dual prescription on the integration momenta, the relation of the dual propagator of the union of two sets given in Eq. (3.26) was used, allowing to rewrite Eq. (3.28) as follows

$$L^{(2)}(1,2,3) = \int_{\ell_1,\ell_2} \mathcal{N}(\ell_1,\ell_2) \otimes [G_D(1)\; G_D(2)\; G_F(3) + G_D(\overline{1})\; G_F(2)\; G_D(3) + G^*(1)\; G_D(2)\; G_D(3)] \;, \quad (3.29)$$

with $G^*(k) \equiv G_F(k) + G_D(k) + G_D(\overline{k})$. In this case the integrand contains dual functions of only one set, and hence the "dual" prescription depends exclusively on external momenta. Nevertheless, the third term in the r.h.s includes also triple cuts due to the contributions with three dual propagators. The triple cuts are such that there is no more than one cut per loop

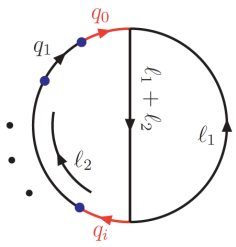

Figure 3.7: Two-loop with a one-loop self-energy insertion. The propagators q_0 and q_i have the same momentum which generates poles of second order.

line, therefore they split the two-loop diagram into two disconnected tree-level diagrams.

From the results obtained at two-loop level we must be aware that we are facing a scenario with either, a dual representation expressed in terms of double cuts but possible dual prescription depending on the integration momenta; or a scenario where the dual prescription depends exclusively on the external momenta but considers triple cuts. In addition to the two-loop case, in Ref. [84] the three-loop level was also explored and analized through the selected topologies depicted in Fig. 3.6. The procedure for developing the dual opening at this level follows the same idea used in the two-loop case, i.e. the iterative application of Eq. (3.23). Related to any multiloop topology, the corresponding dual expression can be expressed in different ways relying on the loop order of applying the duality theorem.

It is important to emphasise that the dual representation obtained at two and three loops is valid as far as only single poles are present when the Cauchy residue theorem is applied. At one-loop, the presence of multiple poles can be avoided by a convenient choice of the gauge or of the dual vector [81]. Regarding two loops or higher orders, self-energy insertions may be considered and, as a consequence, higher order poles might appear. Extending the duality theorem beyond diagrams with single poles requires to evaluate the contribution of the higher order poles which depends on the topology configuration, the nature of the internal propagators and the interaction vertices. The study of higher order poles has been addressed in Ref. [85], working explicitly with two- and three-loop integrals with multiple identical propagators.

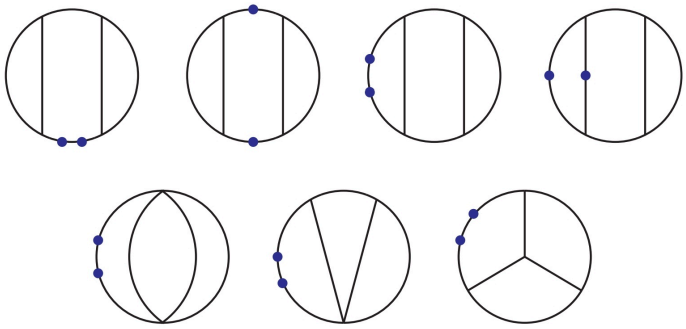

Figure 3.8: Three-loop diagrams with double and triple propagators. The dots indicate external particles.

The first case of higher order poles arises at the two-loop level, with the sole double pole generic graph shown in Fig. 3.7. The procedure followed similar steps as the one-loop case, cutting every propagator line once, including the double propagator, and transforming the rest of the propagators to dual propagators. For the case of triple and higher poles, the calculation of the residue introduces contributions with powers of dual propagators. The tactic followed to deal with higher-order pole integrals was reducing them to single pole integrals by the application of Integration-By-Parts identities [86, 87], allowing the use of the LTD theorem in its original form for single pole propagators. This procedure was explicitly applied in Ref. [85] to the two-loop scalar integral with n external legs and a double propagator, and to the three-loop diagrams with double and triple identical propagators shown in Fig. 3.8.

3.2 Singular behaviour in the loop momentum space

The detailed study of the singular structure of loop integrals and scattering amplitudes through the LTD framework has been addressed in Refs. [7, 88]. The analysis is performed in the loop momentum space relying on the possibility of establishing a physical interpretation of the loop singularities [89] and the feasibility to relate virtual and real-emission contributions.

The main goal in Ref. [88] was to accomplish an appropriate partial cancellation of singularities at loop-integrand level among dual contributions

interpreted in terms of causality. Another relevant contribution was reported in Ref. [7], it included an analysis at two loops and the study of anomalous thresholds. In both analysis, the development was addressed through the study of the propagator properties which are directly related with the emergence of singularities in any loop integral or scattering amplitude. We will review the most important concepts and results from these two studies.

The two on-shell modes of an arbitrary Feynman propagator written as in Eq. (3.3) can be graphically represented by an hyperboloid in the loop momentum space, where the minimal distance between the hyperboloid and its origin is determined by the internal mass. These are the surfaces where the loop integrand in the Feynman representation becomes singular. This singular structure can be illustrated through a kinematical scenario considering three propagators where two momenta, q_1 and q_2, are separated by a time-like distance, $(q_2 - q_1)^2 > 0$, and a third momentum, q_3, is space-like separated with respect to the other two, $(q_3 - q_1)^2 < 0$ and $(q_3 - q_2)^2 < 0$. The on-shell hyperboloids of the three propagators are depicted in Fig. 3.9 (left for massive propagators and right for massless propagators, also called light-cones). Solid lines represent the forward on-shell hyperboloids ($q_{i,0} > 0$) and dashed lines the backward on-shell hyperboloids ($q_{i,0} < 0$). With $q_i = \ell + k_i$, the origin of the hyperboloids is located at $-k_i$.

The advantage of the LTD representation is that the loop integrand becomes singular only at the intersection of two or more on-shell hyperboloids, where two or more Feynman propagators become simultaneously singular, because the integration domain is restricted to the forward on-shell hyperboloids through Cauchy's residue selection. In most cases, these singularities arising due to normal or anomalous thresholds of intermediate states [90, 91], are integrable. Nevertheless, if two massless propagators are separated by a light-like distance then the respective light-cones overlap as shown in Fig. 3.9 (right), leading to non-integrable collinear singularities. Additionaly, soft singularities can be also generated by massless propagators.

Regarding dual propagators, is important to highlight that they can be

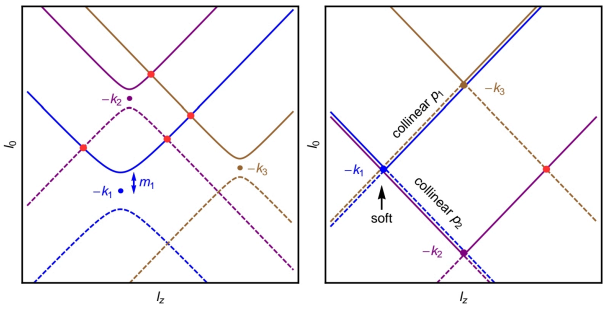

Figure 3.9: On-shell hyperboloids in the (ℓ_0, ℓ_z) space for three arbitrary massive propagators (left). On-shell hyperboloids degenerate to light-cones for massless propagators generating infrared singularities (right).

written also as

$$\tilde{\delta}(q_i)\; G_D(q_i;q_j) = \imath\; 2\pi \frac{\delta\left(q_{i,0} - q_{i,0}^{(+)}\right)}{2q_{i,0}^{(+)}} \frac{1}{\left(q_{i,0}^{(+)} + k_{ji,0}\right)^2 - \left(q_{j,0}^{(+)}\right)^2}\,, \quad (3.30)$$

where $q_{i,0}^{(+)}$ is the on-shell loop energy measured along the on-shell hyperboloid with origin at $-k_i$. Also, it is important to have in mind that integrating along the forward on-shell hyperboloids of two propagators separated by a space-like distance hits the singularity twice with opposite sign because propagators are positive inside the on-shell hyperboloids and negative outside. To continue the analysis of the singular behavior of one-loop amplitudes, the following integrand function was considered

$$S_{ij}^{(1)} = (2\pi\imath)^{-1} G_D(q_i;q_j)\tilde{\delta}(q_i) + (i \leftrightarrow j), \quad (3.31)$$

representing the sum of two single-cut dual contributions. The set of conditions encoding the singularities in Eq. (3.31) is given by,

$$\lambda_{ij}^{\pm\pm} = \pm q_{i,0}^{(+)} \pm q_{j,0}^{(+)} + k_{ji,0} \to 0\;. \quad (3.32)$$

Indeed, there are only two independent limits that establish the location of singularities in the loop momentum space: $\lambda_{ij}^{++} \to 0$ and $\lambda_{ij}^{+-} \to 0$.

The condition $\lambda_{ij}^{++} \to 0$ is satisfied at the intersection of a forward on-shell hyperboloid (positive energy mode) with a backward on-shell hyperboloid

(negative energy mode); the solution of Eq. (3.31) under this limit requires

$$k_{ji}^2 - (m_j + m_i)^2 \geq 0 \quad \text{and} \quad k_{ji,0} < 0 \; . \tag{3.33}$$

This is interpreted in this way: the q_j propagator must be in the future of the q_i propagator with both propagators causally connected ($\lambda_{ij}^{--} \to 0$ and $k_{ji,0} > 0$ represents the complementary solution). The limit $\lambda_{ij}^{++} \to 0$ represents the usual unitarity threshold due to the fact that it involves one backward and one forward on-shell hyperboloid, this scenario is equivalent to two physical particles propagating in the same direction in time. For massless propagators and light-like separation ($k_{ji}^2 = 0$), the singular surface becomes a collinear singularity along a finite region, with the on-shell energy bounded by the energy of external momenta, $q_{r,0}^{(+)} \leq |k_{ji,0}|$ with $r \in \{i, j\}$.

The other potential singularities occur for $\lambda_{ij}^{+-} \to 0$ with

$$k_{ji}^2 - (m_j - m_i)^2 \leq 0 \; , \tag{3.34}$$

which generates unphysical thresholds in each of the dual components, nevertheless, the sum over the two single-cut dual contributions is not singular. The cancellation of these integrand singularities is fully local due to the change of sign in the dual prescription. This scenario corresponds to the on-shell emission and on-shell reabsorption of one virtual particle. Explicitly in the space-like configuration ($k_{ji}^2 < 0$), unphysical thresholds take place in the intersection of the two forward on-shell hyperboloids and in the intersection of the two backward on-shell hyperboloids. On the other hand, for the time-like case, $0 \leq k_{ji}^2 \leq (m_i - m_j)^2$, unphysical thresholds appear only in the intersection of either the forward or the backward on-shell hyperboloids.

Moving on the discussion to anomalous thresholds [7], let us consider internal propagators with real masses: anomalous thresholds at one loop arise when more than two of them go on shell simultaneously. In particular, for three propagators, it is convenient to analize the following integrand function

$$S_{ijk}^{(1)} = (2\pi\imath)^{-1} G_D(q_i, q_k) G_D(q_i, q_j) \tilde{\delta}(q_i) + \text{perm.} \; . \tag{3.35}$$

The physical singularities from Eq. (3.35) arise with the intersection of one backward with two forward on-shell hyperboloids, or two forward with one

backward. The unphysical singularities generated by the intersection of three forward on-shell hyperboloids cancel locally among the dual contributions. As it was mentioned before, the local cancellation is due to the momentum dependent $\imath 0$ dual prescription; the remaining singularities are described by causal $+\imath 0$ contributions. Finally, anomalous thresholds generated in the intersection of one backward with two forward on-shell hyperboloids,

$$\lambda_{ik}^{++} \text{ and } \lambda_{jk}^{++} \to 0 \quad \text{with} \quad \lambda_{ij}^{+-} = \lambda_{ik}^{++} - \lambda_{jk}^{++}\,, \tag{3.36}$$

also cancel at $\lambda_{ij}^{+-} \to 0$. This configuration also describes a soft singularity in the limiting case of a massless parton, $q_{i,0}^{(+)} \to 0$.

For the two-loop case, the singularities appearing from two or more propagators of the same subset behave according to the one-loop study. The exclusive two-loop IR and threshold singularities arise when the propagator that eventually goes on shell and the other two on-shell propagators belong to a different subset each. In this context, the contributions defined by all possible permutations have to be considered. Based on the dual representation in Eq.(3.28), the analysis is done through the following integrand function

$$\begin{aligned} S_{ijk}^{(2)} = (2\pi\imath)^2 \Big[& G_D(q_i;q_k)\tilde{\delta}(q_j)\tilde{\delta}(q_j) + G_D(-q_j;q_k)\tilde{\delta}(-q_j)\tilde{\delta}(q_k) \\ & + \left[G_D(q_k;q_j) + G_D(q_i;-q_j) - G_F(q_j)\right]\tilde{\delta}(q_i)\tilde{\delta}(q_k)\Big]\,, \end{aligned} \tag{3.37}$$

with $i \in 1$, $j \in 2$ and $k \in 3$. The set of conditions to determine the location of the singularities in $S_{ijk}^{(2)}$ is given by

$$\lambda_{ijk}^{\pm\pm\pm} = \pm q_{i,0}^{(+)} \pm q_{j,0}^{(+)} \pm q_{k,0}^{(+)} + k_{k(ij),0} \to 0, \tag{3.38}$$

where $k_{k(ij)} = q_k - q_i - q_j$ only depends on external momenta given a convenient choice of momentum flows.

The unitarity threshold appears in the limit $\lambda_{ijk}^{+++} \to 0$ through the intersection of the backward on-shell hyperboloid of q_k with the forward on-shell hyperboloids of q_i and q_j, the three internal physical momenta flowing in the same direction in time. For massless partons and light-like separation, $k_{k(ij)}^2 = 0$, this configuration generates a triple collinear singularity [92]. For the solution with $k_{k(ij)} > 0$, it generates IR or thresholds singularities in the limit $\lambda_{ijk}^{---} \to 0$. It is important to mention that, for both

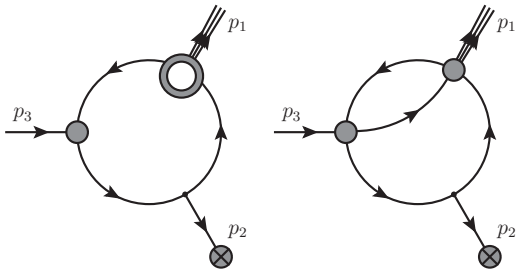

Figure 3.10: Representation of two-loop Feynman diagrams with anomalous thresholds. The momentum p_2 is space-like, $p_2^2 < 0$.

cases, the on-shell energies are limited by the energy of the external partons, $q_{r,0}^{(+)} \leq |k_{k(ij),0}|$ with $r \in \{i, j, k\}$. Other potential singularities emerge at $\lambda_{ijk}^{++-} \to 0$ and $\lambda_{ijk}^{+--} \to 0$; nevertheless, they cancel locally in the sum of all the dual components of $S_{ijk}^{(2)}$. This behaviour is feasible given that the following conditions are fulfilled in each of the cases,

$$\begin{aligned} \lambda_{ijk}^{++-} = 0, \qquad &\to \qquad q_{k,0}^{(+)} - k_{k,(ij),0} > 0\,, \\ \lambda_{ijk}^{+--} = 0, \qquad &\to \qquad q_{i,0}^{(+)} + k_{k,(ij),0} > 0\,, \end{aligned} \tag{3.39}$$

allowing that all the contributions match each other's $\imath 0$ prescription on the singularity.

Regarding anomalous thresholds, we considered configurations that involve more on-shell propagators than those appearing in the unitarity cuts. This scenario, with the propagators involved belonging to the same subset, can be distinguished from the two-loop case where it is necessary to consider propagators going simultaneously on shell from the three different sets. In Fig. 3.10, two configurations generating anomalous thresholds with the participation of the two propagators adjacent to the space-like momentum p_2 are shown. In the specific case of the right diagram, the anomalous threshold appears when four propagators become singular, two of them are dual cuts and two additional internal momenta become on shell due to kinematics ($\lambda_{i_1jk}^{+++}, \lambda_{i_2jk}^{+++} \to 0$).

3.3 Application to physical processes

The detailed study of the singular structure in the loop momentum space, through the LTD approach, opened a potential path to understand the cancellation of infrared singularities and the possibility that virtual and real radiative quantum fluctuations could be brought under a common integral, treating them simultaneously [80, 93–97].

A new approach based on the LTD framework, particularly based on the ideas exposed in Ref. [88], was used to combine virtual and real contributions in Ref. [93]. The procedure was first implemented through a scalar three-point function (internal massless particles) as a proof of concept. The divergent structure was reanalysed and its IR behaviour was isolated to a compact region of the loop three-momentum. The sum over degenerate IR states was accomplished at integrand level by a suitable mapping of three-momenta between the real radiation and the virtual kinematics. Outside this region (at large loop three-momentum), virtual corrections required only the subtraction of UV divergences at integrand level to make them finite.

This approach represented a promising alternative in perturbative calculations given that virtual and real contributions act directly as the IR subtraction counter-term of each other, allowing the possibility of carrying out purely four-dimensional implementations free of soft and final-state collinear singularities.

In order to assess the practicality of the method, it was essential to evaluate the numerical feasibility of calculating processes with many external legs through LTD. The first numerical implementation of the LTD method was presented in Refs. [94, 95], explicitly applied to scalar and tensor integrals with up to ten external legs. The analyses of the singular behaviour of the loop integrand found two types of singularities: ellipsoid singularities which required the application of contour deformation, and hyperboloid singularities that arise pairwise and cancel among dual contributions. The contour deformation proposed, effectively dealt with the ellipsoid singularities, the results were in a very good agreement with the reference values produced by LoopTools [98] and SecDec [99]. The developed code stands out, in cases that involve many external legs, a modest increase in running times in comparison to cases with fewer legs. From this study, there was optimism

that the implementation of the LTD method would represent a competitive alternative for computing multi-scale, multi-leg scalar and tensor one-loop integrals.

Following the effort to compute higher-order corrections to physical observables, a novel method based in the LTD framework was proposed: the so-called Four Dimensional Unsubtraction (FDU) [80, 96]. This methodology establishes a procedure to compute cross sections directly in four space-time dimensions following the ideas and results presented in Ref. [93]. FDU takes advantage of LTD features where the singular structure of the dual contributions closely resembles real-emission amplitudes, allowing to define suitable momentum mappings to perform a real-virtual combination at integrand level. The combination of dual and real contributions leads to a fully local cancellation of singularities making the introduction of IR counterterms unnecessary.

Regarding the cancellation of UV divergences cancellation at integrand level, the ideas exposed in Ref. [100] motivated the construction of a dual representation of a local UV counter-term which cancels the divergences in the high-energy region of the loop momentum providing an integrable representation in four space-time dimensions. It is important to mention that self-energy corrections were included in the external on-shell legs, while they are usually ignored for massless particles because their integrated form vanishes in DREG due to the lack of physical scales. The procedure was implemented through the computation of the full NLO correction to $\gamma^* \to q\bar{q}(g)$ by making use of purely four-dimensional expressions also in a physical application. Furthermore, the procedure was extended to deal with arbitrary scattering amplitudes and provided a subtle physical interpretation of the energy scale entering the UV counter-term as renormalisation scale.

The extension of the FDU algorithm to deal with massive particles [96] considered a general momentum mapping for the quasi-collinear configurations and required the contribution of the self-energy corrections in order to achieve a full cancellation of IR singularities. Concerning UV divergences, UV counter-terms were constructed for self-energy and vertex corrections leading to a fully local cancellation of UV singularities. FDU was tested through the computation of NLO QCD corrections to the decay $A^* \to q\bar{q}(g)$, with massive quarks and $A = \{\phi, \gamma, Z\}$. The transition to the massless limit is smooth given that the quasi-collinear configurations of the real and vir-

tual corrections are matched at integrand level.

An interesting and relevant local renormalization study is the analyses of the most important channels for production and decay of the Higgs boson at the LHC: the $gg \to H$ and $H \to \gamma\gamma$ processes. It is well known that the amplitudes of the Hgg vertex and the Higgs decay into a photon pair are finite due to the absence of a direct interaction at tree-level in the Standard Model, nevertheless, a regularization technique and a well defined renormalization scheme are still necessary for their correct evaluation.

The implementation of LTD to the $gg \to H$ and $H \to \gamma\gamma$ scattering amplitudes at one-loop was first developed in Ref. [101], obtaining a very compact LTD representation which exhibits the same functional form for internal scalar, fermions and vector bosons. This is a non-trivial result considering that intermediate expressions with gauge bosons diverge faster in the UV than those with scalars and fermions. Additionally, a suitable counter-term was introduced that locally canceled the UV behaviour of the one-loop integrand, allowing a local renormalization through the LTD framework.

The extension from one to two loops of the properties of $H \to \gamma\gamma$ unintegrated dual amplitudes was presented in Ref. [102]. In particular, it was shown that the universality of the functional form, regardless of the nature of the internal particles, still holds at this order. Furthermore, an algorithmic way to renormalise two-loop amplitudes was presented, by locally cancelling the ultraviolet singularities at integrand-level, thus allowing a full four-dimensional numerical implementation of the method. The results were compared with analytic expressions already available in the literature, finding a perfect numerical agreement.

Related to asymptotic expansions, the LTD framework gives the advantage that dual amplitudes are supported in a Euclidean space which implies a clear hierarchy of scales and that the series expansion of the integrand commutes with the integration symbol. This property allows to expand the integrand around any parameter and to integrate, order by order, leading to the expected result. The first approach to asymptotic expansions in the LTD context was presented in Ref. [101]. The process $H \to \gamma\gamma$ was used as benchmark example to illustrate the feasibility of performing asymptotic expansions in the LTD formalism. This preliminary study was extended to other configurations [103, 104], where explicit results for the scalar two-

and three-point functions at one loop in different kinematical limits are presented. Particularly, a single expression was found that provides a general description of several asymptotic limits of the two-point function by selecting certain parameters of the expression in a convenient way.

Additional applications have been developed based on the LTD framework and strategies reported in Refs. [81, 84, 85, 88, 105]. For instance, in numerical implementations showing that the number of integration variables is independent of the number of external legs [106, 107] or exploring alternative local momentum mappings [108].

Up to this point, it was shown that LTD is a powerful framework to analyse the singular structure of scattering amplitudes directly in the loop momentum space. The most important feature is the restriction of all the IR and physical threshold singularities to a compact region, leading to a manifest distinction between physical and unphysical singularities at integrand level.

During 2019, the Loop-Tree Duality framework got some special attention by other groups [109–112]. We explored new strategies for the application of the LTD framework, furthermore, we pose a key question:

Is it possible to find explicit and more compact analytic expressions with the LTD formalism to all orders?

The development to answer this question is the mainstay of the latest results in the LTD scenario and is the starting point in the evolution of the present thesis.

Chapter 4

Open loop amplitudes and causality to all orders from the Loop-Tree Duality

In this chapter, we derive the generalization of the Loop-Tree Duality to all perturbative orders [6] with the Lorentz-invariant, and therefore reference-frame independent, dual prescription introduced in the original LTD formulation at one loop [81]. The development is applied to selected multiloop topologies with arbitrary internal configurations, managing to express them in a very compact way; furthermore, they are written in terms of convolutions of known subtopologies. The expressions obtained are entirely independent at integrand level of the initial configuration of momentum flows in the Feynman representation and, remarkably, manifestly free of noncausal singularities.

To present a general study, we work directly with scattering amplitudes in a scenario involving sets of propagators as shown in Ref. [84]. In addition, we introduce a very compact notation to consider the Feynman propagators of the union of several sets, which is denoted as

$$G_F(1,\ldots,n) = \prod_{i \in 1 \cup \ldots \cup n} (G_F(q_i))^{a_i} \ , \tag{4.1}$$

with a_i arbitrary powers. It is important to mention that from now on the powers a_i will appear only implicitly. A generic L-loop scattering amplitude,

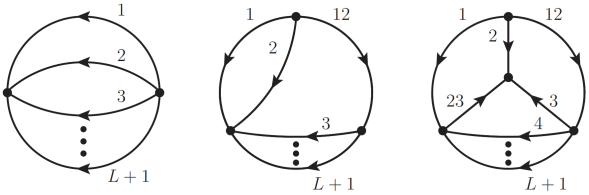

a) MLT b) NMLT c) N^{2}MLT

Figure 4.1: From left to right: Maximal Loop Topology (MLT), Next-to-Maximal Loop Topology (NMLT) and Next-to-Next-to-Maximal Loop Topology (N^{2}MLT). We recall that an arbitrary number of external legs are attached to each loop line.

with P external legs $\{p_j\}_P$ and $n = L+k$ sets of internal momenta, is defined in the Feynman representation as an integral in the Minkowski space of the L loop primitive momenta, $\{\ell_s\}_L$,

$$\mathcal{A}^{(L)}(1,\ldots,L+k) = \int_{\ell_1,\ldots,\ell_L} \mathcal{A}_F^{(L)}(1,\ldots,L+k)\,, \tag{4.2}$$

with the integrand in the Feynman representation given by

$$\mathcal{A}_F^{(L)}(1,\ldots,L+k) = \mathcal{N}(\{\ell_s\}_L,\{p_j\}_P)\; G_F(1,\ldots,L+k)\,. \tag{4.3}$$

The numerator $\mathcal{N}$ is determined by the interaction vertices in the given theory and the kind of particles that propagate; the internal structure of $\mathcal{A}_F^{(L)}$ is implicitly specified via the overall tagging of the different sets of internal momenta.

Moving forward, the one-loop LTD representation is obtained by integrating out one degree of freedom in the loop through Cauchy's residue theorem [81]. In the context of multiloop scattering amplitudes, we have to integrate one degree of freedom per loop. We follow a different tactic from the one developed in Ref. [84]. Our strategy consists of a direct iterative application of Cauchy's residue theorem, obtaining the LTD representation in terms of nested residues

$$\begin{aligned}&\mathcal{A}_D^{(L)}(1,\ldots,r;r+1,\ldots,L+k)\\ &= -2\pi\imath \sum_{i_r\in r} \mathrm{Res}(\mathcal{A}_D^{(L)}(1,\ldots,r-1;r,\ldots,L+k),\mathrm{Im}(\eta\cdot q_{i_r})<0)\,,\end{aligned} \tag{4.4}$$

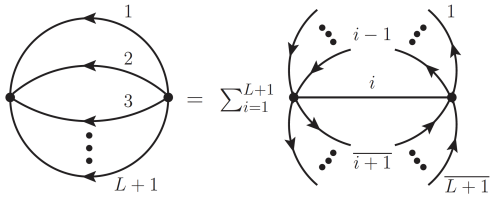

Figure 4.2: Maximal Loop Topology (left) and the corresponding open dual representation (right). All the propagators in the set i on the r.h.s. are off shell, while the on-shell cut is applied over the remaining L sets: one on-shell propagator in each set and an implicit sum over all possible on-shell configurations. Bars indicate a reversal of the momentum flow.

starting from

$$\begin{aligned}&\mathcal{A}_D^{(L)}(1;2,\ldots,L+k)\\&= -2\pi\imath \sum_{i_1\in 1} \mathrm{Res}(\mathcal{A}_F^{(L)}(1,\ldots,L+k), \mathrm{Im}(\eta\cdot q_{i_1})<0)\,,\end{aligned} \tag{4.5}$$

where $\mathcal{A}_F^{(L)}(1,\ldots,L+k)$ is the integrand in the Feynman representation. In Eq. (4.4), all sets before the semicolon are linearly independent and each of them contains exactly one propagator which has been set on shell, while all propagators belonging to sets after the semicolon remain off shell. The sum over all possible on-shell configurations in $\mathcal{A}_D^{(L)}$ is understood through the sum of residues.

In the following sections we derive the reformulation of the Loop-Tree Duality at higher orders through the analyses of several benchmark topologies to all orders. The selected multiloop topologies and their initial configurations are shown in Fig. 4.1; these topologies consider implicitly an arbitrary number of external legs, which are not drawn in the diagrams. The shorthand notation introduced above allows to express the results in the LTD formalism, regardless of the internal configuration, in a more understandable and very compact form.

4.1 Maximal Loop Topology

The Maximal Loop Topology (MLT) which is depicted in Fig. 4.2, is defined by L-loop configurations with $n = L+1$ sets of propagators, where the momenta of the propagators belonging to the first L sets depend on one

single loop momentum, $q_{i_s} = \ell_s + k_{i_s}$ with $s \in \{1, \ldots, L\}$. The momenta of the extra set, $L+1$, are given by a linear combination of all the loop momenta, $q_{i_{L+1}} = -\sum_{s=1}^{L} \ell_s + k_{i_{L+1}}$. The minus sign in front of the sum is imposed by momentum conservation. The momenta k_{i_s} and $k_{i_{L+1}}$ are linear combinations of external momenta. It is worth mentioning that at two loops ($n = 3$) this is the only possible topology, therefore, sufficient to describe any two-loop scattering amplitude.

The LTD representation of the MLT amplitude is extremely simple and symmetric

$$\begin{aligned} &\mathcal{A}^{(L)}_{\rm MLT}(1, \ldots, L+1) \\ &= \int_{\ell_1,\ldots,\ell_L} \sum_{i=1}^{L+1} \mathcal{A}^{(L)}_D(1, \ldots, i-1, \overline{i+1}, \ldots, \overline{L+1}; i) \, , \end{aligned} \tag{4.6}$$

with $\mathcal{A}^{(L)}_D(\overline{2}, \ldots, \overline{L+1}; 1)$ and $\mathcal{A}^{(L)}_D(1, \ldots, L; L+1)$ as the first and the last elements of the sum, respectively. The bars over the set labels indicate a reversal of momentum flow which is equivalent to selecting the on-shell modes with negative energy with respect to the original momentum flow.

The procedure to achieve the compact expression in Eq. (4.6) was to evaluate the nested residues, Eq. (4.4), of several representative multiloop configurations that fall into this topology category. The derived expressions allowed to identify a pattern to formulate an *Ansatz* to all orders, which finally was proven by induction. It is noteworthy that the functional form does not depend on the position of the poles in the complex plane.

In each term of the sum in the integrand of Eq. (4.6), there is one set i with all its propagators off shell, and there is one on-shell propagator in each of the other L sets. This is the necessary condition to open the multiloop amplitude into connected trees. Note also that there is an implicit sum over all possible on-shell configurations of the L sets. The LTD representation in Eq. (4.6) is displayed graphically in Fig. 4.2, and represents the basic building block entering other topologies.

The causal behavior of Eq. (4.6) is also clear and manifest. The dual representation in Eq. (4.6) becomes singular when one or more off-shell propagators eventually go on shell and generate a disjoint tree-level dual subamplitude. If these propagators belong to a set where there is already

one on-shell propagator then the discussion reduces to the one-loop case [88], also mentioned in Section 3.2. The interesting case occurs when the propagator becoming singular belongs to the set with all the propagators off shell [7]. For example, the first element of the sum in Eq. (4.6) features all the off-shell propagators in the set 1. One of those propagators might become on shell, and there are two potential singular solutions, one with positive energy and another with negative energy, depending on the magnitude and direction of the external momenta [7, 88]. The solution with negative energy represents a singular configuration where there is at least one on-shell propagator in each set. Therefore, the amplitude splits into two disjoint trees, with all the momenta over the causal on-shell cut pointing to the same direction. Abusing notation:

$$\mathcal{A}_D^{(L)}(\overline{2},\ldots,\overline{L+1};1) \overset{1\ \text{on-shell}}{\longrightarrow} \mathcal{A}_D^{(L)}(\overline{1},\overline{2},\ldots,\overline{L+1})\ . \tag{4.7}$$

The on-shell singular solution with positive energy, however, is locally entangled with the next term in Eq. (4.6) such that the full LTD representation remains nonsingular in this configuration:

$$\begin{aligned}&\mathcal{A}_D^{(L)}(\overline{2},\overline{3},\ldots,\overline{L+1};1)+\mathcal{A}_D^{(L)}(1,\overline{3},\ldots,\overline{L+1};2) \\ &\overset{(1,2)\ \text{on-shell}}{\longrightarrow} \mathcal{A}_D^{(L)}(1,\overline{2},\overline{3},\ldots,\overline{L+1})-\mathcal{A}_D^{(L)}(1,\overline{2},\overline{3},\ldots,\overline{L+1})\ .\end{aligned} \tag{4.8}$$

These local cancellations also occur with multiple power propagators. They are the known as "dual cancellations" of unphysical or noncausal singularities [7, 88, 102] and they are essential to support that the remaining causal and anomalous thresholds as well as infrared singularities are restricted to a compact region of the loop three-momenta. Causality determines that the only surviving singularities fall on ellipsoid surfaces in the loop three-momenta space [94, 95, 112], that collapse to finite segments for massless particles leading to infrared singularities. These causal singularities are bounded by the magnitude of the external momenta, thus enabling the simultaneous generation with the tree contributions describing the emission of extra radiation through suitable momentum mappings, as defined in four-dimensional unsubstraction (FDU) [80, 93, 96]. Another potential causal singularity occurs from the last term in Eq. (4.6) when all the on-shell momenta are aligned in the opposite direction over the causal on-shell cut,

$$\mathcal{A}_D^{(L)}(1,\ldots,L;L+1) \overset{L+1\ \text{on-shell}}{\longrightarrow} \mathcal{A}_D^{(L)}(1,\ldots,L+1).$$

It is also interesting to note the remarkable appealing structure that the LTD representation exhibits when expressed in terms of dual propagators. For example, the scalar MLT integral with only one single propagator in each set, i.e., the sunrise diagram at two loops, reduces to the extremely compact expression

$$\mathcal{A}^{(L)}_{\rm MLT}(1,\ldots,L+1) = \int_{\vec{\ell}_1,\ldots,\vec{\ell}_L} \frac{1}{x_{L+1}} \left(\frac{1}{\lambda^+_{L+1}} + \frac{1}{\lambda^-_{L+1}} \right) , \tag{4.9}$$

where

$$x_{L+1} = \prod_{i=1}^{L+1} 2q^{(+)}_{i,0} \ , \quad \lambda^{\pm}_{L+1} = \sum_{i=1}^{L+1} q^{(+)}_{i,0} \pm k_{L+1,0} \, , \quad \text{with} \quad k_{L+1} = \sum_{i=1}^{L+1} q_i \, ,$$

and

$$\int_{\vec{\ell}_s} \equiv -\mu^{4-d} \int \frac{d^{d-1}\ell_s}{(2\pi)^{d-1}} \ . \tag{4.10}$$

The most notable property of this expression is that it is explicitly free of unphysical singularities, and the causal singularities occur, as expected, when either λ^+_{L+1} or λ^-_{L+1} vanishes (depending on the sign of the energy component of k_{L+1}) in the loop three-momenta region where the on-shell energies are bounded, $q^{(+)}_{i,0} \leq |k_{L+1,0}|$. This property holds for powers of propagators, nonscalar integrals, more than one propagator in each set, and also for higher complexity topologies. Furthermore, Eq. (4.9) is independent of the initial momentum flows in the Feynman representation.

4.2 Next-to-Maximal Loop Topology

The multiloop topology next in complexity shown in Fig. 4.3, contains one extra set of momenta, denoted by 12, that depends on the sum of two loop momenta, $q_{i_{12}} = -\ell_1 - \ell_2 + k_{i_{12}}$. We call it Next-to-Maximal Loop topology (NMLT). This topology appears for the first time at three loops having $L+2$ sets and its LTD representation is given by the compact and factorized expression

$$\begin{aligned} &\mathcal{A}^{(L)}_{\rm NMLT}(1,\ldots,L+1,12) \\ &\quad = \mathcal{A}^{(2)}_{\rm MLT}(1,2,12) \otimes \mathcal{A}^{(L-2)}_{\rm MLT}(3,\ldots,L+1) \\ &\quad + \mathcal{A}^{(1)}_{\rm MLT}(1,2) \otimes \mathcal{A}^{(L-1)}_{\rm MLT}(\overline{3},\ldots,\overline{L+1}) \ , \end{aligned} \tag{4.11}$$

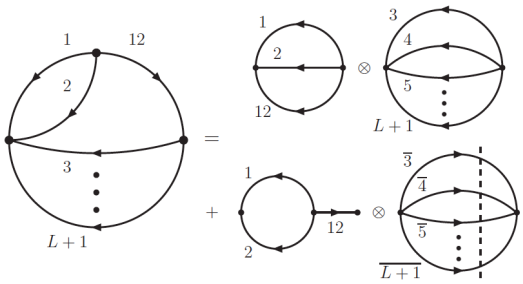

Figure 4.3: Next-to-Maximal Loop Topology (left) and its convoluted dual representation (right). Each MLT subtopology opens according to Eq. (4.6). Only the on-shell cut of the last MLT-like subtopology with reversed momentum flow is explicitly shown.

generating a total of $3L-1$ terms. The first term on the r.h.s. of Eq. (4.11) represents a convolution of the two-loop MLT subtopology involving the sets $(1,2,12)$ with the rest of the amplitude, which is also MLT. Each MLT component of the convolution opens according to Eq. (4.6). In the second term on the r.h.s. of Eq. (4.11), the set 12 remains off shell while there are on-shell propagators in either 1 or $\overline{2}$, and all the inverted sets from 3 to $L+1$ contain on-shell propagators. For example, at three loops ($L=3$), these convolutions are interpreted as

$$\mathcal{A}^{(2)}_{\rm MLT}(1,2,12)\otimes\mathcal{A}^{(1)}_{\rm MLT}(3,4) = \Big(\mathcal{A}^{(3)}_{D}(\overline{2},\overline{12},\overline{4}) + \mathcal{A}^{(3)}_{D}(1,\overline{12},\overline{4}) + \mathcal{A}^{(3)}_{D}(1,2,\overline{4}) + (\overline{4}\leftrightarrow 3)\Big) \tag{4.12}$$

and

$$\mathcal{A}^{(1)}_{\rm MLT}(1,2)\otimes\mathcal{A}^{(2)}_{\rm MLT}(\overline{3},\overline{4}) = \mathcal{A}^{(3)}_{D}(1,\overline{3},\overline{4}) + \mathcal{A}^{(3)}_{D}(\overline{2},\overline{3},\overline{4})\ . \tag{4.13}$$

In order to make the notation more readable, $\mathcal{A}^{(L)}_{\rm N^{k-1}MLT}$ and $\mathcal{A}^{(L)}_{D}$ will refer in the following to the integrand of the corresponding topology in the LTD representation; integration over the L loop momenta will be implicitly understood. An additional simplification is implemented by omitting the explicit reference to the sets with all their propagators off shell; for instance, Eq. (4.13) must be considered as

$$\mathcal{A}^{(1)}_{\rm MLT}(1,2)\otimes\mathcal{A}^{(2)}_{\rm MLT}(\overline{3},\overline{4}) = \mathcal{A}^{(3)}_{D}(1,\overline{3},\overline{4};2,12) + \mathcal{A}^{(3)}_{D}(\overline{2},\overline{3},\overline{4};1,12)\ . \tag{4.14}$$

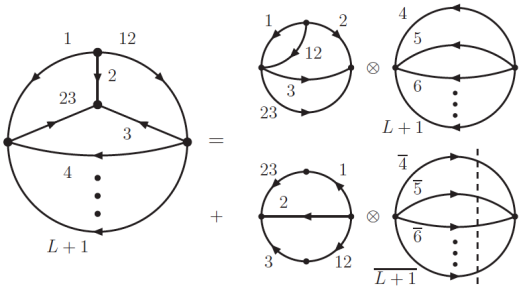

Figure 4.4: Next-to-Next-to-Maximal Loop Topology (left) and its convoluted dual representation (right). Opening according to Eq. (4.15). Only the on-shell cut of the last MLT-like subtopology with reversed momentum flow is explicitly shown.

This notation will be used in the following; the omitted sets are assumed to contain off-shell propagators only.

Causal thresholds and infrared singularities are then determined by the singular structure of the $\mathcal{A}^{(2)}_{\rm MLT}(1,2,12)$ subtopology, and by the singular configurations that split the NMLT topology into two disjoint trees with all the on-shell momenta aligned over the causal cut. Again, the singular surfaces in the loop three-momenta space are limited by the external momenta, and all the noncausal singular configurations that arise in individual contributions undergo dual cancellations.

4.3 Next-to-Next-to-Maximal Loop Topology

The last multiloop topology that we consider explicitly in this chapter is the Next-to-Next-to-Maximal Loop Topology ($\rm N^2MLT$) depicted in Fig. 4.4. At three loops, it corresponds to the so-called Mercedes-Benz topology. Besides the 12-set, we need to add an extra set denoted by 23 with $q_{i_{23}} = -\ell_2 - \ell_3 + k_{i_{23}}$. Its LTD representation is given by the following convolution of factorized subtopologies

$$\begin{aligned}
&\mathcal{A}^{(L)}_{\rm N^2MLT}(1,\ldots,L+1,12,23) \\
&\quad = \mathcal{A}^{(3)}_{\rm NMLT}(1,2,3,12,23) \otimes \mathcal{A}^{(L-3)}_{\rm MLT}(4,\ldots,L+1) \\
&\quad + \mathcal{A}^{(2)}_{\rm MLT}(1\cup 23,2,3\cup 12) \otimes \mathcal{A}^{(L-2)}_{\rm MLT}(\overline{4},\ldots,\overline{L+1}) \,. \qquad (4.15)
\end{aligned}$$

The sets $(1, 2, 3, 12, 23)$ form a NMLT subtopology. Therefore, the first component of the first term on the r.h.s. of Eq. (4.15) opens iteratively as

$$\begin{aligned}\mathcal{A}^{(3)}_{\text{NMLT}}(1,2,3,12,23) &= \mathcal{A}^{(2)}_{\text{MLT}}(1,2,12)\otimes\mathcal{A}^{(1)}_{\text{MLT}}(3,23)\\ &+ \left(\mathcal{A}^{(3)}_{D}(1,\overline{3},\overline{23})+\mathcal{A}^{(3)}_{D}(\overline{12},3,23)\right). \quad (4.16)\end{aligned}$$

The last two terms on the r.h.s. of Eq. (4.16) are fixed by the condition that the sets $(2, 3, 23)$ cannot generate a disjoint subtree. The second term on the r.h.s. of Eq. (4.15) contains a two-loop subtopology made of five sets of momenta, $\mathcal{A}^{(2)}_{\text{MLT}}(1 \cup 23, 2, 3 \cup 12)$, which are grouped into three sets and dualized through Eq. (4.6). For example, propagators in the sets 1 and 23 are not set simultaneously on shell. The number of terms generated by Eq. (4.15) is $8(L-1)$. As for the NMLT, the causal singularities of the N^{2}MLT topology are determined by its subtopologies and by the singular configurations that split the open amplitude into disjoint trees with all the on-shell momenta aligned over the causal cut. Any other singular configuration is entangled among dual amplitudes and cancels.

We want to emphasize that Eq. (4.15) accounts properly for the NMLT and MLT topologies as well, if either 23 or both 12 and 23 are taken as empty sets. At three loops, therefore, Eq. (4.15) emerges as the LTD master topology for opening any scattering amplitude from its Feynman representation. These properties provide integrand representations of scattering amplitudes that exhibit manifest causal singular structures and better numerical stability than other representations.

In Section 4.1 we presented the example of the MLT diagram with an LTD representation explicitly free of physical singularity, a causal LTD representation. In that specific case, the analytical expression is directly obtained with a proper simplification after summing over all the dual terms. However, concerning the NMLT and N^{2}MLT topologies, the path to obtain an expression explicitly free of nonphysical singularities is not so straightforward.

We refer to Ref. [113] for the explicit causal LTD representations for the NMLT and N^{2}MLT cases. The procedure followed there, was to reconstruct their analytic expression from numerical evaluations over finite fields, implicitly canceling out all unphysical singularities.

Chapter 5

Universal opening of four-loop scattering amplitudes to trees

In this chapter, we move on to the next multiloop topology in complexity and we extend the application of LTD to those topologies appearing for the first time at four loops [5]. This multiloop family is represented by three topologies which are assembled in a clever and general expression, the N^{4}MLT *universal topology*. Its LTD representation describes at once the opening of any four-loop scattering amplitude to connected trees. Also, we consider the analytic reconstruction of N^{4}MLT in terms of exclusively causal propagators [113]. For all the internal configurations considered, we achieved analytic expressions manifestly causal. These results confirm the conjecture of Section 4.1 regarding the explicit absence of noncausal singularities in the LTD representation.

5.1 The N^{4}MLT universal topology

The multiloop topologies that appear for the first time at four loops are characterized by multiloop diagrams with $L + 4$ and $L + 5$ sets of propagators. According to the classification scheme in Ref. [6], they correspond to the Next-to-Next-to-Next-to Maximal Loop Topology (N^{3}MLT) and Next-to-Next-to-Next-to-Next-to Maximal Loop Topology (N^{4}MLT). In fact, N^{4}MLT embraces in a natural way all N^{k-1}MLT configurations,

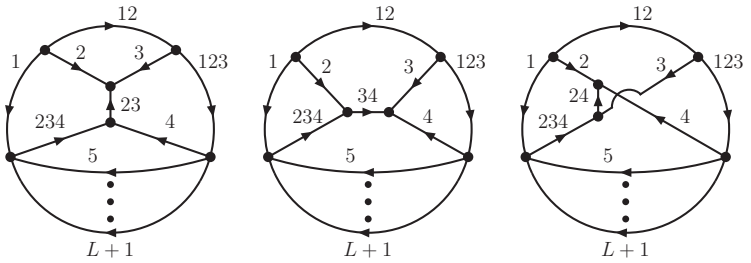

Figure 5.1: Diagrams of the N^{4}MLT family. From left to right the diagrams correspond to the t channel, the s channel and the u channel.

with $k \leq 4$.

This arrangement allows to restrict the overall assessment to the N^{4}MLT family that consists of three main topologies. These topologies were checked with `QGRAF` [114] and are shown in Fig. 5.1. Two of them are planar and one is nonplanar. We observe the similarity of these topologies with the insertion of a four-point subamplitude with trivalent vertices into a larger topology. Therefore, in order to achieve a unified description each of the three N^{4}MLT topologies are interpreted as the t-, s- and u-channels, respectively, of a *universal topology*.

The three topologies contain $L + 4$ common sets of propagators, and one extra set which is different for each of them. Each of the first L sets depends on one characteristic loop momentum ℓ_s and the momenta of their propagators have the form $q_{i_s} = \ell_s + k_{i_s}$. The remaining four common sets are established as linear combinations of all the loop momenta, explicitly

$$\begin{aligned} q_{i_{(L+1)}} &= -\sum_{s=1}^{L} \ell_s + k_{i_{(L+1)}}\,, \quad q_{i_{12}} = -\ell_1 - \ell_2 + k_{i_{12}}\,, \\ q_{i_{123}} &= -\sum_{s=1}^{3} \ell_s + k_{i_{123}}\,, \quad q_{i_{234}} = -\sum_{s=2}^{4} \ell_s + k_{i_{234}}\,, \end{aligned} \tag{5.1}$$

with $k_{i_s}, k_{i_{(L+1)}}, k_{i_{12}}, k_{i_{123}}$ and $k_{i_{234}}$ linear combinations of external momenta. The extra sets are the distinctive key to each of the channels in the universal topology. We identify the momenta of their propagators as different linear combinations of ℓ_2, ℓ_3 and ℓ_4, writing them as

$$q_{i_{rs}} = -\ell_r - \ell_s + k_{i_{rs}}\,, \quad r, s \in \{2, 3, 4\}\,, \quad r \neq s\,. \tag{5.2}$$

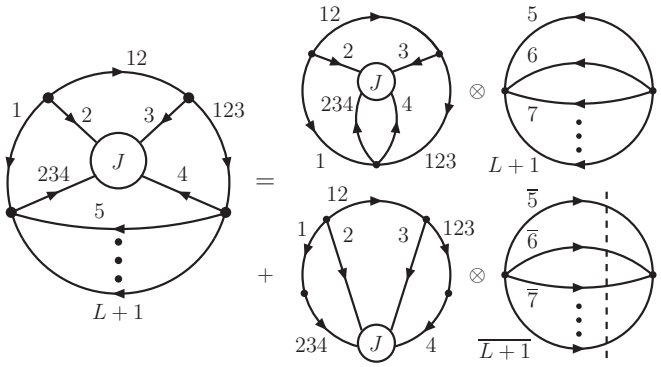

Figure 5.2: Diagrammatic representation for the factorized opening of the multiloop N^{4}MLT *universal topology*. Only the on-shell cut of the last MLT-like subtopology with reversed momentum flow is explicitly shown.

To assemble the three N^{4}MLT channels into a single topology, we define the current J that includes the three different type of sets,

$$J \equiv 23 \cup 34 \cup 24 \ . \tag{5.3}$$

Notice that due to momentum conservation, the three subsets cannot contribute to the same individual Feynman diagram but they all contribute at amplitude level. Relying on the development of this framework, the Feynman representation of the N^{4}MLT universal topology can be expressed as

$$\mathcal{A}^{(L)}_{\text{N}^4\text{MLT}} = \int_{\ell_1,\ldots,\ell_L} \mathcal{A}^{(L)}_{F}(1,\ldots,L+1,12,123,234,J) \ . \tag{5.4}$$

The dual opening of this topology fulfills a factorization identity in terms of simpler topologies similar to the one presented in Sections 4.2 and 4.3 for NMLT and N^{2}MLT respectively,

$$\begin{aligned}
&\mathcal{A}^{(L)}_{\text{N}^4\text{MLT}}(1,\ldots,L+1,12,123,234,J) \\
&= \mathcal{A}^{(4)}_{\text{N}^4\text{MLT}}(1,2,3,4,12,123,234,J) \otimes \mathcal{A}^{(L-4)}_{\text{MLT}}(5,\ldots,L+1) \\
&+ \mathcal{A}^{(3)}_{\text{N}^2\text{MLT}}(1\cup 234,2,3,4\cup 123,12,J) \otimes \mathcal{A}^{(L-3)}_{\text{MLT}}(\overline{5},\ldots,\overline{L+1}) \ .
\end{aligned} \tag{5.5}$$

This factorization identity has a clear graphical interpretation as shown in Fig. 5.2. The convolution symbol indicates that each of the convoluted components is opened independently, whereas the on-shell conditions from all components act together on the propagators that remain off shell.

An essential restriction that the selected on-shell propagators must meet, concerns the feasibility of generating disjoint trees due to the dual opening. The term $\mathcal{A}^{(4)}_{\mathrm{N^4MLT}}$ on the r.h.s. of Eq. (5.5) considers all possible configurations with four on-shell propagators in the sets $\{1, 2, 3, 4, 12, 123, 234, J\}$, while $\mathcal{A}^{(3)}_{\mathrm{N^2MLT}}$ in the second term assumes three on-shell conditions under certain constraints, as explained below. The term $\mathcal{A}^{(L-4)}_{\mathrm{MLT}}(5, \ldots, L+1)$ opens according to the MLT opening presented in Section 4.1; in the case of $\mathcal{A}^{(L-3)}_{\mathrm{MLT}}(\overline{5}, \ldots, \overline{L+1})$, all the momentum flows are reversed and all the sets contain one on-shell propagator. The reversion is imposed by the fact that, in the absence of propagators in the sets $\{12, 123, 234, J\}$, the master opening in Eq. (5.5) should coincide with the MLT opening.

The factorization identity in Eq. (5.5) is the main result of this chapter, and is the universal identity that opens any multiloop $\mathrm{N^4MLT}$ topology to connected trees. It also accounts properly for all $\mathrm{N}^{k-1}\mathrm{MLT}$ configurations with $k \leq 4$, and therefore it is the only master expression required to open any scattering amplitude of up to four loops to connected trees, independently of its internal configuration. Beyond four loops, new topologies arise that, for consistency, should include this universal topology as a particular case.

In order to prove that Eq. (5.5) holds for an arbitrary number of loops, we decompose the $\mathrm{N^4MLT}$ into two parts: the upper part in the l.h.s. of Fig. 5.2 containing the current J, which encodes the novel topological complexity arising in this class of diagrams, and the lower one, which represents a known MLT-like component. The LTD representation of the topological complexity part is computed at four loops for each specific configuration described by the current J, or equivalently, by considering the MLT-like sector as a single internal line. Then, we just need to rely on the MLT formula presented in Eq. (4.6) to complete the calculation and induct the all-order expression.

The factorized and compact form that has been presented in Eq. (5.5) is given by the exploration and selection of the most convenient order in the application of the nested residues; however, we have to mention certain arbitrariness. The dual opening of the $\mathrm{N^4MLT}$ universal topology has at least $L!$ possible representations due to the freedom in the order of the nested application of the Cauchy's residue theorem. Despite this, all the represen-

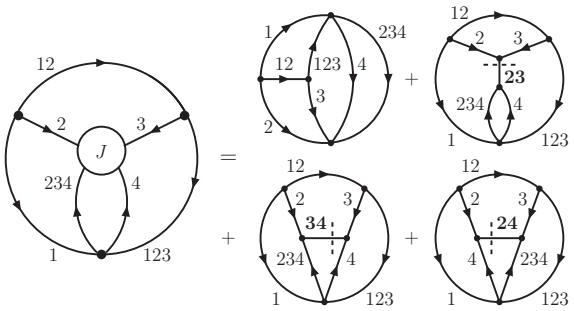

Figure 5.3: Diagrammatic representation of the four-loop subtopology, $\mathcal{A}^{(4)}_{\mathrm{N^4MLT}}(1,2,3,4,12,123,234,J)$.

tations are equivalent and lead to the same causal expression in terms of dual propagators [113].

The four-loop subtopology in Eq. (5.5) is opened as well through a factorization identity which is written in terms of simpler topologies,

$$\begin{aligned}&\mathcal{A}^{(4)}_{\mathrm{N^4MLT}}(1,2,3,4,12,123,234,J)\\&\quad=\mathcal{A}^{(4)}_{\mathrm{N^2MLT}}(1,2,3,4,12,123,234)+\sum_{\mathbf{s}\in J}\mathcal{A}^{(4)}_{D}(1,2,3,4,12,123,234,\mathbf{s})\,.\end{aligned}\tag{5.6}$$

The diagrammatic representation of Eq. (5.6) is depicted in Fig. 5.3. The first term on the r.h.s. of Eq. (5.6) consists of a four-loop N^{2}MLT subtopology and describes dual trees where all the momenta in J remain off shell, corresponding to the first diagram on the r.h.s. of Fig. 5.3. The second term on the r.h.s. of Eq. (5.6) carries contributions where propagators in either 23, 34 or 24 are set on shell. These dual trees are therefore specific to the t-, s- and u-channels. Their explicit expressions are presented below.

The three-loop subtopology on the r.h.s. of Eq. (5.5) is also opened in terms of known subtopologies through the factorized identity

$$\begin{aligned}&\mathcal{A}^{(3)}_{\mathrm{N^2MLT}}(1\cup234,2,3,4\cup123,12,J)\\&\quad=\mathcal{A}^{(3)}_{\mathrm{NMLT}}(1\cup234,2,3,4\cup123,12)+\sum_{\mathbf{s}\in J}\mathcal{A}^{(3)}_{D}(1,2,3,4,12,123,234,\mathbf{s})\,,\end{aligned}\tag{5.7}$$

which has a similar structure as Eq. (5.6). The diagrammatic representation of Eq. (5.7) is depicted in Fig. 5.4. Similarly to Fig. 5.3, the first diagram on the r.h.s. of Fig. 5.4, which represents the first term on the r.h.s. of Eq. (5.7), is a three-loop NMLT subtopology and all the propagators in J are off shell, while the remaining three diagrams are specific to each of the three channels. The NMLT subtopology is made up of 7 subsets of momenta grouped into 5 sets as follows $\{1 \cup 234, 2, 3, 4 \cup 123, 12\}$. This construction prevents, for example, that propagators in the sets 1 and 234 are set on shell simultaneously.

Turning back to Eqs. (5.6) and (5.7) in a more detailed way, the first terms on the r.h.s. of both equations are composed of dual contributions where all the propagators in J remain off shell. These J-propagators act as spectators in relation to the opening of the accompanying subtopology, and can eventually be replaced by a contact interaction to deduce the opening rule of these contributions.

Specifically, the four-loop N^{2}MLT subamplitude in Eq. (5.6) is represented by

$$\begin{aligned}
&\mathcal{A}^{(4)}_{\mathrm{N^2MLT}}(1,2,3,4,12,123,234) \\
&\qquad = \mathcal{A}^{(3)}_{\mathrm{NMLT}}(1,2,3,12,123,234) \otimes \mathcal{A}^{(1)}_{\mathrm{MLT}}(4,234) \\
&\qquad + \left[\mathcal{A}^{(2)}_{\mathrm{MLT}}(1,2,12) + \mathcal{A}^{(2)}_{\mathrm{MLT}}(1,\overline{3})\right] \otimes \mathcal{A}^{(2)}_{\mathrm{MLT}}(\overline{4},\overline{234}) \\
&\qquad + \left[\mathcal{A}^{(2)}_{\mathrm{MLT}}(\overline{123},\overline{3},12) + \mathcal{A}^{(2)}_{\mathrm{MLT}}(2,\overline{123})\right] \otimes \mathcal{A}^{(2)}_{\mathrm{MLT}}(4,234)\,. \qquad (5.8)
\end{aligned}$$

All the MLT subamplitudes that involve a number of loops equal to the number of sets, require to set propagators on shell in all the sets. The rest of NMLT and MLT subtopologies are opened according to the dual representations presented in Chapter 4.

The three-loop NMLT subtopology in Eq. (5.7) is generated from 7 subsets clustered as $\{1 \cup 234, 2, 3, 4 \cup 123, 12\}$ and its LTD representation is

$$\begin{aligned}
&\mathcal{A}^{(3)}_{\mathrm{NMLT}}(1 \cup 234, 2, 3, 4 \cup 123, 12) \\
&\qquad = \mathcal{A}^{(2)}_{\mathrm{MLT}}(1 \cup 234, 2, 12) \otimes \mathcal{A}^{(1)}_{\mathrm{MLT}}(3, 4 \cup 123) \\
&\qquad + \mathcal{A}^{(1)}_{\mathrm{MLT}}(1 \cup 234, 2) \otimes \mathcal{A}^{(2)}_{\mathrm{MLT}}(\overline{3}, \overline{4} \cup \overline{123})\,, \qquad (5.9)
\end{aligned}$$

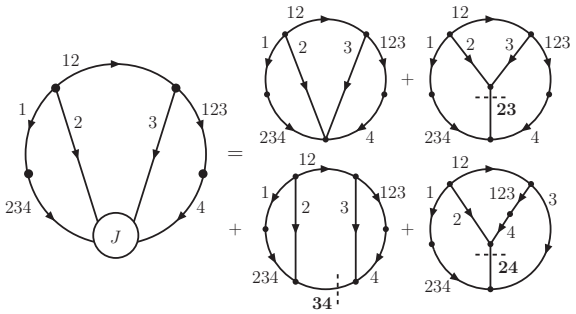

Figure 5.4: Diagrammatic representation of the three-loop subtopology $\mathcal{A}^{(3)}_{\mathrm{N^2MLT}}(1\cup 234, 2, 3, 4\cup 123, 12, J)$.

where the first term is a convolution of two MLT subtopologies, and in the second term all the propagators in the set 12 are off shell.

5.2 The t channel

The second terms in Eqs. (5.6) and (5.7) distinguish the dual configurations arising for each of the three channels when propagators with momenta in J are set on shell. We begin analyzing the dual terms related exclusively to the topology known as t channel from Fig. 5.1 (left). The contributions to the dual opening consider two specific subtopologies, one four-loop subtopology

$$\begin{aligned}
&\mathcal{A}^{(4)}_D(1,2,3,4,12,123,234,\mathbf{23})\\
&= \Big[\Big(\mathcal{A}^{(2)}_{\mathrm{MLT}}(\overline{123},\overline{3},12)+\mathcal{A}^{(2)}_{\mathrm{MLT}}(2,\overline{123})\Big)\otimes\mathcal{A}^{(1)}_D(23)\\
&+\Big(\mathcal{A}^{(2)}_{\mathrm{MLT}}(1,2,12)+\mathcal{A}^{(2)}_{\mathrm{MLT}}(1,\overline{3})\Big)\otimes\mathcal{A}^{(1)}_D(\overline{23})\Big]\otimes\mathcal{A}^{(1)}_{\mathrm{MLT}}(4,234)\ , \qquad (5.10)
\end{aligned}$$

and one three-loop subtopology

$$\begin{aligned}
&\mathcal{A}^{(3)}_D(1,2,3,4,12,123,234,\mathbf{23})\\
&\quad=\Big[\mathcal{A}^{(2)}_{\mathrm{MLT}}(\overline{4}\cup\overline{123},\overline{3},12)+\mathcal{A}^{(2)}_{\mathrm{MLT}}(2,\overline{4}\cup\overline{123})\Big]\otimes\mathcal{A}^{(1)}_D(23)\\
&\quad+\Big[\mathcal{A}^{(2)}_{\mathrm{MLT}}(1\cup 234,2,12)+\mathcal{A}^{(2)}_{\mathrm{MLT}}(1\cup 234,\overline{3})\Big]\otimes\mathcal{A}^{(1)}_D(\overline{23})\ , \qquad (5.11)
\end{aligned}$$

contribution obtained from Eqs. (5.6) and (5.7), respectively. Notice that both expressions, Eqs. (5.10) and (5.11), contain on-shell propagators in the set 23, having contributions with the original momentum flow, 23, and the reversed one $\overline{23}$.

5.3 The s channel

In order to obtain the terms that characterize the s channel shown in Fig. 5.1 (center), we set on shell a propagator in the set 34. The four-loop subtopology is given by

$$\begin{aligned}\mathcal{A}_D^{(4)}(1,2,3,4,12,123,234,\mathbf{34}) = \Big[&\mathcal{A}^{(3)}_{\rm NMLT}(1,2,3,12,123) \\ &+ \mathcal{A}^{(3)}_{\rm MLT}(\overline{3},\overline{123},234) + \mathcal{A}^{(2)}_{\rm MLT}(1,2,12)\otimes\mathcal{A}^{(1)}_D(\overline{4}) \\ &+ \mathcal{A}^{(1)}_{\rm MLT}(3\cup\overline{4},123)\otimes\mathcal{A}^{(2)}_{\rm MLT}(\overline{12},234)\Big]\otimes\mathcal{A}^{(1)}_D(\overline{34}) \\ &+ \Big[\mathcal{A}^{(1)}_{\rm MLT}(3\cup\overline{4},123)\otimes\mathcal{A}^{(2)}_{\rm MLT}(1,\overline{234}) \\ &+ \mathcal{A}^{(1)}_{\rm MLT}(1,2\cup\overline{234})\otimes\mathcal{A}^{(2)}_{\rm MLT}(4,\overline{123})\Big]\otimes\mathcal{A}^{(1)}_D(34)\,.\end{aligned} \tag{5.12}$$

This expression is more involved than the corresponding one in the t channel, because the loop momentum ℓ_4 is found in three sets, while in the t channel ℓ_4 is located in two sets only.

By contrast, for the three-loop subamplitude we observe a very symmetric structure which allows to avoid any momentum flow reversion. In this case, we end up with an expression that only depends on the original momentum flow of the set 34,

$$\begin{aligned}&\mathcal{A}_D^{(3)}(1,2,3,4,12,123,234,\mathbf{34}) \\ &\qquad = \mathcal{A}^{(1)}_{\rm MLT}(1\cup234,2)\otimes\mathcal{A}^{(1)}_{\rm MLT}(3,4\cup123)\otimes\mathcal{A}^{(1)}_D(34)\,.\end{aligned} \tag{5.13}$$

Given the structure of this subtopology and observed in Fig. 5.4, it is manifest that propagators in 12 and 34 cannot become on shell simultaneously without generating a disjoint tree.

5.4 The u channel

Moving on to the last terms associated to the nonplanar topology known as u channel Fig. 5.1 (right), the LTD representation of the four-loop subam-

plitude with on-shell propagators in the set 24 reads

$$\begin{aligned}
&\mathcal{A}_D^{(4)}(1,2,3,4,12,123,234,\mathbf{24}) \\
&\quad= \Big[\mathcal{A}^{(3)}_{\rm NMLT}(1,2,3,12,123) + \mathcal{A}^{(1)}_{\rm MLT}(1,2\cup\overline{4})\otimes\mathcal{A}^{(2)}_{\rm MLT}(\overline{123},234) \\
&\quad+ \mathcal{A}^{(1)}_{\rm MLT}(3\cup\overline{234},123)\otimes\mathcal{A}^{(2)}_{\rm MLT}(1,\overline{4})\Big]\otimes\mathcal{A}^{(1)}_D(\overline{24}) \\
&\quad+ \Big[\mathcal{A}^{(2)}_{\rm MLT}(1,2,12)\otimes\mathcal{A}^{(1)}_{\rm MLT}(\overline{234}) + \mathcal{A}^{(3)}_{\rm MLT}(4,\overline{3},\overline{123}) \\
&\quad+ \mathcal{A}^{(1)}_{\rm MLT}(3\cup\overline{234},123)\otimes\mathcal{A}^{(2)}_{\rm MLT}(4,\overline{12})\Big]\otimes\mathcal{A}^{(1)}_D(24)\,. \qquad (5.14)
\end{aligned}$$

This subtopology is also not as compact as the expression for the t channel given that ℓ_4 is also present in three different sets. For the three-loop subamplitude, we find,

$$\begin{aligned}
&\mathcal{A}_D^{(3)}(1,2,3,4,12,123,234,\mathbf{24}) \\
&\quad= \Big[\mathcal{A}^{(2)}_{\rm MLT}(1\cup234,\overline{4}) + \mathcal{A}^{(2)}_{\rm MLT}(234,\overline{123})\Big]\otimes\mathcal{A}^{(1)}_D(\overline{24}) \\
&\quad+ \Big[\mathcal{A}^{(2)}_{\rm MLT}(1\cup234\cup\overline{3},2,12) + \mathcal{A}^{(2)}_{\rm MLT}(\overline{3},\overline{4}\cup\overline{123}) \\
&\quad+ \mathcal{A}^{(2)}_{\rm MLT}(4\cup123,\overline{12}) + \mathcal{A}^{(2)}_{\rm MLT}(\overline{1},123)\Big]\otimes\mathcal{A}^{(1)}_D(24)\,. \qquad (5.15)
\end{aligned}$$

5.5 Common features of the N^{4}MLT channels

All these results are consistent with the absence of disjoint trees. We would like to comment on the fact that repeated propagators from self-energy insertions are treated as single propagators raised to specific powers and are not considered to generate disjoint trees when the repeated propagator is set on shell.

Notice that the number of trees in the LTD forest can also be computed through the combinatorial exercise of selecting, from the full list of sets, all possible subsets of L elements that do not generate disjoint trees. For the individual t, s and u channels the number of terms calculated in this way are $5(8L-17)$, $15(3L-7)$ and $9(5L-11)$, respectively, and $82L-187$ for the N^{4}MLT universal topology, in agreement with the number of dual contributions generated by Eq. (5.5). The momentum flows of the on-shell propagators, however, can only be determined through the nested residues.

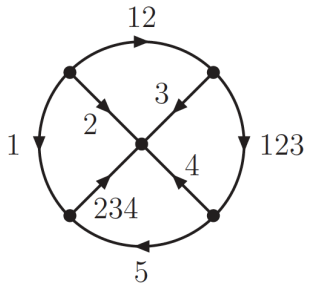

Figure 5.5: Diagrammatic representation of four loops with one four-particle vertex, N^{3}MLT.

5.6 Causal representations of the N^{4}MLT universal topology

In this section, we present explicit causal representations of selected configurations that can be described through very compact expressions. We consider, in the first place, the multi-loop N^{3}MLT configuration shown in Fig. 5.5 with one internal propagator in each loop set and five external momenta

$$\begin{aligned}&\mathcal{A}^{(L)}_{\mathrm{N^3MLT}}(1,\ldots,L+4)\\&=\int_{\ell_1,\cdots,\ell_L}\mathcal{N}(\{\ell_s\}_L,\{p_j\}_P)\;G_F(1,\ldots,L+1,12,123,234)\;,\end{aligned}\tag{5.16}$$

where the internal momenta are defined in Eq. (5.1). Its LTD representation is obtained through the universal N^{4}MLT expression in Eq. (5.5) by considering J as an empty set, or equivalently, by substituting J by a contact interaction. After computing the nested residues and adding them all together, the dual causal representation reads

$$\mathcal{A}^{(L)}_{\mathrm{N^3MLT}}(1,\ldots,L+4)=\int_{\vec{\ell}_1,\cdots,\vec{\ell}_L}\frac{\mathcal{N}_{\mathrm{N^3MLT}}(\{q^{(+)}_{s,0},k_{j,0}\})}{x_{L+4}\left(\prod_{p=1}^{13}\lambda_p^+\lambda_p^-\right)}\;,\tag{5.17}$$

where the integrand is a function of the on-shell energies,

$$q^{(+)}_{s,0}=\sqrt{\mathbf{q}_s^2+m_s^2-\imath 0},\quad\text{with}\quad s\in[1,\ldots,L+4],$$

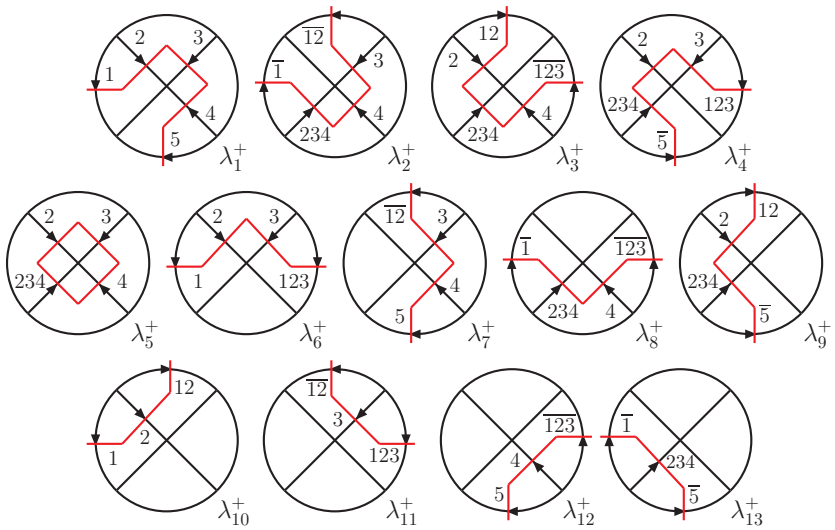

Figure 5.6: Causal configurations of the N^{3}MLT topology. The λ_p^- configurations are obtained by reversing the momentum flows of the corresponding λ_p^+ configurations shown here. The set number 5 accounts for all the propagators in the sets 5 to $L+1$.

and linear combinations of the energy components of external momenta, $k_{j,0}$. The integrand in Eq. (5.17) is written in terms of

$$x_{L+4} = \prod_{s=1}^{L+4} 2q_{s,0}^{(+)} \ , \tag{5.18}$$

and thirteen causal propagators, $1/\lambda_p^{\pm}$, with

$$\begin{aligned}
\lambda_1^{\pm} &= q^{(+)}_{(1,\ldots,L+1),0} \pm k_{L+1,0} \ , \\
\lambda_2^{\pm} &= q^{(+)}_{(1,12,3,4,234),0} \pm (k_{234} - k_{12})_0 \ , \\
\lambda_3^{\pm} &= q^{(+)}_{(2,4,12,123,234),0} \pm (k_{12} + k_{234} - k_{123})_0 \ , \\
\lambda_4^{\pm} &= q^{(+)}_{(2,3,123,234,5,\ldots,L+1),0} \pm (k_{123} + k_{234} - k_{L+1})_0 \ , \\
\lambda_5^{\pm} &= q^{(+)}_{(2,3,4,234),0} \pm k_{234,0} \ , \\
\lambda_6^{\pm} &= q^{(+)}_{(1,2,3,123),0} \pm k_{123,0} \ , \\
\lambda_7^{\pm} &= q^{(+)}_{(12,3,4,\ldots,L+1),0} \pm (k_{L+1} - k_{12})_0 \ ,
\end{aligned}$$

$$
\begin{aligned}
\lambda_8^{\pm} &= q^{(+)}_{(1,4,123,234),0} \pm (k_{234} - k_{123})_0 \ , \\
\lambda_9^{\pm} &= q^{(+)}_{(2,12,234,5,\ldots,L+1),0} \pm (k_{12} + k_{234} - k_{L+1})_0 \ , \\
\lambda_{10}^{\pm} &= q^{(+)}_{(1,2,12),0} \pm k_{12,0} \ , \\
\lambda_{11}^{\pm} &= q^{(+)}_{(12,3,123),0} \pm (k_{123} - k_{12})_0 \ , \\
\lambda_{12}^{\pm} &= q^{(+)}_{(123,4,\ldots,L+1),0} \pm (k_{L+1} - k_{123})_0 \ , \\
\lambda_{13}^{\pm} &= q^{(+)}_{(1,234,5,\ldots,L+1),0} \pm (k_{234} - k_{L+1})_0 \ ,
\end{aligned}
\tag{5.19}
$$

where we have defined $q^{(+)}_{\alpha,0} = \sum_{i\in\alpha} q^{(+)}_{i,0}$. As explained in Refs. [6, 113], these propagators are causal because they are constructed from sums of positive on-shell energies exclusively, and they represent potential singular configurations in which the momentum flows of the internal propagators are aligned in the same direction. The causal propagators appear in pairs because there are two opposite directions to consider for each aligned configuration.

A graphical representation of these causal configurations is shown in Fig. 5.6. All other linear combinations of on-shell energies do not have a physical interpretation in terms of causality, and are cancelled analytically in the sum over nested residues of the LTD representation. As a result, the straightforward application of LTD leads directly to an expression, Eq. (5.17), which is manifestly causal. In addition, the causal expression is independent of the initial flow assignments of the internal momenta, and of the order of the nested application of Cauchy's residue theorem.

The numerator of the integrand in Eq. (5.17), $\mathcal{N}_{\mathrm{N^3MLT}}(\{q^{(+)}_{s,0}, k_{j,0}\})$, is a lengthy polynomial in the on-shell and external energies. For example, it is a polynomial of degree nine for the scalar integral. A more suitable causal expression can be obtained by reinterpreting Eq. (5.17) in terms of a number of entangled thresholds equal to the difference between the number of propagators and the number of loops by, e.g., analytical reconstruction from numerical evaluation over finite fields [115–117] as defined in Ref. [113].

The N^{3}MLT expression in Eq. (5.17) is analytically reconstructed by matching all combinations of four thresholds that are causally compatible with

each other

$$\mathcal{A}^{(L)}_{\mathrm{N^3MLT}}(1,\ldots,L+4) = \int_{\vec{\ell}_1,\cdots,\vec{\ell}_L} \frac{1}{x_{L+4}} \sum_{\sigma} \frac{\mathcal{N}_{\sigma(i_1,\ldots,i_4)}(\{q^{(+)}_{s,0}, k_{j,0}\})}{\lambda^{h_{\sigma(i_1)}}_{\sigma(i_1)} \lambda^{h_{\sigma(i_2)}}_{\sigma(i_2)} \lambda^{h_{\sigma(i_3)}}_{\sigma(i_3)} \lambda^{h_{\sigma(i_4)}}_{\sigma(i_4)}} , \tag{5.20}$$

where $\lambda^{h_{\sigma(i)}}_{\sigma(i)} \in \{\lambda^{\pm}_p\}_{p=1,\ldots,13}$, and the numerators $\mathcal{N}_{\sigma(i_1,\ldots,i_4)}$ are of the same polynomial order as the original numerator in the Feynman representation, e.g., they are constants for scalar integrals. To simplify the discussion, we will present explicit results only for scalar integrals because they fully encode all the compatible causal matchings. For example, given a quadratic numerator, we can use the identity

$$(q_{i,0})^2 \, G_F(q_i) = 1 + \left(q^{(+)}_{i,0}\right)^2 G_F(q_i) \, . \tag{5.21}$$

The first term on the r.h.s. generates a scalar integral with one propagator less than the original integral, while the second term introduces a factor $\left(q^{(+)}_{i,0}\right)^2$ which is not modified by the application of the Cauchy's residue theorem. Both integrals, however, are described by the same set of causal thresholds. In general, tensor reduction commutes with LTD and can be used to deal with tensor integrals.

The explicit expression that we obtain for the scalar N^{3}MLT is very compact:

$$\begin{aligned}\mathcal{A}^{(L)}_{\mathrm{N^3MLT}}(1,\ldots,L+4) &= \int_{\vec{\ell}_1,\cdots,\vec{\ell}_L} \frac{1}{x_{L+4}} \Big[\mathcal{F}^{(L+4)}_{(1,5,6,7,10,11,12,13)} + \mathcal{F}^{(L+4)}_{(2,5,7,8,11,12,13,10)} \\ &+ \mathcal{F}^{(L+4)}_{(3,5,8,9,12,13,10,11)} + \mathcal{F}^{(L+4)}_{(4,5,9,6,13,10,11,12)} + L^+_{(6,10,11)} L^-_{(8,12,13)} \\ &+ L^-_{(7,11,12)} L^+_{(9,13,10)} + L^+_{10} L^-_{11} L^+_{12} L^-_{13} + (\lambda^+_p \leftrightarrow \lambda^-_p) \Big] \, ,\end{aligned} \tag{5.22}$$

where

$$\mathcal{F}^{(L+4)}_{(1,5,6,7,10,11,12,13)} = L^+_1 \left(L^+_5 + L^-_{13}\right) \left(L^+_{(6,10,11)} + L^+_{(7,11,12)} + L^+_{10} L^+_{12}\right) \, , \tag{5.23}$$

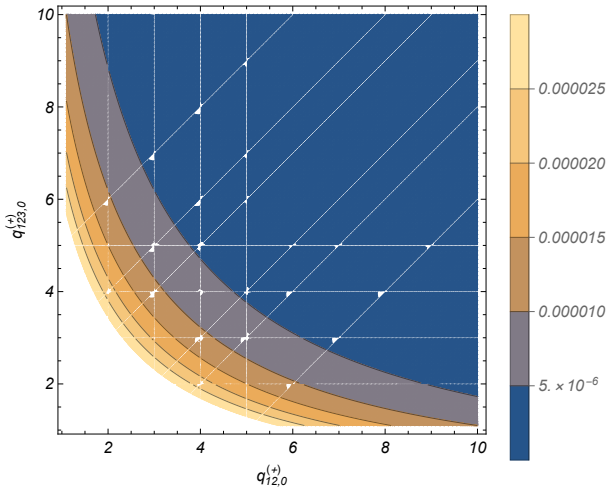

Figure 5.7: Integrand-level behaviour of the noncausal LTD representation of a four-loop N^{3}MLT diagram. White lines indicate the position of noncausal thresholds.

with

$$L_i^{\pm} = \frac{1}{\lambda_i^{\pm}} \ , \qquad L^{\pm}_{(i,j,k)} = L_i^{\pm}\left(L_j^{\pm} + L_k^{\pm}\right) \ . \tag{5.24}$$

The function $\mathcal{F}^{(L+4)}$ encodes four causal configurations that are obtained by permutation of the arguments. The number of terms generated by Eq. (5.5) scales as $3(8L-17)$, i.e., 45 terms at four loops, while the number of terms generated by Eq. (5.22) equals 98 regardless of the number of loops. The numerical performance of Eq. (5.22) is, in addition, a factor 2 to 8 faster than Eq. (5.5) at four loops, and even three orders of magnitude faster than Eq. (5.17). We have estimated the numerical performance by comparing the timings of evaluating the integrands at 1000 random points. Similar relative timings are observed for the rest of the configurations presented in this chapter.

Let us emphasize that the most significant advantage of Eq. (5.22) with respect to Eq. (5.5) stems from the core difference between them, the presence or absence of noncausal singularities. The straightforward application of the nested residue generates multiple threshold singularities, nevertheless, with a clever analytical rearrangement, the absence of noncausal singularities is achieved and leads to a causal representation which is more efficient and numerically stable numerically in the entire integration domain.

To illustrate the impact of noncausal singularities, we present in Fig. 5.7 the integrand of the dual representation of the N^{3}MLT vacuum diagram ($k_{j,0} = 0$) as a function of the two on-shell energies $q^{(+)}_{12,0}$ and $q^{(+)}_{123,0}$ where the remaining on-shell energies are set at fixed values, $q^{(+)}_{i,0} = 1$ for $i = 1, \ldots, 5$ and $q^{(+)}_{234,0} = 2$. The white lines represent the location of the noncausal thresholds which arise due to the denominators of the type

$$\frac{1}{q^{(+)}_{12,0} - q^{(+)}_{i,0}}, \quad \frac{1}{q^{(+)}_{123,0} - q^{(+)}_{i,0}} \quad \text{and} \quad \frac{1}{q^{(+)}_{12,0} - q^{(+)}_{123,0} \pm q^{(+)}_{i,0}}.$$

Additionally, to clarify the meaning of the noncausal thresholds in Fig. 5.7, we study one of the singularities by fixing $q^{(+)}_{123,0}$ and scanning over $q^{(+)}_{12,0}$. The results of noncausal and causal evaluations of the N^{3}MLT configurations are displayed in Fig. 5.8 in the left and right plots, respectively. In the left graph we can observe numerical instabilities of the four-loop N^{3}MLT integrand which arise due to noncausal singularities; an opposite behaviour is displayed in the right graph, showing a remarkable numerical stability in the causal representations. Similar findings were reported in Ref. [113], where explicit causal representations of up to N^{2}MLT complexity were presented.

Returning to the LTD representation in Eq. (5.5), it is universal and valid regardless of the internal configuration, while the causal representation is specific to the details of the configuration under consideration, e.g., the number of propagators in each loop set. The number of terms for a given N^{k-1}MLT topology in Eq. (5.5) scales with the number of loops and linearly with the number of propagators per loop set, but the sum over residues, equivalently over internal propagators, is implicitly accounted in this expression.

Concerning the causal representation, the number of terms for a given N^{k-1}MLT topology is independent of the number of loops but requires to specify additional causal thresholds and additional causal entanglements when more internal propagators are considered. In this respect, external momenta attached to interaction vertices that connect different loop sets do not alter the number of internal propagators and therefore the complexity of the causal representation. We will exploit this feature in the following to simplify the discussion of the causal representation of the N^{4}MLT topol-

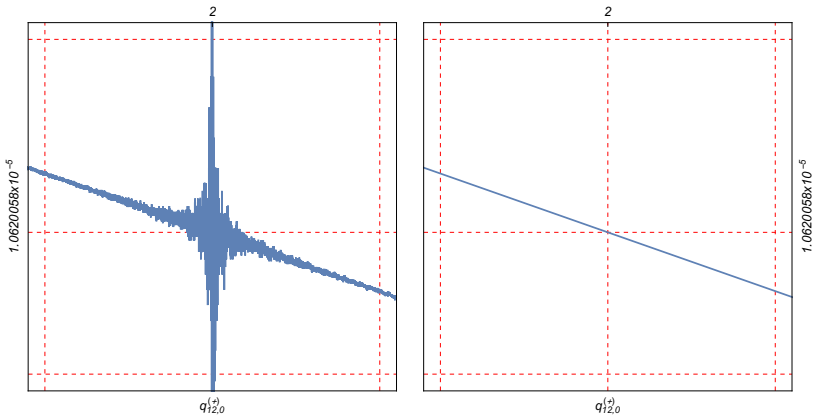

Figure 5.8: Numerical instabilities of the four-loop N^{3}MLT integrand which arise due to noncausal singularities (left), which are absent in the causal representations (right).

ogy. The full causal expressions with external momenta can be deduced from the causal representation of the vacuum configuration by matching the momentum flows of the entangled thresholds.

Let us then consider the t-channel of the N^{4}MLT universal topology

$$\mathcal{A}^{(L)}_{\mathrm{N^4MLT}}(1,\ldots,L+4,23) = \int_{\ell_1,\cdots,\ell_L} \mathcal{N}(\{\ell_s\}_L,\{p_j\}_N)\, G_F(1,\ldots,L+4,23)\ , \tag{5.25}$$

again with only one propagator per set, and six external particles. The direct LTD representation is obtained through the Eq. (5.5), that leads to a causal expression after all the nested residues are summed up together, i.e.

$$\mathcal{A}^{(L)}_{\mathrm{N^4MLT}}(1,\ldots,L+4,23) = \int_{\vec{\ell}_1,\cdots,\vec{\ell}_L} \frac{\mathcal{N}_{\mathrm{N^4MLT}}(\{q^{(+)}_{s,0},k_{j,0}\})}{x_{t,L+5}\left(\prod_{p=1}^{22}\lambda^+_p\lambda^-_p\right)}\ , \tag{5.26}$$

where $x_{t,L+5} = 2q^{(+)}_{23,0}\,x_{L+4}$. The formulation provided in Eq. (5.26) depends on the causal propagators already defined for the N^{3}MLT configuration in Eq. (5.19) in addition to nine extra causal propagators that depend on $q^{(+)}_{23,0}$

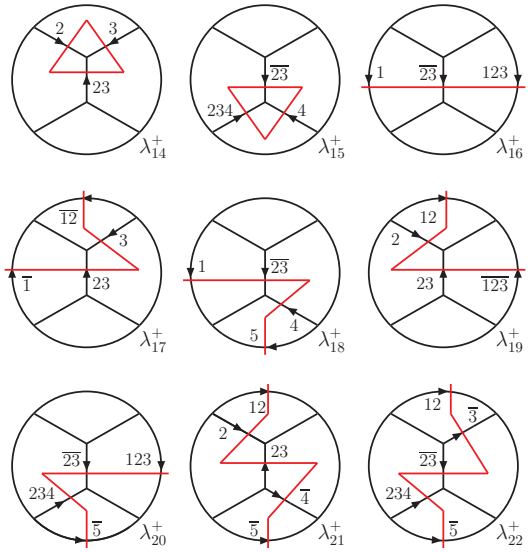

Figure 5.9: Extra causal configurations of the t-channel of the N^{4}MLT topology.

with:

$$
\begin{aligned}
\lambda^{\pm}_{14} &= q^{(+)}_{(2,3,23),0} \pm k_{23,0} \ , \\
\lambda^{\pm}_{15} &= q^{(+)}_{(4,234,23),0} \pm (k_{234} - k_{23})_0 \ , \\
\lambda^{\pm}_{16} &= q^{(+)}_{(1,123,23),0} \pm (k_{123} - k_{23})_0 \ , \\
\lambda^{\pm}_{17} &= q^{(+)}_{(1,3,12,23),0} \pm (k_{23} - k_{12})_0 \ , \\
\lambda^{\pm}_{18} &= q^{(+)}_{(1,4,\ldots,L+1,23),0} \pm (k_{L+1} - k_{23})_0 \ , \\
\lambda^{\pm}_{19} &= q^{(+)}_{(2,12,123,23),0} \pm (k_{12} + k_{23} - k_{123})_0 \ , \\
\lambda^{\pm}_{20} &= q^{(+)}_{(123,234,5,\ldots,L+1,23),0} \pm (k_{123} + k_{234} - k_{L+1} - k_{23})_0 \ , \\
\lambda^{\pm}_{21} &= q^{(+)}_{(2,4,\ldots,L+1,12,23),0} \pm (k_{12} + k_{23} - k_{L+1})_0 \ , \\
\lambda^{\pm}_{22} &= q^{(+)}_{(3,5,\ldots,L+1,12,234,23),0} \pm (k_{234} + k_{12} - k_{23} - k_{L+1})_0 \ .
\end{aligned}
\tag{5.27}
$$

The corresponding configurations are depicted in Fig. 5.9.

The numerator in Eq. (5.26) is now a polynomial of degree seventeen for the scalar integral. Aiming for a more manageable expression we reinterpret Eq. (5.17) in terms of all the entangled configurations with five causal

thresholds. The forthcoming analysis is restricted to the vacuum configuration ($\lambda_p^+ = \lambda_p^-$) in order to have a clear overview of the causal structure.

Applying the reconstruction algorithm defined in Ref. [113] to the causal expression found in Eq. (5.26), we obtain an overall structure similar to Eq. (5.22) and a very compact result,

$$\begin{aligned}\mathcal{A}^{(L)}_{\mathrm{N^4MLT}}(1,\ldots,L+4,23) = -\int_{\vec{\ell}_1,\cdots,\vec{\ell}_L} \frac{2}{x_{t,L+5}} \\ \Big[\mathcal{F}^{(L+5)}_{(1,5,6,7,10,11,12,13,14,15,18)} + \mathcal{F}^{(L+5)}_{(2,5,7,8,11,12,13,10,15,14,17)} \\ + \mathcal{F}^{(L+5)}_{(3,5,8,9,12,13,10,11,15,14,19)} + \mathcal{F}^{(L+5)}_{(4,5,9,6,13,10,11,12,14,15,20)} \\ + \mathcal{F}^{(L+5)}_{(21,18,19,7,14,11,12,9,13,15,10)} + \mathcal{F}^{(L+5)}_{(22,17,20,7,15,12,11,9,10,14,13)} \\ + \mathcal{G}^{(L+5)}_{(10,14,6,13,11,12,15,8)} + \mathcal{G}^{(L+5)}_{(10,11,12,13,14,15,17,18)} \\ + \mathcal{G}^{(L+5)}_{(12,13,10,11,15,14,20,19)} + \big(L_{(6,10,11)} + L_{(17,10,14)} \\ + L_{(19,11,14)}\big)\big(L_{(8,12,13)} + L_{(18,13,15)} + L_{(20,12,15)}\big) L_{16}\Big] ,\end{aligned} \tag{5.28}$$

that is written in terms of permutations of the arguments of the two functions

$$\begin{aligned}\mathcal{F}^{(L+5)}_{(1,\ldots,11)} = L_1 \left(L_{(2,9,10)} + L_{(8,9,11)} + L_{10}\, L_{11}\right) \\ \left(L_{(3,5,6)} + L_{(4,6,7)} + L_5\, L_7\right) ,\end{aligned} \tag{5.29}$$

and

$$\mathcal{G}^{(L+5)}_{(1,\ldots,8)} = (L_1 + L_5)\; L_{(3,4,6)}\, L_{(7,2,8)} \; . \tag{5.30}$$

Notice that, for example

$$\mathcal{F}^{(L+5)}_{(1,5,6,7,10,11,12,13,14,15,18)}\Big|_{L_{14}\to 1,(L_{15},L_{18})\to 0} = \mathcal{F}^{(L+4)}_{(1,5,6,7,10,11,12,13)} \; , \tag{5.31}$$

thus ensuring the consistency of Eq. (5.28) with Eq. (5.22).

Moving on to the next topology, the s-channel is obtained just by a clockwise rotation of the t-channel and therefore by a permutation of the arguments

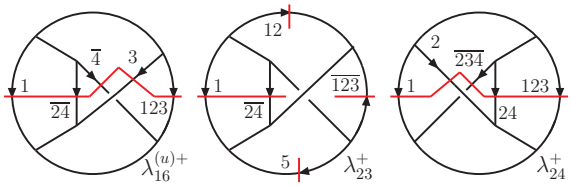

Figure 5.10: Extra causal configurations of the u-channel of the N^{4}MLT topology due to nonplanarity.

of the causal propagators that are channel specific

$$
\begin{aligned}
&1/\lambda_p^{\pm}(1,2,3,4,5\cdots(L+1),12,123,234,34) \qquad (5.32)\\
&\quad = 1/\lambda_p^{\pm}(\overline{5}\cdots(\overline{L+1}),234,2,3,123,\overline{1},12,4,23)\ , \qquad p\in[14,22]\ .
\end{aligned}
$$

This means that in Eq. (5.27) it is enough to make, for example, replacements similar to

$$
\begin{aligned}
&\lambda_{14}^{\pm}\to q^{(+)}_{(3,4,34),0}\pm k_{34,0}\ ,\\
&\lambda_{18}^{\pm}\to q^{(+)}_{(1,12,234,34),0}\pm(k_{234}-k_{12}-k_{34})_0\ ,
\end{aligned}
\qquad (5.33)
$$

in order to obtain the corresponding causal representation.

For the u-channel, the causal propagators are obtained from the t-channel through the substitution $23\to 24$ and by the exchange $3\leftrightarrow 4$ or $2\leftrightarrow 234$ (123 remains invariant):

$$
\begin{aligned}
&\lambda_p^{\pm}(1,\ldots,L+1,12,123,234,24)\\
&\qquad\qquad = \lambda_p^{\pm}(3\leftrightarrow 4,23\to 24)\ , \quad p\in[14,15,17,18,22]\ ,\\
&\lambda_p^{\pm}(1,\ldots,L+1,12,123,234,24)\\
&\qquad\qquad = \lambda_p^{\pm}(2\leftrightarrow 234,23\to 24)\ , \quad p\in[19,20,21]\ .
\end{aligned}
\qquad (5.34)
$$

There are, however, three new configurations that arise due to the fact that the u-channel is nonplanar. These new configurations are shown in Fig. 5.10 and are described by the following causal propagators

$$
\begin{aligned}
&\lambda_{16}^{(u)\pm} = q^{(+)}_{(1,\ldots,4,123),0}\pm k_{123,0}\ ,\\
&\lambda_{23}^{\pm} = q^{(+)}_{(1,5,\ldots,L+1,12,123,24),0}\pm(k_{L+1}+k_{12}-k_{123}-k_{24})_0\ ,\\
&\lambda_{24}^{\pm} = q^{(+)}_{(1,2,123,234,24),0}\pm(k_{123}-k_{234}+k_{24})_0\ .
\end{aligned}
\qquad (5.35)
$$

The causal representation of the u-channel has a very similar structure to Eq. (5.28),

$$\begin{aligned}\mathcal{A}^{(L)}_{\mathrm{N^4MLT}}(1,\dots,L+4,24) = -\int_{\vec{\ell}_1,\cdots,\vec{\ell}_L} \frac{2}{x_{u,L+5}} \Big[& \mathcal{F}^{(L+5)}_{(1,5,6,7,10,11,12,13,14,15,18)} \\ & + \mathcal{F}^{(L+5)}_{(2,5,7,8,11,12,13,10,15,14,17)} + \mathcal{F}^{(L+5)}_{(3,5,8,9,12,13,10,11,14,15,19)} \\ & + \mathcal{F}^{(L+5)}_{(4,5,9,6,13,10,11,12,15,14,20)} + \mathcal{F}^{(L+5)}_{(21,18,20,7,14,12,11,9,13,15,10)} \\ & + \mathcal{F}^{(L+5)}_{(22,17,19,7,15,11,12,9,10,14,13)} + \mathcal{F}^{(L+5)}_{(16,18,17,6,14,10,11,8,13,15,12)} \\ & + \mathcal{F}^{(L+5)}_{(24,20,19,6,15,11,10,8,12,14,13)} + \mathcal{F}^{(L+5)}_{(23,19,20,17,12,14,10,18,15,11,13)} \\ & + L_{10}\, L_{12}\, L_{15}\, (L_{11}\, L_{13} + L_{11}\, L_{14} + L_{13}\, L_{14}) \Big] \,, \end{aligned} \tag{5.36}$$

where $x_{u,L+5} = 2q^{(+)}_{24,0}\, x_{L+4}$.

Chapter 6

From five-loop scattering amplitudes to open trees with the LTD

It has been shown in Chapters 4 and 5 that the dual opening obtained by applying the nested residues, through the LTD framework, enables to write any loop integral or scattering amplitude in a convenient factorized way. Any $\mathrm{N}^k\mathrm{MLT}$ topology can be reduced to convolutions of $\mathrm{N}^j\mathrm{MLT}$ and MLT subtopologies (with $j < k$). Furthermore, the singular structure of the more complex topologies is constrained by these factorization properties, thus simplifying their treatment and cancellation.

In this chapter we delve into the application of the LTD approach to describe families of multiloop topologies that appear for the first time at five loops [1]. Following the strategies in Chapter 5, the analysis of four-loop topologies, we define here a $\mathrm{N}^7\mathrm{MLT}$ *universal topology* that allows to generate the LTD representation of any possible five-loop Feynman diagram or scattering amplitude. We exploit the recursive formulation in terms of simpler subtopologies and MLT insertions, in order to extract the main features of the more complex diagrams.

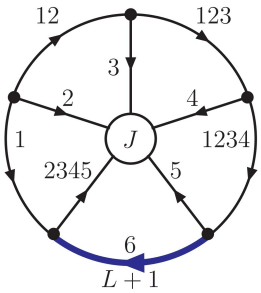

Figure 6.1: Diagrammatic representation of the general N^{7}MLT topology. The current J considers all the possible combinations among the internal propagators. The blue line encodes a MLT with $L-5$ loops and $L-4$ propagators.

6.1 Universal topology

In this section we analyse the multiloop topologies that appear for the first time at five loops, i.e., the family composed by those loop topologies described by $L+5$, $L+6$ and $L+7$ propagators. We start identifying the representative diagrams, followed by a unified description and the application of the LTD framework to obtain the dual opening to connected trees.

Based on the classification scheme presented in Refs. [6, 118], the topological complexity of this set of diagrams corresponds to N^{7}MLT, which has $L+5$ common sets of propagators:

$$\{1,\ldots,L+1,12,123,1234,2345\}\ ,$$

and two additional specific sets distinguishing them from each other. To achieve a global representation of this family, we first need to unravel the representative topologies through the identification of the distinctive pair of sets.

Inspired by the N^{4}MLT *universal topology* [5], we recall the concept of a current to encode in a compact form the distinctive sets. This arrangement is diagrammatically represented in Fig. 6.1. Each specific topology is characterized by a pair of sets from the following list:

$$\{23,24,25,34,35,45,234,235,245,345\}\ .$$

J_1:	$\{234, 23\}$	$\{234, 24\}$ ⋆	$\{234, 34\}$
J_2:	$\{235, 23\}$ ⋆	$\{235, 25\}$ ⋆	$\{235, 35\}$ ⋆
J_3:	$\{245, 24\}$ ⋆	$\{245, 25\}$ ⋆	$\{245, 45\}$ ⋆
J_4:	$\{345, 34\}$	$\{345, 35\}$ ⋆	$\{345, 45\}$
J_5:	$\{23, 45\}$	$\{24, 35\}$ ⋆	$\{25, 34\}$ ⋆

Table 6.1: Pair of sets identifying the representative topologies of the N^{7}MLT family. The star indicates that the set is associated to a nonplanar diagram.

It is important to take into account that one of the internal sets, 2345, is imposed by momentum conservation. The total number of distinctive pairs is fifteen, and they are conveniently grouped in five channels as presented in Table 6.1 and displayed in Fig. 6.2. Many nonplanar topologies arise; in fact, they account for ten from the total of fifteen.

Each pair of sets from Table 6.1 is associated to a single Feynman diagram. The first L common sets of propagators depend on one characteristic loop momentum ℓ_s and the momenta of their propagators have the form

$$q_{i_s} = \ell_s + k_{i_s} \qquad s \in \{1, \dots, L\} \ . \tag{6.1}$$

The remaining five common sets are denoted as linear combinations of all the loop momenta, explicitly:

$$\begin{aligned} q_{i_{(L+1)}} &= -\sum_{s=1}^{L} \ell_s + k_{i_{(L+1)}} \ , \quad q_{i_{12}} = -\ell_1 - \ell_2 + k_{i_{12}} \ , \\ q_{i_{123}} &= -\sum_{s=1}^{3} \ell_s + k_{i_{123}} \ , \quad q_{i_{1234}} = -\sum_{s=1}^{4} \ell_s + k_{i_{1234}} \ , \\ q_{i_{2345}} &= -\sum_{s=2}^{5} \ell_s + k_{i_{2345}} \ , \end{aligned} \tag{6.2}$$

with $k_{i_s}, k_{i_{(L+1)}}, k_{i_{12}}, k_{i_{123}}, k_{i_{1234}}$ and $k_{i_{2345}}$ linear combinations of external momenta. The extra sets are the distinctive key to generate each of the fifteen topologies. We identify the momenta of their propagators as different

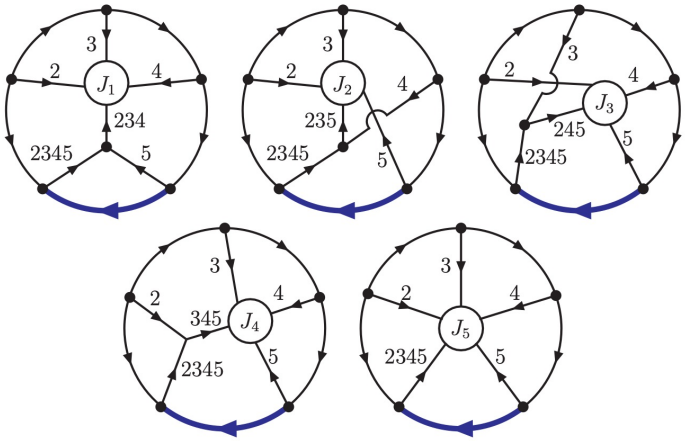

Figure 6.2: Diagrammatic representation of the multiloop topologies associated to the sets defined in Table 6.1 where only the internal propagators are labeled. The blue bold line represents an arbitrary number of propagators. In the case of the channel J_5, the characterized sets are established by merging two of the common sets as depicted in Fig.6.3.

linear combinations of ℓ_2, ℓ_3, ℓ_4 and ℓ_5, writing them as

$$\begin{aligned} q_{i_{rs}} &= -\ell_r - \ell_s + k_{i_{rs}} \ , \\ q_{i_{rst}} &= -\ell_r - \ell_s - \ell_t + k_{i_{rst}} \ , \qquad r,s \in \{2,3,4,5\} \, . \end{aligned} \tag{6.3}$$

In order to achieve a single expression to represent the N^{7}MLT topologies, we merge the sets presented in Table 6.1 into a current labeled as J,

$$J = \cup_{i=1}^{5} J_i \ . \tag{6.4}$$

The setting of this scenario allows us to assemble the Feynman representation of the N^{7}MLT family as

$$\mathcal{A}^{(L)}_{\mathrm{N^7MLT}} = \int_{\ell_1,\ldots,\ell_L} \mathcal{A}^{(L)}_{F}(1,\ldots,L+1,12,123,1234,2345,J) \ , \tag{6.5}$$

diagrammatic represented in accordance with Fig. 6.1.

The dual opening of Eq. (6.5) is computed by the direct application of the nested residues through the LTD framework. With the purpose of obtaining a manageable dual expression, we also propose an ansatz based on

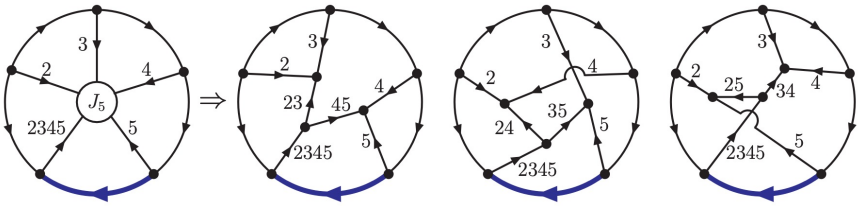

Figure 6.3: Diagrammatic representation of the multiloop topologies conforming the channel J_5.

a graphical interpretation of the opening. The comparison between these two ingredients allows us to achieve a LTD representation exhibited in a factorized form in terms of simpler subtopologies,

$$\begin{aligned}
&\mathcal{A}^{(L)}_{\mathrm{N^7MLT}}(1,\ldots,L+1,12,123,1234,2345,J) \qquad (6.6)\\
&= \mathcal{A}^{(5)}_{\mathrm{N^6MLT}}(1,\ldots,5,12,123,1234,2345,J) \otimes \mathcal{A}^{(L-5)}_{\mathrm{MLT}}(6,\ldots,L+1)\\
&+ \mathcal{A}^{(4)}_{\mathrm{N^5MLT}}(1\cup 2345,2,3,4,5\cup 1234,12,123,J) \otimes \mathcal{A}^{(L-4)}_{\mathrm{MLT}}(\overline{6},\ldots,\overline{L+1}) \ .
\end{aligned}$$

The term $\mathcal{A}^{(L)}_{\mathrm{N^{k-1}MLT}}$ refers to the integrand of the corresponding topology in the LTD representation; integration over the L loop momenta is assumed. The convolution symbol indicates that each component is open independently, while the on-shell conditions of all elements act together over the remaining off-shell propagators. Regarding the selected on-shell propagators, they are restricted so as not to generate disjoint trees due to the dual opening.

The LTD expression in Eq. (6.6) opens any multiloop $\mathrm{N^7MLT}$ topology to connected trees, furthermore, it is valid for all $\mathrm{N^{k-1}MLT}$ configurations with $k \leq 7$. The dual opening interpretation is depicted in Fig. 6.4, where the diagrams associated to the term $\mathcal{A}^{(5)}_{\mathrm{N^6MLT}}$ on the r.h.s. of Eq. (6.6) contemplate all possible configurations with five on-shell propagators in the sets $\{1,2,3,4,12,123,1234,2345,J\}$, and the contribution of $\mathcal{A}^{(4)}_{\mathrm{N^5MLT}}$ in the second term assumes four on-shell conditions selected from $\{1\cup 2345,2,3,4,5\cup 1234,12,123,J\}$. The term $\mathcal{A}^{(L-5)}_{\mathrm{MLT}}(6,\ldots,L+1)$ is opened according to the MLT opening introduced in Chapter 4; in $\mathcal{A}^{(L-4)}_{\mathrm{MLT}}(\overline{6},\ldots,\overline{L+1})$ all the momentum flows are reversed and all the sets contain one on-shell propagator.

The unfolding of Eq. (6.6) is computed recursively through the subtopologies arising. For instance, the five-loop contribution opens as follows

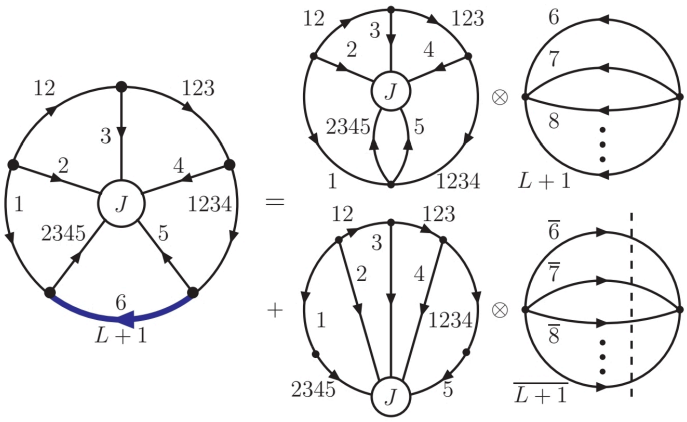

Figure 6.4: Diagrammatic representation for the factorized opening of the multiloop N^{7}MLT general topology. Only the on-shell cut of the last MLT-like subtopology with reversed momentum flow is shown.

$$\begin{aligned}
&\mathcal{A}^{(5)}_{\mathrm{N^6MLT}}(1,\ldots,5,12,123,1234,2345,J)\\
&=\mathcal{A}^{(5)}_{\mathrm{N^4MLT}}(1,\ldots,5,12,123,1234,2345)\\
&+\sum_{s\in J}\mathcal{A}^{(4)}_{\mathrm{N^4MLT}}(1,\ldots,5,12,123,1234,2345,\mathbf{s})\ .
\end{aligned}\tag{6.7}$$

The first term in the r.h.s. gives a LTD contribution with all the propagators with momenta in J remaining off shell. The second term on the r.h.s. of Eq. (6.7) considers all the contributions with a pair of propagators with momenta belonging to Table 6.1, therefore, these dual trees correspond to a single representative channel. The bold symbol, $\mathbf{s}$, is used to identify the contributions with on-shell propagators belonging to J.

Concerning the four-loop subtopology in Eq. (6.6), the dual opening is given by

$$\begin{aligned}
&\mathcal{A}^{(4)}_{\mathrm{N^5MLT}}(1\cup 2345,2,3,4,5\cup 1234,12,123,J)\\
&=\mathcal{A}^{(4)}_{\mathrm{N^3MLT}}(1\cup 2345,2,3,4,5\cup 1234,12,123)\\
&+\sum_{s\in J}\mathcal{A}^{(3)}_{\mathrm{N^3MLT}}(1\cup 2345,2,3,4,5\cup 1234,12,123,\mathbf{s})\ ,
\end{aligned}\tag{6.8}$$

where similar to Eq. (6.7), the first term in the r.h.s. considers all the pairs of propagators with momenta in J off shell, whereas the second term is associated to a specific three-loop N^{3}MLT topology.

Every representative topology in the N^{7}MLT family have common dual terms, those associated to the first term in the r.h.s. in Eqs. (6.7) and (6.8) respectively,

$$\begin{aligned}&\mathcal{A}^{(5)}_{\mathrm{N^4MLT}}(1,\dots,5,12,123,1234,2345) \quad \text{and}\\ &\mathcal{A}^{(4)}_{\mathrm{N^3MLT}}(1\cup 2345,2,3,4,5\cup 1234,12,123)\ .\end{aligned} \tag{6.9}$$

These contributions can be graphically represented with the first diagram in the r.h.s. of both sums depicted in Fig. 6.4 by replacing J with a five point interaction among the internal sets, i.e., by taking J as an empty set. To entirely unfold them and obtain the explicit dual terms, we continue to open the subtopologies recursively. Even if the ordering of opening any topology is arbitrary, following the guide of a diagrammatic interpretation allows us to work in a more manageable form.

Concerning the common dual terms in the N^{7}MLT topologies, the amplitude

$$\mathcal{A}^{(4)}_{\mathrm{N^3MLT}}(1\cup 2345,2,3,4,5\cup 1234,12,123) \tag{6.10}$$

opens according to Eq. (5.5) by considering the set 234 as empty and, in the case of the five-loop contribution, the explicit dual opening is given by

$$\begin{aligned}&\mathcal{A}^{(5)}_{\mathrm{N^4MLT}}(1,\dots,5,12,123,1234,2345)\\ &=\mathcal{A}^{(4)}_{\mathrm{N^4MLT}}(1,2,3,4,12,123,1234)\otimes\mathcal{A}^{(1)}_{\mathrm{MLT}}(5,2345)\\ &+\Big[\mathcal{A}^{(3)}_{\mathrm{NMLT}}(1,2,3,12,123)+\Big(\mathcal{A}^{(2)}_{\mathrm{MLT}}(1,2,12)+\mathcal{A}^{(2)}_{\mathrm{MLT}}(1,\overline{3})\Big)\\ &\otimes\mathcal{A}^{(1)}_{\mathrm{MLT}}(\overline{4})\Big]\otimes\mathcal{A}^{(2)}_{\mathrm{MLT}}(\overline{5},\overline{2345})+\Big[\mathcal{A}^{(2)}_{\mathrm{MLT}}(\overline{1234},2\cup\overline{12})\otimes\mathcal{A}^{(1)}_{\mathrm{MLT}}(3,123)\\ &+\mathcal{A}^{(3)}_{\mathrm{MLT}}(\overline{1234},\overline{3},\overline{123})+\mathcal{A}^{(2)}_{\mathrm{MLT}}(\overline{1234},2\cup\overline{312})\otimes\mathcal{A}^{(1)}_{\mathrm{MLT}}(\overline{4})\\ &+\Big(\mathcal{A}^{(2)}_{\mathrm{MLT}}(3,\overline{12})+\mathcal{A}^{(2)}_{\mathrm{MLT}}(\overline{1234},2\cup\overline{3}\cup\overline{12})\Big)\otimes\mathcal{A}^{(1)}_{\mathrm{MLT}}(4)\Big]\otimes\mathcal{A}^{(2)}_{\mathrm{MLT}}(5,2345)\ .\end{aligned} \tag{6.11}$$

The number of dual terms arising from the contributions in Eqs. (6.10) and (6.11) for an arbitrary number of loops is given by $11(6L-19)$.

The contributions corresponding to the second term in the r.h.s. in Eqs. (6.7) and (6.8) depend on the particular topology to be opened. In the following section we take a specific example and present the explicit contributions characterising the topology.

6.2 Specific channels

In this section we present the development of the topology associated to the pair of sets $\{234, 23\}$ belonging to the current J_1. The factorized dual opening is obtained through the application of Eq. (6.6) replacing J by $\{234, 23\}$. The diagrammatic representation of the associated topology and its factorized dual opening is depicted in Fig. 6.5.

The common terms in the fifteen topologies are the ones associated to Eqs. (6.10) and (6.11) which are illustrated with the first diagram in the r.h.s. of each sum in Fig. 6.6. From the previous section we know that the contributions for this specific topology arise from the second term in the r.h.s. of Eqs. (6.7) and (6.8) which are diagrammatically represented by the sum of the second and third diagrams in the r.h.s. of each sum in Fig. 6.6.

The unfolding of the second term in the r.h.s. of Eq. (6.7) with $s \in \{234, 23\}$ is given by

$$
\begin{aligned}
&\mathcal{A}^{(4)}_{\mathrm{N^4MLT}}(1,\ldots,5,12,123,1234,2345,23,234) \\
&+\mathcal{A}^{(4)}_{\mathrm{N^4MLT}}(1,\ldots,5,12,123,1234,2345,23) \\
&=\Big[\Big(\mathcal{A}^{(3)}_{\mathrm{N^2MLT}}(1,2,3,12,123,23)+\mathcal{A}^{(2)}_{\mathrm{MLT}}(1,2,12)\otimes\mathcal{A}^{(1)}_{\mathrm{MLT}}(\overline{4}) \\
&+\mathcal{A}^{(3)}_{\mathrm{MLT}}(1,\overline{3},\overline{4})\Big)\otimes\mathcal{A}^{(1)}_{D}(\overline{234})+\Big(\mathcal{A}^{(2)}_{\mathrm{MLT}}(\overline{1234},2\cup\overline{12}) \\
&\otimes\mathcal{A}^{(1)}_{\mathrm{MLT}}(3,4\cup 23)+\mathcal{A}^{(3)}_{\mathrm{MLT}}(\overline{1234},\overline{3},\overline{4}\cup\overline{23})+\mathcal{A}^{(3)}_{\mathrm{MLT}}(12,3,4) \\
&+\mathcal{A}^{(3)}_{\mathrm{MLT}}(4\cup\overline{1234},2\cup\overline{3}\cup\overline{12},\overline{123})\Big)\otimes\mathcal{A}^{(1)}_{D}(234)\Big]\otimes\mathcal{A}^{(1)}_{\mathrm{MLT}}(5,2345) \\
&+\Big[\Big(\mathcal{A}^{(2)}_{\mathrm{MLT}}(1,2,12)+\mathcal{A}^{(2)}_{\mathrm{MLT}}(1,\overline{3})\Big)\otimes\Big(\mathcal{A}^{(2)}_{\mathrm{MLT}}(4,5,2345) \\
&+\mathcal{A}^{(1)}_{\mathrm{MLT}}(5,2345)\otimes\mathcal{A}^{(1)}_{\mathrm{MLT}}(\overline{1234})\Big)+\mathcal{A}^{(1)}_{\mathrm{MLT}}(2\cup\overline{3},12) \\
&\otimes\mathcal{A}^{(2)}_{\mathrm{MLT}}(5,2345)\otimes\mathcal{A}^{(1)}_{\mathrm{MLT}}(\overline{1234})\Big]\otimes\mathcal{A}^{(1)}_{D}(\overline{23}) \\
&+\Big[\Big(\mathcal{A}^{(2)}_{\mathrm{MLT}}(\overline{123},\overline{3},12)+\mathcal{A}^{(2)}_{\mathrm{MLT}}(\overline{123},2)\Big)\otimes\mathcal{A}^{(2)}_{\mathrm{MLT}}(4,5,2345) \\
&+\Big(\mathcal{A}^{(2)}_{\mathrm{MLT}}(\overline{4}\cup\overline{123},\overline{3},12)+\mathcal{A}^{(2)}_{\mathrm{MLT}}(\overline{4}\cup\overline{123},2)\Big)\otimes\mathcal{A}^{(1)}_{\mathrm{MLT}}(5,2345) \\
&\otimes\mathcal{A}^{(1)}_{\mathrm{MLT}}(\overline{1234})\Big]\otimes\mathcal{A}^{(1)}_{D}(23)\ ,
\end{aligned}
\tag{6.12}
$$

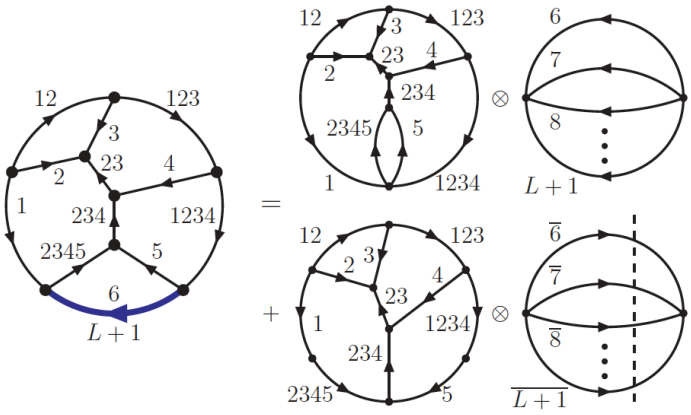

Figure 6.5: Diagrammatic representation for the topology having as characterized set $\{234, 23\}$ and its factorized dual opening.

and the one corresponding to Eq. (6.8),

$$
\begin{aligned}
&\mathcal{A}^{(3)}_{\mathrm{N^3MLT}}(1 \cup 2345, 2, 3, 4, 5 \cup 1234, 12, 123, 23, 234) \qquad (6.13)\\
&+ \mathcal{A}^{(3)}_{\mathrm{N^3MLT}}(1 \cup 2345, 2, 3, 4, 5 \cup 1234, 12, 123, 23)\\
&= \Big[\mathcal{A}^{(3)}_{\mathrm{N^2MLT}}(1 \cup 2345, 2, 3, 12, 123, 23) + \mathcal{A}^{(2)}_{\mathrm{MLT}}(1 \cup 2345, 2, 12) \otimes \mathcal{A}^{(1)}_{\mathrm{MLT}}(\overline{4})\\
&+ \mathcal{A}^{(3)}_{\mathrm{MLT}}(1 \cup 2345, \overline{3}, \overline{4})\Big] \otimes \mathcal{A}^{(1)}_{D}(\overline{234})\\
&+ \Big[\mathcal{A}^{(2)}_{\mathrm{MLT}}(\overline{5} \cup \overline{1234}, 2 \cup \overline{12}) \otimes \mathcal{A}^{(1)}_{\mathrm{MLT}}(3, 4 \cup 23) + \mathcal{A}^{(3)}_{\mathrm{MLT}}(\overline{5} \cup \overline{1234}, \overline{3}, \overline{4} \cup \overline{23})\\
&+ \mathcal{A}^{(3)}_{\mathrm{MLT}}(\overline{12}, 3, 4) + \mathcal{A}^{(3)}_{\mathrm{MLT}}(\overline{5} \cup \overline{1234} \cup \overline{4}, 2 \cup \overline{3} \cup \overline{12}, \overline{123})\Big] \otimes \mathcal{A}^{(1)}_{D}(234)\\
&+ \Big(\mathcal{A}^{(2)}_{\mathrm{MLT}}(1 \cup 2345, 2, 12) + \mathcal{A}^{(2)}_{\mathrm{MLT}}(1 \cup 2345, \overline{3})\Big) \otimes \mathcal{A}^{(1)}_{\mathrm{MLT}}(4, 5 \cup 1234)\\
&\otimes \mathcal{A}^{(1)}_{D}(\overline{23}) + \Big[\Big(\mathcal{A}^{(2)}_{\mathrm{MLT}}(\overline{123}, \overline{3}, 12) + \mathcal{A}^{(2)}_{\mathrm{MLT}}(\overline{123}, 2)\Big) \otimes \mathcal{A}^{(1)}_{\mathrm{MLT}}(4, 5 \cup 1234)\\
&+ \mathcal{A}^{(1)}_{\mathrm{MLT}}(2 \cup \overline{3}, 12) \otimes \mathcal{A}^{(2)}_{\mathrm{MLT}}(\overline{4}, \overline{5} \cup \overline{1234})\Big] \otimes \mathcal{A}^{(1)}_{D}(23)\ .
\end{aligned}
$$

The sets in blue in the arguments of the terms in the l.h.s. of Eqs. (6.12) and (6.13) indicate the set that we use as a starting cut in the second and third diagram of each sum in Fig. 6.6. After this action we end up with known subtopologies that we recursively compute by applying the results from Refs. [5,6]. The total number of dual terms emerging from Eqs. (6.12) and (6.13) for an arbitrary number of loops is given by $119L - 380$. The number of dual terms arising from every specific channel for an arbitrary number of loops is summarized in Table 6.2.

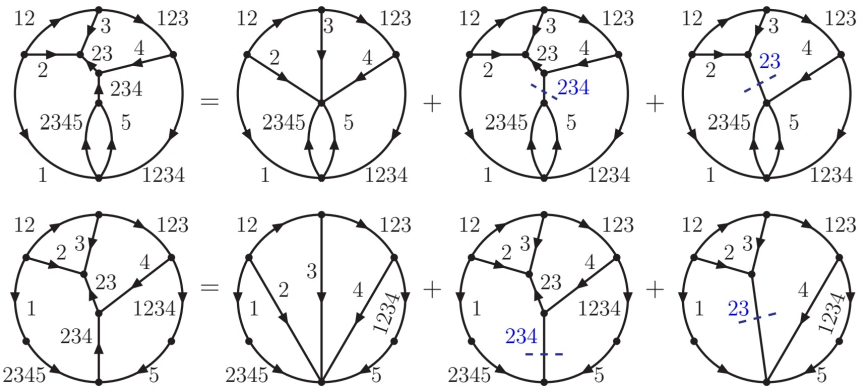

Figure 6.6: Diagrammatic representation of the sum of contributions associated to the five-loop N^{6}MLT (top) and the four-loop N^{4}MLT (bottom) dual opening.

It is worth mentioning that among the fifteen configurations some of them are topologically equivalent. For example, the dual representation of the diagram characterized by $\{234, 34\}$ can be obtained from the dual representation computed to the topology characterized with $\{234, 23\}$, by the substitution $23 \to 34$ and the exchange $2 \leftrightarrow 4$,

$$\mathcal{A}^{(L)}_{\mathrm{N^7MLT}}(1,\ldots,234,23) \xrightarrow[2\leftrightarrow 4]{23\to 34} \mathcal{A}^{(L)}_{\mathrm{N^7MLT}}(1,\ldots,234,34)\ .$$

For the remaining equivalent topologies, we require to exchange $2 \leftrightarrow 4$ and $5 \leftrightarrow 2345$, as well as applying the proper substitution between the distinctive sets. Explicitly, we have that

$$\begin{aligned}
&\mathcal{A}^{(L)}_{\mathrm{N^7MLT}}(1,\ldots,235,23) \xrightarrow[2\leftrightarrow 4,\ 5\leftrightarrow 2345]{235\to 25,\ 23\to 34} \mathcal{A}^{(L)}_{\mathrm{N^7MLT}}(1,\ldots,25,34)\ ,\\
&\mathcal{A}^{(L)}_{\mathrm{N^7MLT}}(1,\ldots,235,35) \xrightarrow[2\leftrightarrow 4,\ 5\leftrightarrow 2345]{235\to 25,\ 35\to 245} \mathcal{A}^{(L)}_{\mathrm{N^7MLT}}(1,\ldots,245,25)\ ,\\
&\mathcal{A}^{(L)}_{\mathrm{N^7MLT}}(1,\ldots,245,24) \xrightarrow[2\leftrightarrow 4,\ 5\leftrightarrow 2345]{245\to 35} \mathcal{A}^{(L)}_{\mathrm{N^7MLT}}(1,\ldots,24,35)\ ,\\
&\mathcal{A}^{(L)}_{\mathrm{N^7MLT}}(1,\ldots,245,45) \xrightarrow[2\leftrightarrow 4,\ 5\leftrightarrow 2345]{245\to 35,\ 45\to 345} \mathcal{A}^{(L)}_{\mathrm{N^7MLT}}(1,\ldots,345,35)\ ,\\
&\mathcal{A}^{(L)}_{\mathrm{N^7MLT}}(1,\ldots,345,34) \xrightarrow[2\leftrightarrow 4,\ 5\leftrightarrow 2345]{345\to 45,\ 34\to 23} \mathcal{A}^{(L)}_{\mathrm{N^7MLT}}(1,\ldots,23,45)\ .
\end{aligned}$$

Certainly, there are topologies that cannot be obtained from a direct replacement of indices, mainly those related with nonplanar topologies. Nev-

J_1:	$\{234, 23\}$	$\star$ $\{234, 24\}$	$\{23, 34\}$
	$119L - 380$	$132L - 418$	$119L - 380$
J_2:	$\star$ $\{235, 23\}$	$\star$ $\{235, 25\}$	$\star$ $\{235, 35\}$
	$143L - 473$	$158L - 519$	$165L - 54$
J_3:	$\star$ $\{245, 24\}$	$\star$ $\{245, 25\}$	$\star$ $\{245, 45\}$
	$165L - 554$	$165L - 554$	$165L - 83$
J_4:	$\{345, 34\}$	$\star$ $\{345, 35\}$	$\{34, 45\}$
	$143L - 500$	$165L - 583$	$158\ L - 575$
J_5:	$\{23, 45\}$	$\star$ $\{24, 35\}$	$\star$ $\{25, 34\}$
	$143L - 500$	$165L - 554$	$143L - 473$

Table 6.2: Numbers of dual terms for the individual channels.

ertheless, the direct application of the LTD shows that there are no disjoint trees in the forest of the N^{7}MLT topology and this feature is important to compute physical observables at high precision. Therefore, we leave the application of these expressions to further analysis.

6.3 General causal representation

We know that for any loop integral or scattering amplitude, the emergence of a causal expression occurs after all the nested residues are summed up. However, we must be aware that the numerator of the integrand may be a lengthy polynomial in the on-shell and external energies.

The strategy introduced in Ref. [113] and followed in Chapter 5, to derive a more suitable causal representation, was to reinterpret the causal expression found in terms of entangled thresholds, ending up with the following general causal LTD representation

$$\mathcal{A}_D^{(L)} = \int_{\vec{\ell}_1 \dots \vec{\ell}_L} \frac{1}{x_n} \sum_{\sigma \in \Sigma} \frac{\mathcal{N}_{\sigma(i_1,\dots,i_{n-L})}}{\lambda_{\sigma(i_1)}^{h_{\sigma(i_1)}} \cdots \lambda_{\sigma(i_{n-L})}^{h_{\sigma(i_{n+L})}}} + (\lambda_p^+ \leftrightarrow \lambda_p^-) \ , \tag{6.14}$$

with $x_n = \prod_{i=1}^n 2q_{i,0}^{(+)}$. The Feynman propagators from Eq. (4.2) are substituted in Eq. (6.14) by causal propagators $1/\lambda_p^\pm$ with

$$\lambda_p^\pm = \sum_{i \in p} q_{i,0}^{(+)} \pm k_{p,0} \ , \tag{6.15}$$

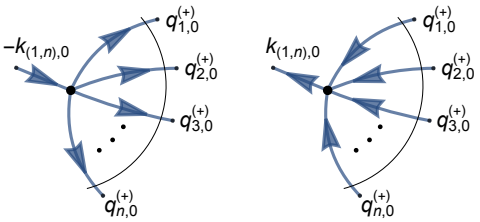

Figure 6.7: Graphical interpretation of the causal configurations encoded by $\lambda^{+}_{(1,n)}$ (left) and $\lambda^{-}_{(1,n)}$ (right). If the total external momentum is outgoing, $k_{(1,n),0} > 0$, a threshold singularity arises when all the internal momenta are set on shell and their three-momenta flow towards the interaction vertex. The opposite configuration, $\lambda^{+}_{(1,n)}$, generates a threshold singularity if $k_{(1,n),0} < 0$.

where p is a partition of the on-shell energies, and $k_{p,0}$ is a linear combination of the energy components of the external momenta. Causal propagators may appear raised to a power if the Feynman propagators in the original representation are raised to a power, for example due to self-energy insertions. Each $\lambda^{\pm}_{p}$ is associated to a kinematic configuration in which the momentum flows of all the propagators that belong to the partition p are aligned in the same direction. A graphical interpretation is provided in Fig. 9.5. Any other configuration cannot be interpreted as causal and is absent from Eq. (6.14). Depending on the sign of $k_{p,0}$, either λ^{+}_{p} or λ^{-}_{p} becomes singular when all the propagators in p are set on shell.

The set Σ in Eq. (6.14) contains all the combinations of causal propagators that are entangled, i.e., whose momentum flows are compatible with each other and therefore represent causal thresholds that can occur simultaneously. Each element in Σ fixes the momentum flows of all sets in specific directions. Conversely, once the momentum flows of all sets are fixed, the causal representation in Eq. (6.14) can be bootstrapped.

To obtain the causal LTD representation with the structure exhibited in Eq. (6.14), is essential to overcome an important difficulty: the determination of the causal thresholds of multiloop Feynman integrals from the identification of all internal configurations that fulfill causal conditions. Aiming for a more efficient algorithm, in the following chapter we explore a promising method based on quantum computing for the search of causal singular configurations of multiloop Feynman diagrams.

Chapter 7

Quantum algorithms for Feynman loop integrals

Quantum algorithms [119] are a very promising avenue for solving specific problems that become too complex or even intractable for classical computers because they scale either exponentially or superpolynomially. They are particularly well suited to solve those problems for which the quantum principles of superposition and entanglement can be exploited to gain a speed-up advantage over the counterpart classical algorithms. These are, for example, the well-known cases of database querying [120] and factoring integers into primes [121]. Other recent applications are related to the enhanced capabilities of quantum systems for minimizing Hamiltonians [122, 123] which lead to a wide range of applications in optimization problems. For instance, this framework has been used in quantum chemistry [124], nuclear physics [125, 126], and also finance, where portfolio optimization [127] is the flagship application.

In the context of particle physics, quantum algorithms have recently started to come under the spotlight. Some applications include: the speed-up of jet clustering algorithms [128–131], jet quenching and jet broadening in medium [132, 133], determination of parton densities [134], simulation of parton showers [135–137], heavy-ion collisions [137], quantum machine learning [138–140] and lattice gauge theories [141–146].

Despite recent proposals on numerical evaluation of tree-level helicity amplitudes [147] and cross-sections [148], it is generally accepted that the per-

turbative description of hard scattering processes at high energies is beyond the reach of quantum computers, since it would require a prohibitive number of qubits. In this chapter, we present a proof-of-concept of a quantum algorithm applied to perturbative quantum field theory and demonstrate that the unfolding of certain properties of Feynman loop integrals is completely appropriate and amenable in a quantum computing approach.

The feasibility of associating quantum computing and Feynman loop integrals is due to the fact that the two on-shell states of a Feynman propagator can be stored in a qubit. Specifically, the problem we address is the bootstrapping of the causal representation of multiloop Feynman integrals in the Loop-Tree Duality formalism from the identification of all internal configurations that fulfill causality requirements among the $N = 2^n$ potential solutions, where n is the number of internal Feynman propagators. As we will show, this is a satisfiability problem that can be solved with the application a well-designed modification of Grover's algorithm [120].

The archetypal situation in which this algorithm is employed consists in finding a single and unique solution among a large unstructured set of N configurations. While a classical algorithm requires testing the satisfiability condition for all cases, i.e. $\mathcal{O}(N)$ iterations, the quantum algorithm considers all the states in a uniform superposition and tests the satisfiability condition at once. Ultimately, the complexity of the task goes from $\mathcal{O}(N)$ in the classical case to $\mathcal{O}(\sqrt{N})$ in the quantum case. This constitutes a big motivation to explore the applicability of such algorithms in the calculation of Feynman diagrams and integrals.

From a purely mathematical perspective causal solutions correspond, in graph theory language, to directed acyclic graphs [149], which have a broad scope of applications in other sciences, including the characterization of quantum networks [150]. In classical computations, there exist efficient algorithms that identify closed directed loops in connected graphs based on searches on tree representations, such as the well known depth-first search method [151]. We apply a different strategy, exploiting the structure of graphs that are relevant in higher-order perturbative calculations, with the purpose of easing the identification of causal solutions.

This chapter [3] starts describing how to characterize causal configurations by using geometrical arguments. In particular, we emphasise the impor-

tance of identifying all the configurations with a consistent causal flow of internal momenta, which are equivalent to directed acyclic graphs. We proceed with the development of a suitable modification of the original Grover's algorithm for querying of multiple solutions [152] to identify all the states of a multiloop Feynman diagram that satisfy causality. It is worth noting that since its introduction in 1996, Grover's algorithm has been generalized [153, 154] and adapted for other applications, such as solving the collision problem [155] or performing partial quantum searches [156].

7.1 Geometric interpretation of causal flows

Originated from the perturbative expansion of the path integral, multiloop multileg scattering amplitudes are described by Feynman diagrams made of vertices and propagators connecting them. Whilst vertices codify interactions among particles, propagators are associated to virtual states moving before or after the interactions take place. These Feynman diagrams might contain closed paths or loops, which symbolise quantum fluctuations involving the emission and subsequent absorption of a virtual particle. The number of loops corresponds to the number of free integration variables in Eq. (4.2).

Concerning the dual causal representation presented in Chapters 4 and 5, it can be described by relying on *reduced* Feynman graphs built from vertices and edges [157, 158]. Considering a number of propagators (lines) connecting a pair of interaction vertices, the only possible causal configurations are those in which the momentum flow of all the propagators are aligned in the same direction. As a result, and with the purpose of bootstrapping the causal configurations, a multiloop bunch of propagators can be replaced by a single *edge* representing the common momentum flow [157, 158] as shown in Fig. 7.1. This replacement is further supported by the explicit demonstrations reported in Ref. [118].

Once propagators have been collapsed into edges, we can count the number of actual loops in the reduced Feynman graph: these are the so-called *eloops*. We would like to emphasize that the number of eloops is always smaller (or equal) to the number of loops. Whilst the latter counts the number of primitive integration variables, the former refers to a purely topological property of the reduced Feynman graph.

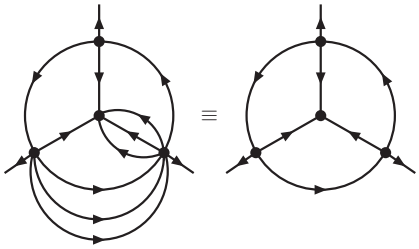

Figure 7.1: Causal equivalence of a multiloop Feynman diagram (left) with a reduced Feynman graph made of edges obtained by merging all propagators connecting a pair of vertices (right).

Following the geometrical description of Feynman diagrams, it is possible to introduce a topological classification related to the number of vertices, V. In concrete, we define the *order* of a reduced diagram as $k = V - 1$, which corresponds to the number of off-shell lines involved in the dual representation. In fact, it can be shown that $k = n - L$, and thus the order of the diagram coincides with the number of causal propagators that are being multiplied in each term of the causal representation in Eq. (6.14).

At this point, let us comment on the reconstruction of the causal structure and some of the available computational strategies for that purpose. Causal propagators, $1/\lambda_p^{\pm}$, are identified efficiently starting from the connected binary partitions of vertices of the reduced Feynman graph. Once the causal propagators are known, the representation in Eq. (6.14) can be recovered by identifying all the possible causal compatible combinations of k causal propagators: these are the "*causal entangled thresholds*". There are three conditions that determine the eligibility entanglements [158]:

i) The combination of k causal propagators depends on the on-shell energies of all the edges.

ii) The two sets of vertices associated to two causal propagators are disjoint, or one of them is totally included in the other. For instance, if a maximally connected graph (i.e. a graph where all the vertices are connected to each other) is composed by the vertices $V = \{1, 2, 3, 4, 5\}$, then $\lambda_1 = \{2, 3, 4\}$ and $\lambda_2 = \{1, 3, 4\}$ cannot be simultaneously entangled since their intersection is not empty. But, λ_1 and $\lambda_3 = \{2, 3\}$ are part of an entangled causal threshold because $\{2, 3\} \subset \{2, 3, 4\}$.

iii) *Causal flow*: The momentum of the edges that cross a given binary partition of vertices (i.e. each λ_i being entangled) must be consistently aligned. Momentum must flow from one partition to a different one.

The strategy to successfully identify the set Σ in Eq. (6.14) consists in following the conditions 1 to 3, in that specific order, as already implemented in Refs. [158, 159]. Remarkably, the third condition can be reinterpreted as selecting the directed graphs associated to the reduced Feynman diagram. Since momenta must exit one partition and enter into a different one, there cannot be closed cycles. This means that condition 3 is equivalent to identifying all possible *directed acyclic graphs* compatible with a given set of causal propagators $\{\lambda_{i_1}, \ldots, \lambda_{i_k}\}$. In this way, another reformulation exists for the causal reconstruction:

i) *Causal flow*: Identify all the possible directed acyclic graphs obtained from the original reduced Feynman graph.

ii) Dress each causal configuration with all the possible combinations of entangled causal propagators fulfilling the first and second condition of the previous listing.

Both approaches turn out to be equivalent, supporting the path selected for the detection of causal configurations from the corresponding directed acyclic graphs. However, the identification of directed acyclic graphs is known to be very time-demanding in classical computations [151], motivating the search of alternative techniques that could provide any possible speed-up. In the following section we will explain how to use quantum algorithms for such a purpose. This can be considered as a first step towards a fully quantum approach to the identification of entangled causal thresholds.

The development of the quantum algorithm takes into consideration the collection of the representative multiloop topologies presented in Chapters 4 and 5 in terms of edges, which are depicted in Fig. 7.2. We follow the classification scheme introduced in Refs. [5, 113], where loop diagrams are ranked according to the number of sets of propagators that depend on different linear combinations of the loop momenta, starting from the maximal loop topology (MLT) with $L + 1$ sets, to N^{k}MLT with $L + 1 + k$ sets. An extended classification has been introduced in Ref. [157] that considers all the vertices connected to each other.

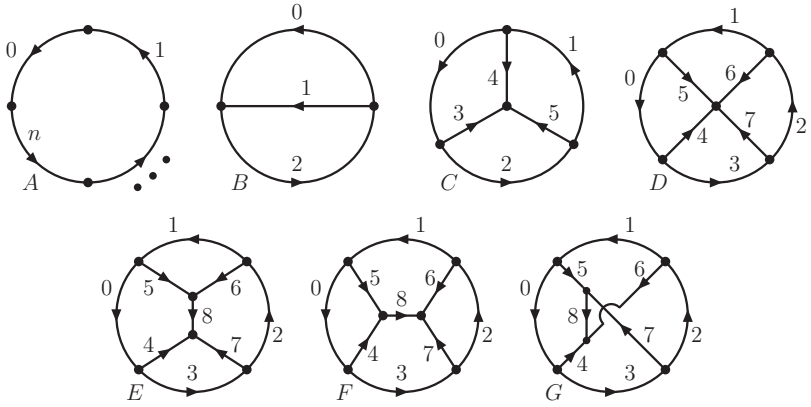

Figure 7.2: Representative multiloop topologies with up to four eloops. The direction of the arrows corresponds to the $|1\rangle$ states. The vertices may or may not have attached external momenta. Beyond one eloop, each line can be composed of n_i edges that introduce additional vertices. From left to right and top to bottom: one eloop with n vertices, two eloops (MLT), three eloops (N^{2}MLT), four eloops with one four-particle vertex (N^{3}MLT), and four eloops with trivalent interactions (N^{4}MLT), t-, s- and u-channels.

7.2 Grover's quantum algorithm

The standard Grover's querying algorithm [120] over unstructured databases relies on three fundamental concepts: uniform superposition of all possible states, an oracle operator to tag the states of interest, and a diffusion operator to amplify the probability of these elements.

The schematic representation of the three main ingredients of Grover's quantum algorithm is shown in Fig. 7.3 and the detailed description is shown below:

i) The uniform superposition of the total of $N = 2^n$ states is denoted as

$$|q\rangle = \frac{1}{\sqrt{N}} \sum_{x=0}^{N-1} |x\rangle \ , \tag{7.1}$$

where n is the number of edges. The Eq. (7.1) can also be seen and written as the superposition of a winning state $|w\rangle$, encoding all the causal solutions in a uniform superposition, and the orthogonal state

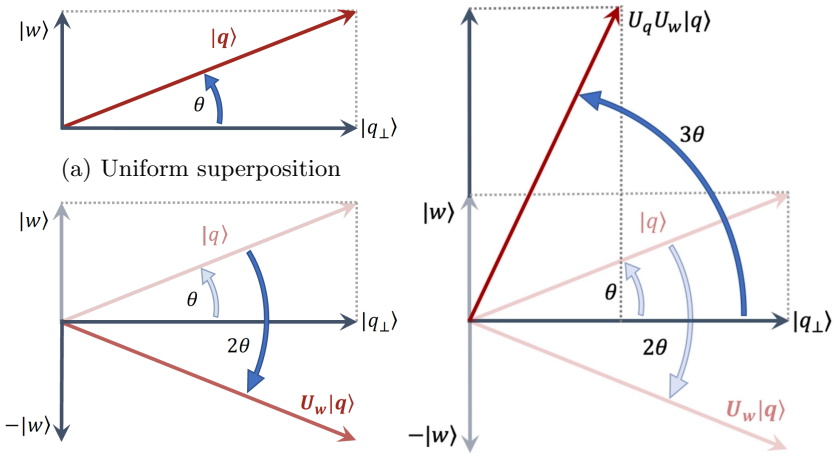

(a) Uniform superposition

(b) Oracle operator

(c) Diffusion operator

Figure 7.3: Diagrammatic representation of the three main ingredients of the standard Grover's quantum algorithm. (a) Uniform superposition, (b) Oracle operator and (c) Diffusion operator.

$|q_\perp\rangle$, that collects the noncausal states

$$|q\rangle = \cos\theta\,|q_\perp\rangle + \sin\theta\,|w\rangle \ . \tag{7.2}$$

The mixing angle is given by

$$\theta = \arcsin\sqrt{r/N} \ , \tag{7.3}$$

with r the number of causal solutions, and N the total number of possible configurations, which measures the ratio of states to be queried. The winning and orthogonal uniform superpositions are given by

$$|w\rangle = \frac{1}{\sqrt{r}}\sum_{x\in w}|x\rangle \ , \qquad |q_\perp\rangle = \frac{1}{\sqrt{N-r}}\sum_{x\notin w}|x\rangle \ . \tag{7.4}$$

ii) The oracle operator denoted as

$$U_w = \boldsymbol{I} - 2|w\rangle\langle w| \ , \tag{7.5}$$

flips the state $|x\rangle$ if $x \in w$, $U_w|x\rangle = -|x\rangle$, and leaves it unchanged otherwise, $U_w|x\rangle = |x\rangle$ if $x \notin w$.

iii) The diffusion operator expressed as

$$U_q = 2|q\rangle\langle q| - \boldsymbol{I} \ , \tag{7.6}$$

performs a reflection around the initial state $|q\rangle$, in order to amplify the probability of the causal singular configurations.

According to the particular problem, the application of the oracle and diffusion operators may have to be performed repeatedly. The iterative application of both operators t times leads to

$$(U_q U_w)^t |q\rangle = \cos\theta_t \, |q_\perp\rangle + \sin\theta_t \, |w\rangle \ , \tag{7.7}$$

where $\theta_t = (2t+1)\,\theta$.

The mixing angle plays a critical role to define a proper number of iterations, θ_t has to be chosen according to the following condition:

$$\frac{\cos^2\theta_t}{N-r} \ll \frac{\sin^2\theta_t}{r} \ . \tag{7.8}$$

The general purpose is to obtain a final state such that the probability of each of the components in the orthogonal state is much smaller than the probability of each of the causal solutions. This goal is achieved when $\sin^2\theta_t \sim 1$.

Based on the relation stated in Eq. (7.8), Grover's standard algorithm shows the desirable performance if θ is less or similar to $\pi/6$, equivalent to have r less or similar to $N/4$. In the case of much larger angles, the amplitude probability amplification of the winning states is inadequate. For example:

- If $\theta = \pi/3$ the first iteration leads to $\theta_1 = \pi$ which in fact suppresses the projection onto the set of solutions.
- For $\theta = \pi/4$ or $r = N/2$ no matter how many iterations are enforced the probabilities of the initial states remain unchanged.

Considering our specific problem, we know from the classical computation [5, 113] that the number of causal states associated to the multiloop topologies shown in Fig. 7.2 are greater than $N/4$. To overcome this condition, in the following section, we present two potential adjustments and the description of the proposed algorithm.

Before moving forward we recall the concept of the quantum depth[1] of a quantum circuit used to encode a quantum algorithm, which gives the number of gates that need to be executed along the longest path of the circuit from input to output, moving forward in time along qubit wires. It represents an estimate of the efficiency of a quantum circuit. The input is understood as the preparation of the qubits and the output as the measurement gate. In the implementation to be presented in Section 7.4, the quantum circuit depth is computed through `QuantumCircuit.depth()`[2], a routine provided by Qiskit. An important feature of the quantum circuit depth is the impact of quantum gates acting in no common qubits, allowing to perform them at the same time-step. On the other hand, if the gates act in at least one common qubit they have to be applied in different time-steps, increasing the quantum circuit depth.

7.3 Quantum algorithm for causal querying

The proposed modification of Grover's quantum algorithm incorporates a pair of strategies to achieve the best feasibility of the algorithm. One of the optional strategies, which is also valid for other problems where the number of solutions is larger than $N/4$, is to enlarge the total number of states without increasing the number of solutions by introducing ancillary qubits in the register that encode the edges of the loop diagram[3]. In general, the maximum number of ancillary qubits needed is two, as this increases the number of total states by a factor of 4.

In particular, for Feynman loop diagrams we have a remarkable advantage; the fact that given a causal solution (directed acyclic configuration), the mirror state in which all internal momentum flows are reversed is also a causal solution. Therefore, the most efficient strategy is to single out one of the edges and consider that only one of its states contributes to the winning set. The mirror states are directly deduced from the selected causal solutions. As a result, the complete set of causal solutions can be determined with the help of at most one ancillary qubit.

The modified Grover's quantum algorithm requires three registers for implementation, together with an extra qubit used as marker by the Grover's

[1] https://quantumcomputing.stackexchange.com
[2] https://qiskit-test.readthedocs.io
[3] This strategy has been previously discussed in Ref. [160].

oracle. The first register, whose qubits are labelled q_i, encode the states of the edges. The qubit q_i is in the state $|1\rangle$ if the momentum flow of the corresponding edge is oriented in the direction of the initial assignment and in $|0\rangle$ if it is in the opposite direction (see Fig. 7.2). In any case, the final physical result is independent of the initial assignment, being used only as a reference.

The second register, named c_{ij}, stores the Boolean clauses that probe whether or not two qubits representing two adjacent edges are in the same state (whether or not their momenta are oriented in the same direction). These binary clauses are defined as

$$\begin{aligned} c_{ij} &\equiv (q_i = q_j) \ , \\ \bar{c}_{ij} &\equiv (q_i \neq q_j) \ , \qquad i,j \in \{0,\ldots,n-1\} \ . \end{aligned} \tag{7.9}$$

The third register, $a_k(\{c_{ij}\},\{\bar{c}_{ij}\})$, encodes the eloop clauses that probe if all the qubits (edges) in each of the eloops that are part of the diagram generate a cyclic circuit.

The causal quantum algorithm is implemented as follows. The initial uniform superposition is obtained by applying Hadamard gates to each of the qubits in the q-register, $|q\rangle = H^{\otimes n}|0\rangle$, while the qubit which is used as Grover's marker is initialized to

$$|out_0\rangle = \frac{|0\rangle - |1\rangle}{\sqrt{2}} \equiv |-\rangle \, , \tag{7.10}$$

corresponding to a Bell state in the basis $\{|0\rangle,|1\rangle\}$. The other registers, $|c\rangle$ and $|a\rangle$, used to store the binary and eloop clauses are initialized to $|0\rangle$. Each binary clause $\bar{c}_{ij}$ requires two CNOT gates operating between two qubits in the $|q\rangle$ register and one qubit in the $|c\rangle$ register. An extra XNOT gate acting on the corresponding qubit in $|c\rangle$ is needed to implement a c_{ij} binary clause.

The oracle is defined as

$$U_w|q\rangle|c\rangle|a\rangle|out_0\rangle = (-1)^{f(a,q)}\,|q\rangle|c\rangle|a\rangle|out_0\rangle \ , \tag{7.11}$$

therefore, if all the causal conditions are satisfied, $f(a,q) = 1$, the corresponding states are marked; otherwise, if $f(a,q) = 0$, they are left unchanged. After the marking, the $|c\rangle$ and $|a\rangle$ registers are rotated back to $|0\rangle$

eloops (edges per set)	$\|q\rangle$	$\|c\rangle$	$\|a\rangle$	Total
one (n)	$n+1$	$n-1$	1	$2n+2$
two (n_0, n_1, n_2)	n	n	3	$2n+4$
three $(n_0, \ldots, n_5)$	n	$n+(2 \text{ to } 3)$	4 to 7	$2n+(7 \text{ to } 11)$
four$^{(\mathrm{N^3MLT})}$ $(n_0, \ldots, n_7)$	n	$n+(3 \text{ to } 6)$	5 to 13	$2n+(9 \text{ to } 20)$
four$^{(t,s)}$ $(n_0, \ldots, n_8)$	n	$n+(4 \text{ to } 7)$	5 to 13	$2n+(10 \text{ to } 21)$
four$^{(u)}$ $(n_0, \ldots, n_8)$	n	$n+(5 \text{ to } 8)$	9 to 13	$2n+(15 \text{ to } 22)$

Table 7.1: Number of qubits in each of the three main registers. The total number of qubits includes the ancillary qubit which is initialized to $|-\rangle$ to implement Grover's oracle. Measurements are made on $n = \sum n_i$ classical bits.

by applying the oracle operations in inverse order. Then, the diffuser U_q is applied to the register $|q\rangle$. We use the diffuser described in the IBM Qiskit website[1].

The upper and lower limit in the number of qubits needed to analyze loop topologies of up to four eloops is summarized in Table 7.1. The final number of qubits depends on the internal configuration of the loop diagram. The lower limit is achieved if $n_i = 1$, the upper limit is saturated for $n_i \geq 2$. Specific details on the implementation of the quantum algorithm and causal clauses are provided in the next section. We use two different quantum simulators: *IBM Quantum* provided by the open source Qiskit framework; and *Quantum Testbed* (QUTE) [161] , a high performance quantum simulator developed and maintained by Fundación Centro Tecnológico de la Información y la Comunicación (CTIC)[2].

The output of the Grover's algorithm described above is a quantum state that is predominantly a superposition of the whole set of causal solutions, with a small contribution from orthogonal states. After a measurement, a single configuration is determined and the superposition is lost. If one requires knowing all solutions and not just a single one, the original output of Grover's algorithm has then to be prepared and measured a certain number of times, also called shots, large enough in order to scan over all causal solutions, and to distinguish them from the less probable noncausal states.

[1] `http://qiskit.org/`
[2] `http://qute.ctic.es/`

The final result is represented by frequency histograms and is affected by the statistical fluctuations that are inherent to the measurements of a quantum system. The proposed approach is based on Grover's search algorithm and, as such, has a similar quantum depth compared to the original implementation and thus a well-known noisy performance on a real present device [162–164]. Given the quantum depth of the algorithm and the resulting difficulties in introducing a reliable error mitigation strategy, we will only consider error-free statistical uncertainties in quantum simulators. Nevertheless, for the sake of benchmarking, we will present a simulation on a real device for the less complex multiloop topology we have analyzed.

We estimate that the number of shots required to distinguish causal from noncausal configurations with a statistical significance of $\Delta\sigma$ standard deviations in a quantum simulator is given by

$$N_{\text{shots}} \approx r\,(\Delta\sigma)^2\left(1+\mathcal{O}(\cos^2(\theta_t))\right)\,, \tag{7.12}$$

assuming that an efficient amplification of the causal states is achieved, i.e. $\cos(\theta_t) \sim 0$. In the following, we will consider $\Delta\sigma \gtrsim 3$, which provides a sufficiently safe discriminant yield with a minimal number of shots.

7.4 Benchmark multiloop topologies

After explaining the connection between acyclic graphs and causality, and introducing the quantum algorithm that identifies the causal configurations of multiloop Feynman diagrams, we present here concrete examples. We consider several topological families of up to four eloops, discussing in each case the explicit implementation of the Boolean clauses and explaining the results obtained.

7.4.1 One eloop

The one-eloop topology shown in Fig. 7.2 A, consists of n vertices connected with n edges along a one-loop circuit. Each vertex has an external particle attached to it, although it is also possible to have vertices without attached external momenta that are the result of collapsing, e.g., a self-energy insertion into a single edge as explained in Sec. 7.1.

We need to test $n-1$ binary clauses, and there is one Boolean condition

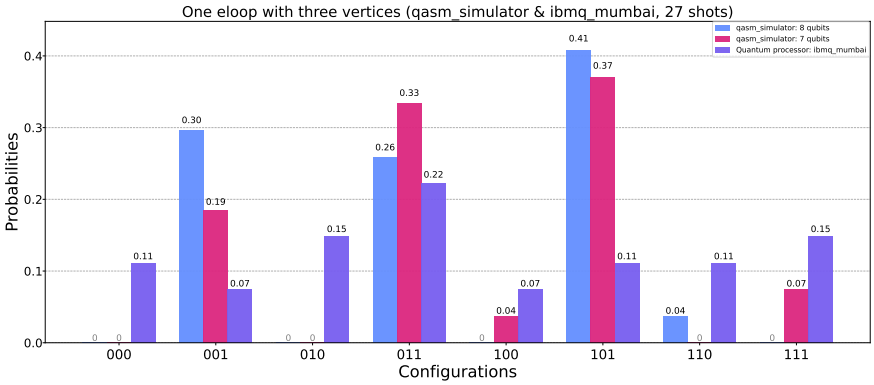

Figure 7.4: Probability distribution of causal and noncausal configurations obtained with (blue) and without (purple) an ancillary qubit for a one-eloop three-vertex topology. Results are presented with both the IBM quantum simulator and the real quantum device.

that has to be fulfilled

$$a_0(\{c_{ij}\}) \equiv \neg\left(c_{01} \wedge c_{12} \wedge \cdots \wedge c_{n-2,n-1}\right) \ . \tag{7.13}$$

The qubit a_0 is set to one if not all the edges are oriented in the same direction. This condition is implemented by imposing a multicontrolled Toffoli gate followed by a Pauli-X gate. We know, however, that this condition is fulfilled for $N-2$ states at one eloop. Therefore, the initial Grover's angle tends to

$$\arcsin\left(\sqrt{(N-2)/N}\right)\Big|_{n\to\infty} = \pi/2\,. \tag{7.14}$$

In order to achieve an efficient suppression of the orthogonal states, we introduce one ancillary qubit, q_n, and select one of the states of one of the qubits representing one of the edges. The required Boolean marker is given by

$$f^{(1)}(a,q) = a_0 \wedge q_0 \wedge q_n \ , \tag{7.15}$$

which is also implemented through a multicontrolled Toffoli gate.

The ratio of probabilities of measuring a winning state versus an orthogonal state is enhanced by adding the ancillary qubit. Alternatively, we can still rely on the original Grover's algorithm when the number of noncausal configurations is small, by swapping the definition of winning and orthogonal states. However, the ancillary qubit is absolutely necessary when the

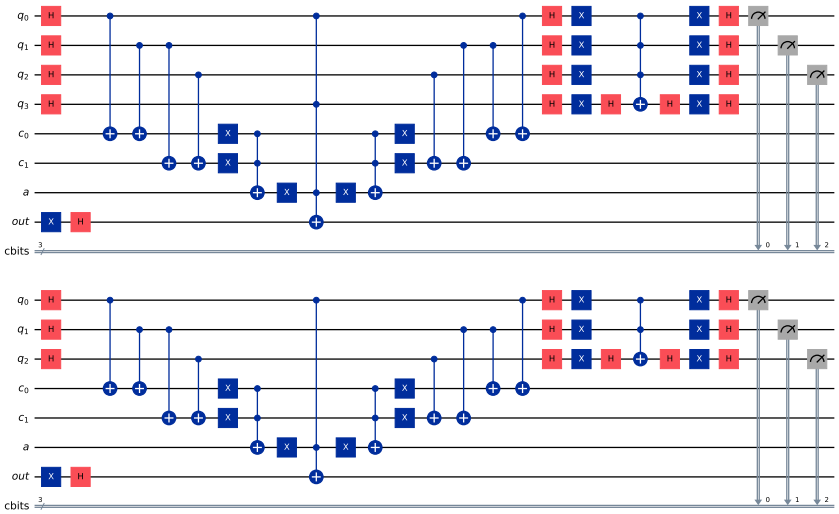

Figure 7.5: Quantum circuits used to bootstrap the causal configuration of a three-vertex one-eloop Feynman diagram. Implementation with (upper plot) and without (lower plot) an ancillary qubit.

number of winning solutions is $\mathcal{O}(N/2)$.

The quantum circuits corresponding to the algorithm for a three-vertex one-eloop topology are represented in Fig. 7.5 and the output in a quantum simulator and a real device is illustrated in Fig. 7.4, where we extract and compare the selection of causal states with and without the ancillary qubit. The ancillary qubit is set in superposition with the other qubits but is not measured because this information is irrelevant. Note that in the Qiskit convention qubits are ordered in such a way that the last qubit appears on the left-most side of the register $|q\rangle$.

The Fig. 7.6 shows the corresponding directed acyclic configurations and the bootstrapped causal interpretation in terms of causal thresholds. Once the direction of the edges is fixed by the quantum algorithm, the causal thresholds are determined by considering all the possible on-shell cuts with aligned edges that are compatible or entangled with each other. This information can be translated directly into the LTD causal representation in Eq. (6.14); the on-shell energies $q_{i,0}^{(+)}$ that contribute to a given causal propagator, $1/\lambda_p^{\pm}$, are those related through the same threshold.

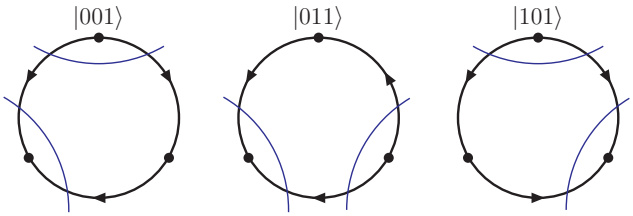

Figure 7.6: Causal bootstrapping of the one-eloop three-vertex topology. Configurations with all internal momentum flows reversed (not shown) are also causal.

The quantum depth of the circuit estimated by Qiskit is $\mathcal{O}(200)$ with the ancillary qubit, and $\mathcal{O}(150)$ without. In both cases, the depth of the circuit is too large to provide a good result in a present real device, as illustrated in Fig. 7.4, and we will focus hereafter on the results obtained by quantum simulations. Results in the quantum simulators are in full agreement with the expectations.

7.4.2 Two eloops

We now analyze multiloop topologies with two eloops. The topologies displayed in Fig. 7.2 B are characterized by three sets of edges, with n_0, n_1 and n_2 insertions in each set and two common vertices. The first non-trivial configuration requires that at least two of the three sets contain two or more edges.

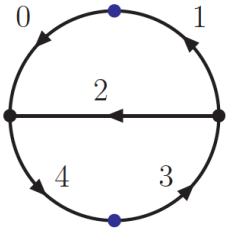

Figure 7.7: Two-eloop five-edge topology.

If $n_0 = n_1 = n_2 = 1$, we have a multibanana or MLT configuration with $L+1$ propagators which is equivalent to one edge, while the NMLT configuration

with $L+2$ sets of propagators, or $n_0 = 2$ and $n_1 = n_2 = 1$, is equivalent to the one-eloop three-vertex topology already analyzed in Sec. 7.4.1 because propagators in the sets 1 and 2 can be merged into a single edge. We consider the five-edge topology depicted in Fig. 7.7 as the first non-trivial configuration at two loops.

The diagram is composed by three subloops, and therefore requires to test three combinations of binary clauses

$$\begin{aligned} a_0 &= \neg\left(c_{01} \wedge c_{13} \wedge c_{34}\right) \ , \\ a_1 &= \neg\left(c_{01} \wedge \bar{c}_{12}\right) \ , \\ a_2 &= \neg\left(c_{23} \wedge c_{34}\right) \ . \end{aligned} \tag{7.16}$$

We know from a classical computation [113] that the number of causal solutions over the total number of states is $18/32 \sim 1/2$. Therefore, it is sufficient to fix the state of one of the edges to reduce the number of states queried to less than $1/4$, while the ancillary q_n-qubit is not necessary. We select q_2 as the qubit whose state is fixed, and check the Boolean condition

$$f^{(2)}(a,q) = (a_0 \wedge a_1 \wedge a_2) \wedge q_2 \ . \tag{7.17}$$

The oracle of the quantum circuit and its output in the IBM's Qiskit simulator are shown in Fig. 7.8, and the causal interpretation is provided in Fig. 7.9. The number of states selected in Fig. 7.8 is 9, corresponding to 18 causal states when considering the mirror configurations obtained by inverting the momentum flows, and in full agreement with the classical calculation.

The generalization to an arbitrary number of edges requires to check first if all the edges in each set are aligned. We define

$$b_s = \bigwedge_{i_s \in s} c_{i_s, i_s+1} \ , \qquad s \in \{0,1,2\} \ . \tag{7.18}$$

The number of subloops is always three, and so the number of conditions that generalize Eq. (7.16)

$$\begin{aligned} a_0 &= \neg\left(b_0 \wedge c_{0_0(n_2-1)} \wedge b_2\right) \ , \\ a_1 &= \neg\left(b_0 \wedge \bar{c}_{(n_0-1)(n_1-1)} \wedge b_1\right) \ , \\ a_2 &= \neg\left(b_1 \wedge c_{(n_1-1)0_2} \wedge b_2\right) \ , \end{aligned} \tag{7.19}$$

where 0_s represents the first edge of the set s, and $(n_s - 1)$ is the last one.

The total number of qubits required to encode these configurations is summarized in Table 7.1. With 32 qubits as the upper limit in the IBM Qiskit simulator, one can consider any two-eloop topology with $\sum n_i \leq 14$ distributed in three sets.

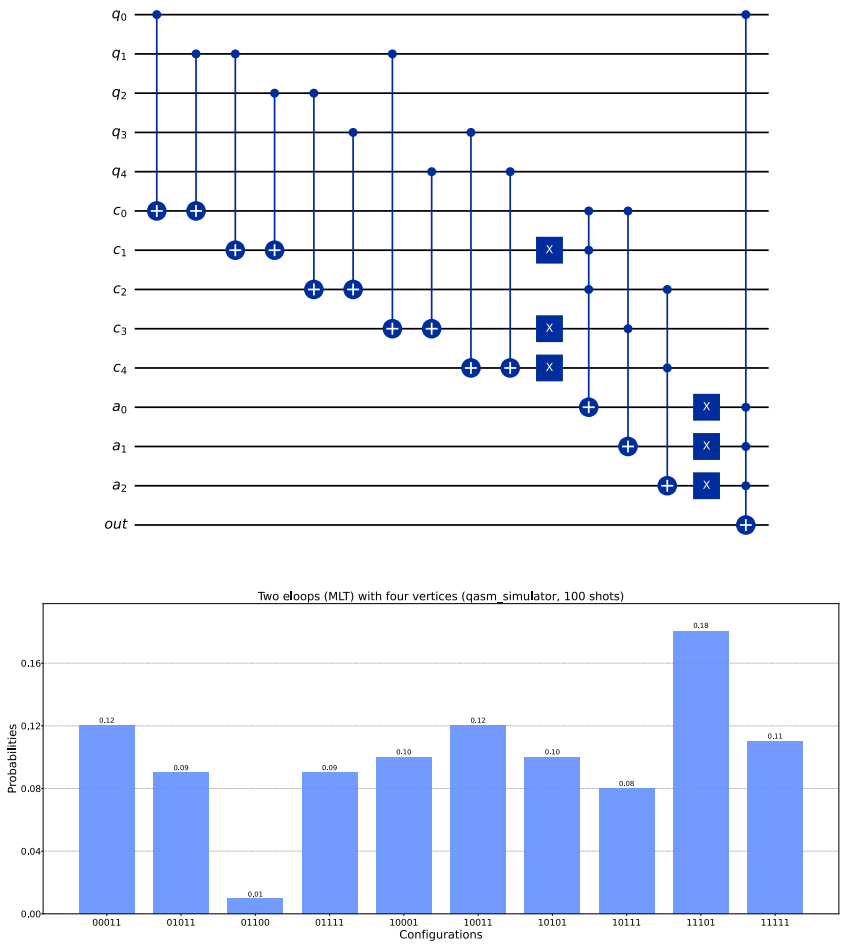

Figure 7.8: Oracle of the quantum circuit (upper plot, omitting the reflection of the quantum gates) and probability distribution of causal and noncausal configurations (lower plot) for a two-eloop topology (MLT) with $n_0 = n_2 = 2$ and $n_1 = 1$ edges.

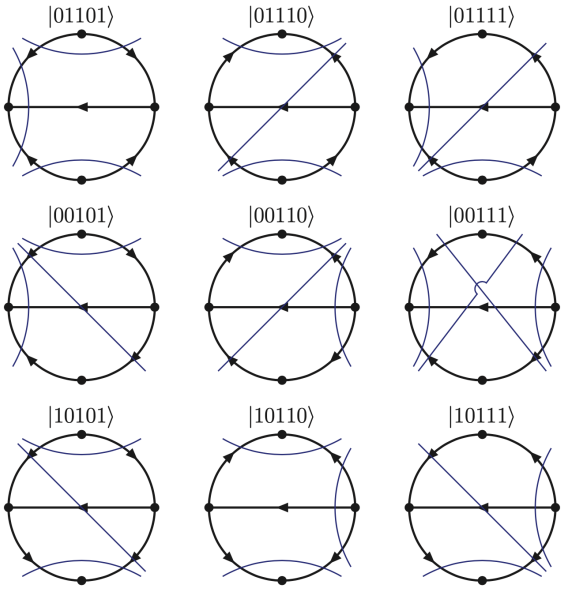

Figure 7.9: Causal bootstrapping of the two-eloop five-edge topology. Configurations with all internal momentum flows reversed (not shown) are also causal.

7.4.3 Three eloops

The N^{2}MLT multiloop topology depicted in Fig. 7.2 C is characterized by four vertices connected through six sets of edges, and n_i edges in each set, $i \in \{0, \ldots, 5\}$; it appears for the first time at three loops. The algorithm for the multiloop topology with $n_i = 1$ requires to test the following eloop clauses

$$\begin{aligned} a_0 &= \neg\left(c_{01} \wedge c_{12}\right) \ , \\ a_1 &= \neg\left(\bar{c}_{04} \wedge \bar{c}_{34}\right) \ , \\ a_2 &= \neg\left(\bar{c}_{15} \wedge \bar{c}_{45}\right) \ , \\ a_3 &= \neg\left(\bar{c}_{23} \wedge \bar{c}_{35}\right) \ . \end{aligned} \tag{7.20}$$

It is worth to notice that the eloop clauses can be implemented in several ways. For example the following expressions are equivalent

$$\left(\bar{c}_{04} \wedge \bar{c}_{34}\right) = \left(c_{03} \wedge \bar{c}_{34}\right) \ . \tag{7.21}$$

However, the expression on the l.h.s. of Eq. (7.21) requires one NOT gate less than the one on the r.h.s., so it is preferable given that it allows to reduce the quantum circuit depth. It is also important to mention that testing eloop clauses involving four edges, such as

$$\neg(\bar{c}_{35} \wedge \bar{c}_{15} \wedge c_{01}) \ , \tag{7.22}$$

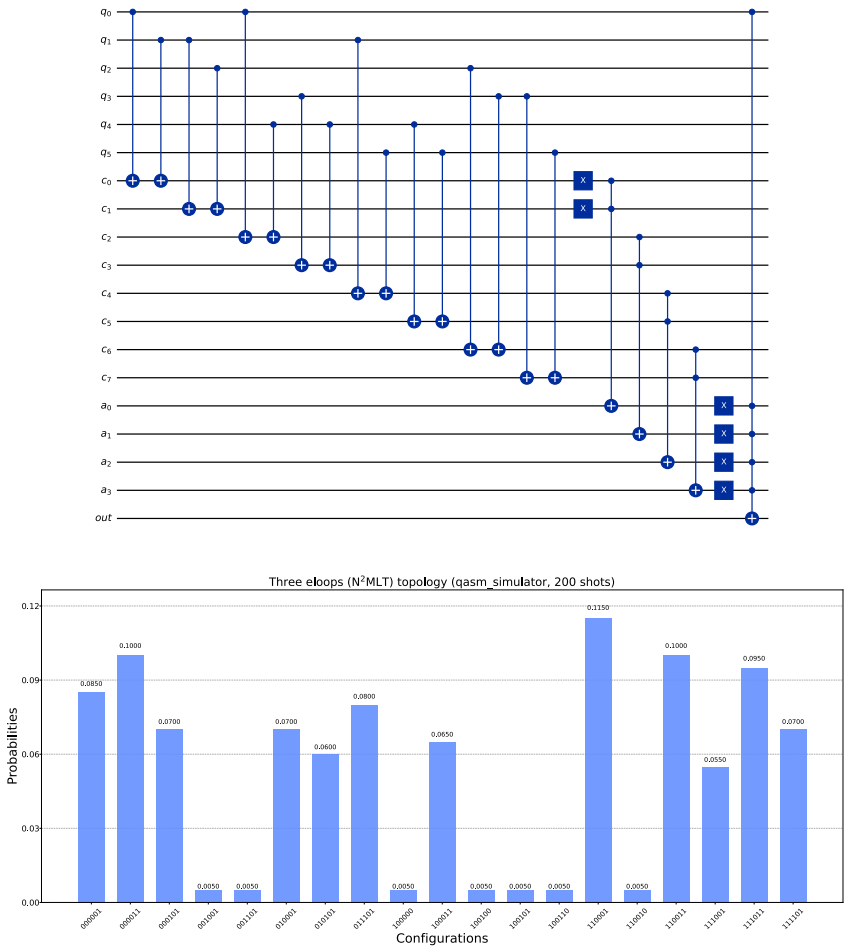

Figure 7.10: Oracle of the quantum circuit (upper plot, omitting the reflection of the quantum gates) and probability distribution of causal and noncausal configurations (lower plot) for a three-eloop topology (Mercedes topology or N^2MLT with $n_i = 1$).

is not necessary because four-edge loops enclose one qubit that in any of its states would create a cyclic three-edge loop if the other four edges are oriented in the same direction.

The final Boolean condition is

$$f^{(3)}(a,q) = (a_0 \wedge \ldots \wedge a_3) \wedge q_0 \ . \tag{7.23}$$

The oracle of the quantum circuit and probability distribution are shown in Fig. 7.10, and the causal interpretation is given in Fig. 7.11. The number of causal configurations is 24 out of 64 states.

For configurations with an arbitrary number of edges the eloop clauses in

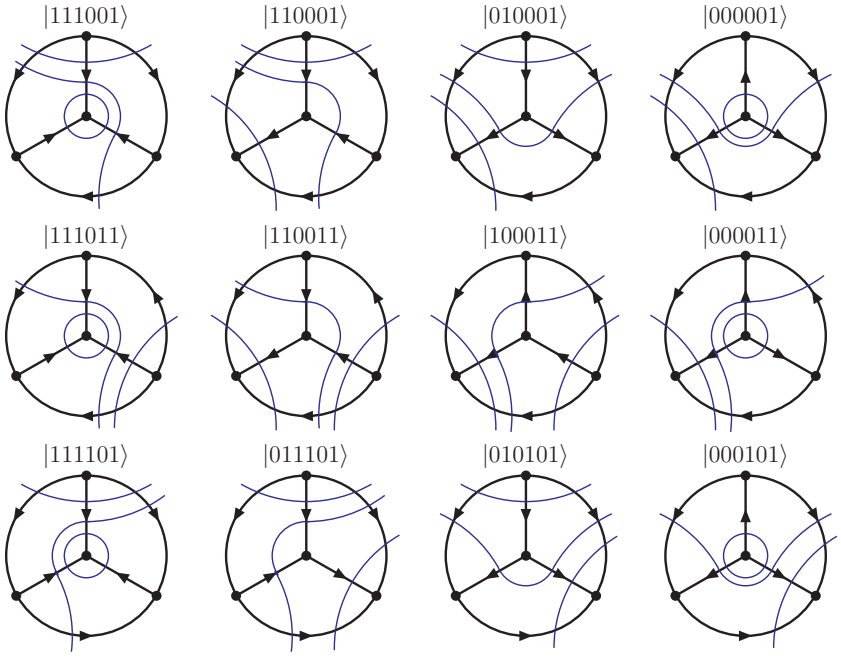

Figure 7.11: Causal bootstrapping of the three-eloop topology (N^2MLT). Configurations with all internal momentum flows reversed (not shown) are also causal.

Eq. (7.20) are substituted by

$$\begin{aligned} a_0 &= \neg \left(b_0 \wedge c_{(n_0-1)0_1} \wedge b_1 \wedge c_{(n_1-1)0_2} \wedge b_2 \right) \ , \\ a_1 &= \neg \left(b_0 \wedge \bar{c}_{(n_0-1)(n_4-1)} \wedge b_4 \wedge \bar{c}_{0_4 0_3} \wedge b_3 \right) \ , \\ a_2 &= \neg \left(b_1 \wedge \bar{c}_{(n_1-1)(n_5-1)} \wedge b_5 \wedge \bar{c}_{0_5 0_4} \wedge b_4 \right) \ , \\ a_3 &= \neg \left(b_2 \wedge \bar{c}_{(n_2-1)(n_3-1)} \wedge b_3 \wedge \bar{c}_{0_3 0_5} \wedge b_5 \right) \ . \end{aligned} \tag{7.24}$$

This is the minimal number of eloop clauses at three eloops. For three-eloop configurations with several edges in each set, an extra binary clause $(c_{(n_2-1)0_0})$ and up to three eloop clauses may be needed to test cycles over

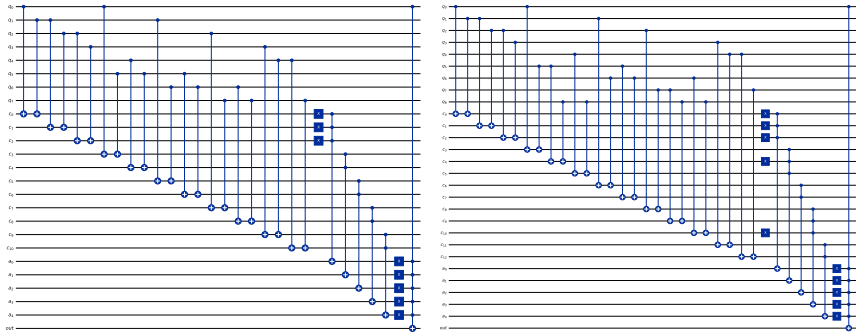

(a) N^{3}MLT (b) t-channel

(c) s-channel (d) u-channel

Figure 7.12: Oracles of the quantum circuits for four-eloop topologies (omitting the reflection of the quantum gates). (a) N^{3}MLT, (b) t-channel, (c) s-channels and (d) u-channel of N^{4}MLT.

four edge sets. These clauses are

$$
\begin{aligned}
a_4 &= \neg \left(b_0 \wedge c_{(n_0-1)0_1} \wedge b_1 \wedge \bar{c}_{(n_1-1)(n_5-1)} \wedge b_5 \wedge \bar{c}_{0_3 0_5} \wedge b_3 \right) \ , \\
a_5 &= \neg \left(b_1 \wedge c_{(n_1-1)0_2} \wedge b_2 \wedge \bar{c}_{(n_2-1)(n_3-1)} \wedge b_3 \wedge \bar{c}_{0_4 0_3} \wedge b_4 \right) \ , \\
a_6 &= \neg \left(b_2 \wedge c_{(n_2-1)0_0} \wedge b_0 \wedge \bar{c}_{(n_0-1)(n_4-1)} \wedge b_4 \wedge \bar{c}_{0_5 0_4} \wedge b_5 \right) \ . \qquad (7.25)
\end{aligned}
$$

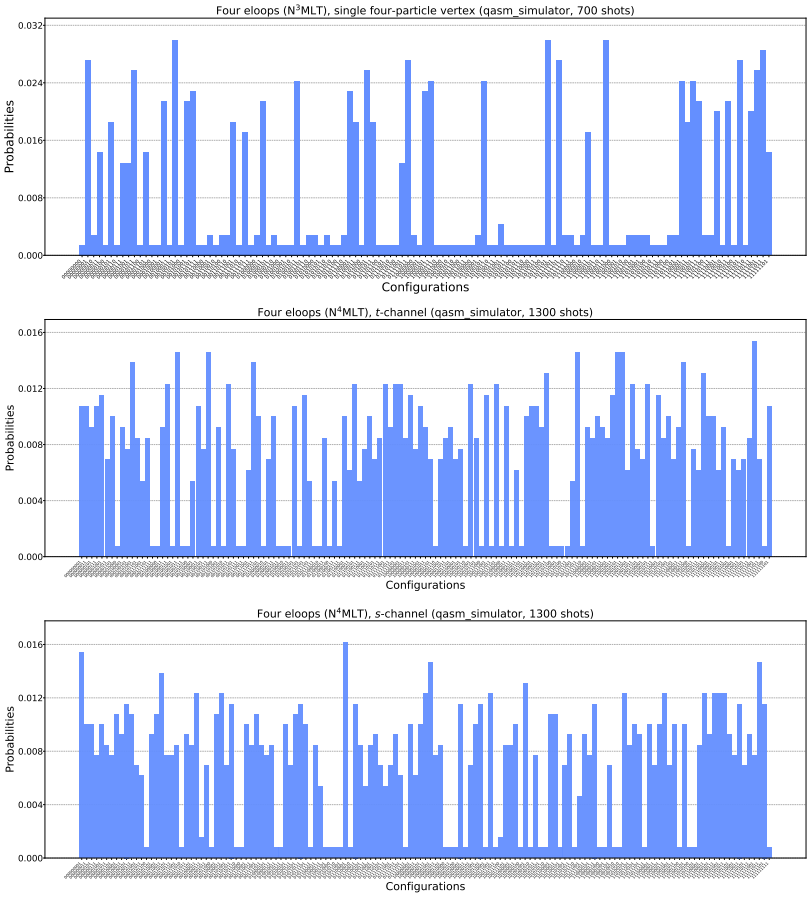

Figure 7.13: Probability distribution of causal and noncausal configurations for four-eloop topologies after 700, 1300 and 1300 shots, respectively. The *qasm_simulator* in the IBM's Qiskit framework was used. From top to bottom: N^3MLT, t-, and s-channels of N^4MLT with $n_i = 1$. The number of selected states is 39/256, 102/512 and 102/512, respectively.

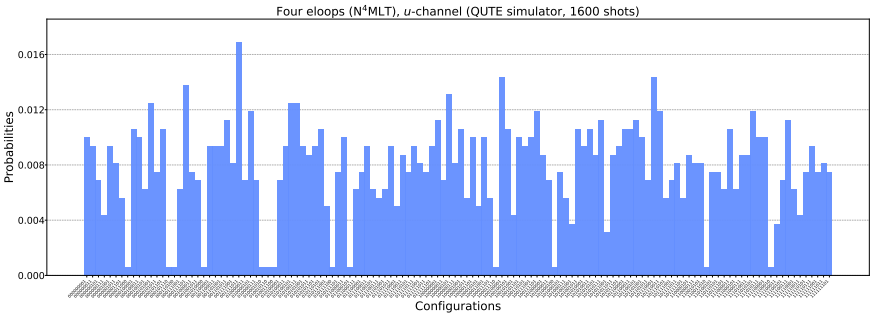

Figure 7.14: Probability distribution of causal and noncausal configurations for the four-eloop u-channel after 1600 shots in the QUTE Testbed framework. The number of selected states is 115/512.

The number of qubits reaches the upper limit reflected in Table 7.1 for $n_i \geq 2$.

7.4.4 Four eloops

Considering a complexity of four eloops, we take into account the four-eloop topologies shown in Fig. 7.2. The N^{3}MLT multiloop topology is characterized by 8 sets of edges connected through 5 vertices. For $n_i = 1$, with $i \in \{0, \ldots, 7\}$, the eloop clauses are

$$\begin{aligned} a_0^{(4)} &= \neg\left(c_{01} \wedge c_{12} \wedge c_{23}\right) \ , \\ a_1^{(4)} &= \neg\left(\bar{c}_{05} \wedge \bar{c}_{45}\right) \ , \\ a_2^{(4)} &= \neg\left(\bar{c}_{16} \wedge \bar{c}_{56}\right) \ , \\ a_3^{(4)} &= \neg\left(\bar{c}_{27} \wedge \bar{c}_{67}\right) \ , \\ a_4^{(4)} &= \neg\left(\bar{c}_{34} \wedge \bar{c}_{47}\right) \ , \end{aligned} \tag{7.26}$$

and the Boolean test function is

$$f^{(4)}(a, q) = (a_0^{(4)} \wedge \ldots \wedge a_4^{(4)}) \wedge q_0 \ . \tag{7.27}$$

Some of the eloop clauses in Eq. (7.26) are common to the t-, s- and u-channels, which are inclusively denoted as N^{4}MLT as they involve each one extra set of edges with respect to N^{3}MLT. The channel specific eloop clauses

needed are

$$\begin{aligned} a_1^{(t)} &= \neg\left(\bar{c}_{05} \wedge c_{58} \wedge \bar{c}_{48}\right) \ , \\ a_3^{(t)} &= \neg\left(\bar{c}_{27} \wedge \bar{c}_{78} \wedge c_{68}\right) \ , \end{aligned} \tag{7.28}$$

for the t-channel,

$$\begin{aligned} a_2^{(s)} &= \neg\left(\bar{c}_{16} \wedge \bar{c}_{68} \wedge c_{58}\right) \ , \\ a_4^{(s)} &= \neg\left(\bar{c}_{34} \wedge c_{48} \wedge \bar{c}_{78}\right) \ , \end{aligned} \tag{7.29}$$

for the s-channel, and

$$\begin{aligned} a_3^{(u)} &= \neg\left(\bar{c}_{27} \wedge c_{78} \wedge \bar{c}_{68}\right) \ , \\ a_4^{(u)} &= \neg\left(\bar{c}_{34} \wedge \bar{c}_{48} \wedge c_{78}\right) \ , \\ a_5^{(u)} &= \neg\left(c_{01} \wedge \bar{c}_{16} \wedge \bar{c}_{46}\right) \ , \\ a_6^{(u)} &= \neg\left(c_{12} \wedge \bar{c}_{27} \wedge \bar{c}_{57}\right) \ , \\ a_7^{(u)} &= \neg\left(c_{23} \wedge \bar{c}_{34} \wedge \bar{c}_{46}\right) \ , \\ a_8^{(u)} &= \neg\left(c_{03} \wedge \bar{c}_{05} \wedge \bar{c}_{57}\right) \ , \end{aligned} \tag{7.30}$$

for the u-channel. The number of eloop clauses for the u-channel is much larger than for the other configurations because it is the first nonplanar diagram.

Each of the t-, s- and u-channels is characterized by one of the following Boolean conditions

$$\begin{aligned} f^{(4,t)}(a,q) &= \left(a_0^{(4)} \wedge a_1^{(t)} \wedge a_2^{(4)} \wedge a_3^{(t)} \wedge a_4^{(4)}\right) \wedge q_0 \ , \\ f^{(4,s)}(a,q) &= \left(a_0^{(4)} \wedge a_1^{(4)} \wedge a_2^{(s)} \wedge a_3^{(4)} \wedge a_4^{(s)}\right) \wedge q_0 \ , \\ f^{(4,u)}(a,q) &= \left(a_0^{(4)} \wedge a_1^{(t)} \wedge a_2^{(s)} \wedge a_3^{(u)} \wedge \ldots \wedge a_8^{(u)}\right) \wedge q_0 \ . \end{aligned} \tag{7.31}$$

The number of qubits required for each configuration is given by the lower ranges of Table 7.1, i.e. 25, 28, 28 and 33 qubits respectively. Despite the complexity of these topologies, the quantum algorithm is well supported by IBM Quantum simulator capacity in the N^{3}MLT, t- and s-channels. In Fig. 7.13, the outputs obtained from these configurations are shown. Regarding the non planar configuration, the u-channel, it was tested within the QUTE Testbed framework as it supports more than 32 qubits (see Fig. 7.14). Following the procedure described for three-eloop topologies, more complex

topologies with $n_i \geq 1$ are also amenable to the quantum algorithm, although they may soon exceed the current capacity of the quantum simulator. The corresponding oracles of the quantum circuits are presented in Fig. 7.12 and representative bootstrapped diagrams at four eloops are shown in Fig. 7.15.

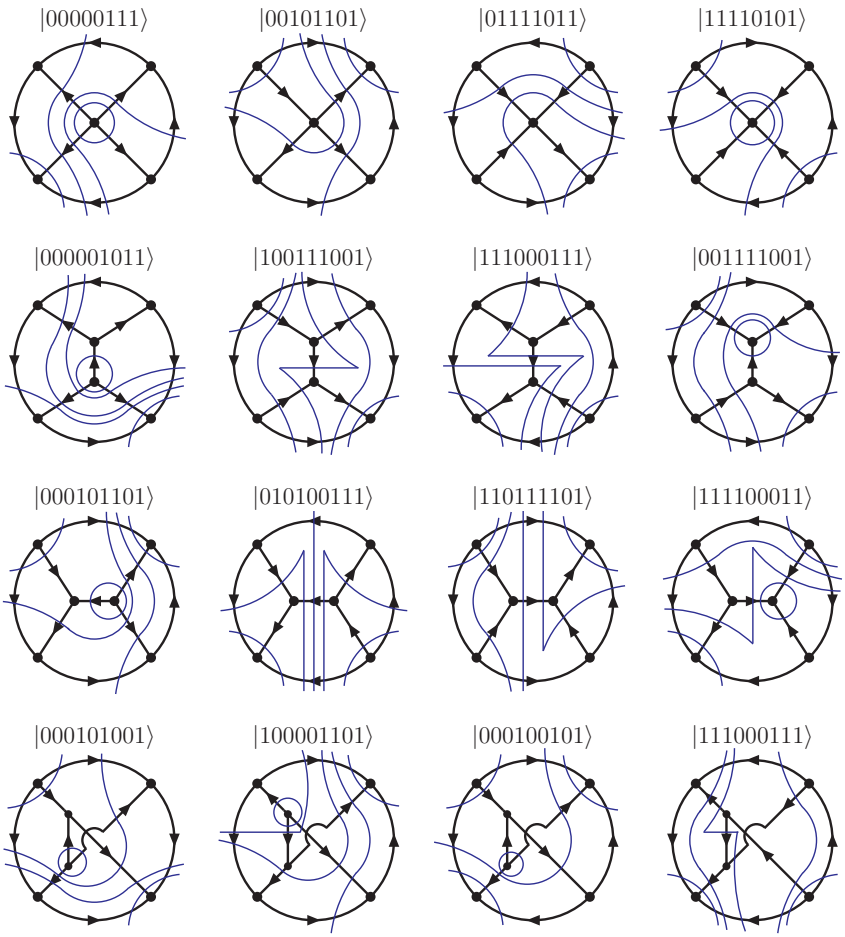

Figure 7.15: Representative bootstrapped diagrams at four eloops, from the quantum algorithm output in Figs. 7.13 and 7.14.

In Sec. 7.3 we have presented the most recent developments in LTD combined with the exploration of quantum algorithms in perturbative Quantum Field Theory. In particular, a quantum algorithm for causal querying and its implementation was presented in Sec. 7.4. It succeeded to unfold the causal configurations of selected multiloop Feynman diagrams up to four loops.

Chapter 8

Conclusions

The evolution of the LTD framework has undergone significant improvements during the past few years. A new strategy based on the application of nested residues to open any multiloop scattering amplitude to connected trees, allowed to reformulate the Loop-Tree Duality at higher perturbative orders. The key development that enabled this reformulation is presented in Chapter 4, considering selected multiloop topologies to all orders with $L + 3$ sets of propagators. The direct LTD representations are expressed in a very compact open-into-tree analytical expressions exhibiting a factorized cascade form in terms of simpler subtopologies. Since this factorized structure is imposed by the opening into connected trees and by causality, we expected that it holds to all loop orders and topologies. Remarkably, the dual expressions presented are free of unphysical singularities and independent of the initial momentum flow. This property has been tested with all the topologies and several internal configurations. We also conjectured that analytic dual representations in terms of only causal denominators are always possible.

The extension of the results found in Chapter 4 have been developed with the analysis of the multiloop topologies that appear for the first time at four loops in Chapter 5. We found out that this family could be represented by three main topologies and unified them in a unique representation, the N^4MLT *universal topology*. We have described its opening to connected trees through the Loop-Tree Duality. As we expected, the opening to trees admits a very structured and compact factorized interpretation in terms of convolutions of known subtopologies, that finally determine the internal

causal structure of the entire amplitude. The LTD representation presented is valid in arbitrary coordinate systems and space-time dimensions.

The N^4MLT topology is called universal because it unifies in a single expression all the necessary ingredients to open any scattering amplitude of up to four loops. Regarding causality, we have verified that the LTD representation of N^4MLT is causal, namely, that the explicit LTD analytic expression is manifestly free of noncausal singularities. Furthermore, the ideas and results of the causal analysis of Ref. [113] are extended by one perturbative order, the causal LTD representation is explicitly found and reinterpreted in terms of entangled causal thresholds, for the multiloop N^3MLT and the t-, s- and u-channels. We have shown a desired numerical stability behaviour at integrand-level from the analysis of an explicit causal LTD expression. The causal scenario allows one to work with favorable conditions, the absence of noncausal singularities, enabling to get a more efficient numerical evaluation of multiloop scattering amplitudes. In addition, all these results confirm the all-order conjecture of Ref. [6].

Beyond four loops, the methodology presented here was used as a guide to achieve a detailed description of the topologies that arise for the fist time at five loops. The explicit LTD expressions presented through Chapter 4, 5 and 6 are sufficient to describe any scattering amplitude up to five loops. Moreover, the reformulation of the LTD presented allows for a direct and efficient application to physical scattering processes, and is also advantageous to unveil formal aspects of multiloop scattering amplitudes.

Delving into the causal representation scenario, a solution to a challenging exercise at higher orders is presented in Chapter 7, the search of all internal causal configurations among 2^n potential solutions, where n is the number of edges. To address this problem we explored alternative methodologies through a quantum computing approach. We have presented the first proof-of-concept of a quantum algorithm to efficiently reconstruct multiloop multileg Feynman integrals exploiting the Loop-Tree Duality and causality. The concrete problem addressed was the identification of all the causal singular configurations of the loop integrand resulting from setting on-shell internal Feynman propagators. This information is useful both for identifying the physical discontinuities of the Feynman loop integral and to bootstrap its causal representation in the loop-tree duality.

We have proposed a modified Grover's quantum algorithm, described it in general terms, and have provided specific details on its implementation for selected multiloop configurations. These cases were successfully handled by IBM Quantum and QUTE quantum simulators. Given the quantum depth of the algorithm, its execution in current real devices leads to unreliable results due to hardware limitations. However, the quantum simulators successfully identify all causal states even for the most complex multiloop configurations considered. Given the rapid progress being made in this field, it is expected that present technological limitations will soon be overcome.

The knowledge and experience acquired through the developments presented in this thesis have prepared the path for recalling the FDU algorithm, a method developed to construct purely four dimensional representations of higher order perturbative contributions to physical cross-sections, this time through a convenient causal scenario. This is a work in progress that involves the identification of suitable mappings between the external and loop momenta of the virtual scattering amplitudes, and the external momenta of the real emission corrections through the LTD causal framework. To accomplish the cancellation of the infrared divergences locally without introducing subtraction counter-terms, we will take advantage of virtual and real contributions expressed in a causal representation to perform the sum over degenerate infrared states at integrand level.

Chapter 9

Resumen

9.1 Introducción

La impresionante evolución en la comprensión de las interacciones fundamentales y componentes elementales de la Naturaleza, se debe a la capacidad para obtener predicciones teóricas precisas a partir de la Teoría Cuántica de Campos. La construcción de estas predicciones teóricas en física de partículas a altas energías se basa principalmente en teorías perturbativas, las cuales han mostrado una extraordinaria eficiencia. Sin embargo, la necesidad de alcanzar órdenes perturbativos más altos con el objetivo de obtener predicciones más precisas, ha puesto al descubierto retos importantes.

La principal dificultad en Teoría Cuántica de Campos perturbativa, tiene su origen en la descripción de las fluctuaciones cuánticas en los procesos de dispersión y desintegración a altas energías mediante el cálculo de amplitudes de dispersión multilazo considerando múltiples partículas externas. La estructura matemática intrínseca de los diagramas de lazo de Feynman, genera singularidades físicas y no físicas cuyo comportamiento complejo dificulta las evaluaciones numéricas. Considerando el escenario experimiental, los retos en física de altas energías debidos a la tercera etapa de toma de datos (Run 3) del Gran Colisionador de Hadrones (LHC) del CERN [19], la próxima fase de alta luminosidad [20], y los colisionadores futuros previstos [8–11, 16, 21–24], están empujando la frontera de precisión hacia predicciones teóricas aún más precisas y una mejor comprensión del comportamiento cuántico de dichos objetos.

Para una evaluación numérica robusta de las integrales con lazos múltiples, es necesario un tratamiento adecuado de las singularidades. Con el objetivo de hacer frente a este desafío, se han realizado grandes esfuerzos en el campo para proporcionar metodologías apropiadas [25]. No obstante, todavía se tiene un gran camino por recorrer; nuevas metodologías y estrategias son requeridas para afrontar la necesidad de mejorar la precisión teórica en colisionadores de altas energías. Para afrontar estas necesidades, esta tesis profundiza en una metodología novedosa que expresa cualquier diagrama de lazo en diagramas conectados de tipo árbol, la Dualidad Lazo-Árbol. Adicionalmente, se exploran enfoques alternativos para proporcionar soluciones adecuadas y más completas.

9.2 Dualidad Lazo-Árbol

La Dualidad Lazo-Árbol (LTD) [81, 84, 85] es una metodología sumamente eficaz para analizar la estructura singular en las amplitudes de dispersión directamente en el espacio de momentos de lazo. La característica más importante es la capacidad de restringir todas las singularidades infrarrojas (IR) y umbrales físicos a una región compacta del espacio de integración, lo que lleva a una distinción manifiesta entre singularidades físicas y no físicas a nivel del integrando [7, 88].

El conocimiento adquirido en el manejo de las singularidades, fue crucial para el desarrollo de la desustracción cuatridimensional (FDU) [80, 93, 96, 97], la cual permite combinar las correcciones reales y virtuales en una única integral numéricamente estable. El objetivo de FDU es realizar la mayoría de los cálculos directamente en las cuatro dimensiones físicas del espacio-tiempo. Además, el formalismo LTD posee otras características que lo convierten en una técnica prometedora para abordar cálculos perturbativos de orden superior, por ejemplo, el número de variables de integración en las implementaciones numéricas es independiente del número de partículas externas [94, 95, 106, 107, 112]. Además, LTD proporciona eficazmente expansiones asintóticas [101, 103, 104], y también constituye una estrategia prometedora hacia los enfoques de renormalización ultravioleta (UV) local [102].

Durante el año 2019, la metodología LTD recibió una atención especial por parte de otros grupos [109–112] y exploramos nuevas estrategias para

la aplicación de la LTD, además, planteamos una pregunta clave:

¿Es posible encontrar expresiones analíticas explícitas y más compactas con el formalismo LTD a todos los órdenes?

El desarrollo para responder a esta pregunta, es el pilar de los últimos resultados en el escenario de LTD, y es el punto de partida en la evolución de la presente tesis. A continuación introducimos la notación utilizada para describir cualquier amplitud de dispersión, así como el procedimiento para su correspondiente apertura a través del formalismo LTD.

Una amplitud de dispersión de L lazos, con P partículas externas $\{p_j\}_P$ y $n = L + k$ conjuntos de momentos internos, se define en la representación de Feynman como una integral en el espacio de Minkowski de los L momentos de lazo, $\{\ell_s\}_L$,

$$\mathcal{A}^{(L)}(1,\ldots,L+k) = \int_{\ell_1,\ldots,\ell_L} \mathcal{A}_F^{(L)}(1,\ldots,L+k)\,, \tag{9.1}$$

donde la medida de integración en regularización dimensional [74, 75] está dada por

$$\int_{\ell_s} = -\imath\mu^{4-d} \int \frac{d^d\ell_s}{(2\pi)^d}\,, \tag{9.2}$$

con d el número de dimensiones espacio-temporales y μ una escala de energía arbitraria. El integrando en la Eq. (9.1) está dado por

$$\mathcal{A}_F^{(L)}(1,\ldots,L+k) = \mathcal{N}(\{\ell_s\}_L, \{p_j\}_P)\; G_F(1,\ldots,L+k)\,, \tag{9.3}$$

donde el numerador $\mathcal{N}$ está determinado por los vértices de interacción y el tipo de partículas que se propagan en la teoría considerada. La notación compacta establecida para el producto de un conjunto de propagadores de Feynman que dependen de un momento de lazo específico, o la unión de varios conjuntos que dependen de una combinación lineal de diferentes momentos de lazo, está dado por

$$G_F(1,\ldots,L+k) = \prod_{i\in 1\cup\ldots\cup L+k} (G_F(q_i))^{a_i}\,, \tag{9.4}$$

donde a_i es una potencia arbitratia. Es importante mencionar que de este punto en adelante las potencias a_i estarán de manera implícita. La configuración interna de $\mathcal{A}_F^{(L)}$ está implícitamente especificada a través de la asignación inicial en los conjuntos de momentos internos.

El propagador de Feynman se escribe de manera conveniente como

$$G_F(q_i) = \frac{1}{(q_{i,0} - q_{i,0}^{(+)})(q_{i,0} + q_{i,0}^{(+)})} \,, \tag{9.5}$$

mostrando de manera explícita la localización de sus polos,

$$q_{i,0}^{(+)} = \sqrt{\mathbf{q}_i^2 + m_i^2 - \imath 0}, \tag{9.6}$$

con $q_{i,0}$ y $\mathbf{q}_i$ las componentes temporal y espacial de q_i, respectivamente, y m_i la masa de la partícula.

Respecto al cálculo de la representación LTD a un lazo, éste se obtiene integrando un grado de libertad en el momento del lazo a través del teorema de residuo de Cauchy [81]. En el contexto de las amplitudes de disperisión con lazos múltiples, se integra un grado de libertad por lazo. La táctica que se propone y se sigue en esta tesis, es diferente de la desarrollada en Ref. [84], en este caso, la aplicación del teorema de residuo de Cauchy la realizamos iterativamente, obteniendo la representación LTD en términos de residuos anidados

$$\begin{aligned} &\mathcal{A}_D^{(L)}(1,\dots,r;r+1,\dots,L+k) \\ &= -2\pi\imath \sum_{i_r \in r} \mathrm{Res}(\mathcal{A}_D^{(L)}(1,\dots,r-1;r,\dots,L+k), \mathrm{Im}(\eta \cdot q_{i_r}) < 0) \,, \end{aligned} \tag{9.7}$$

empezando con

$$\begin{aligned} &\mathcal{A}_D^{(L)}(1;2,\dots,L+k) \\ &= -2\pi\imath \sum_{i_1 \in 1} \mathrm{Res}(\mathcal{A}_F^{(L)}(1,\dots,L+k), \mathrm{Im}(\eta \cdot q_{i_1}) < 0) \,, \end{aligned} \tag{9.8}$$

donde $\mathcal{A}_F^{(L)}(1,\dots,L+k)$ es el integrando en la representación de Feynman en Ec. (9.1). Respecto a la Ec. (9.7), los conjuntos de momentos antes del punto y coma son linearmente indepencientes, y cada uno de ellos contiene exactamente un propagador sobre la capa de masas, mientras que aquellos propagadores correspondientes a los conjuntos ubicados después del punto y coma se mantienen fuera de su capa de masas. La suma sobre todas las posibles configuraciones de propagadores sobre su capa de masas en $\mathcal{A}_D^{(L)}$ se entiende implícitamente a través de la suma de residuos.

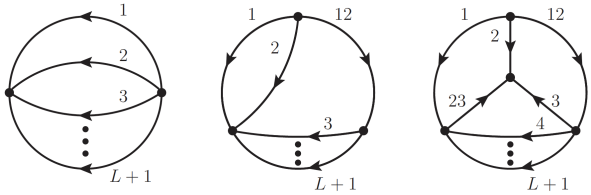

a) MLT b) NMLT c) N^{2}MLT

Figure 9.1: De izquierda a derecha: Maximal Loop Topology (MLT), Next-to-Maximal Loop Topology (NMLT) y Next-to-Next-to-Maximal Loop Topology (N^{2}MLT). Cada línea interna puede representar un número arbitrario de propagadores y por lo tanto un número arbitrario de partículas externas adscritas.

Los residuos se evalúan mediante la selección de los polos con componentes imaginarias negativas aplicando el vector η, mediante el cual se selecciona la componente del momento del lazo que será integrada. De manera conveniente se toma $\eta^\mu = (1, \mathbf{0})$, lo cual permite trabajar en el dominio de integración del trimomento del lazo de un espacio Euclideo, en lugar de trabajar en el espacio de Minkowski.

9.3 Apertura de amplitudes con lazos a todos los órdenes con la Dualidad Lazo-Árbol

En esta sección se presenta la generalización de la Dualidad Lazo-Árbol a todos los órdenes perturbativos preservando la invariancia Lorentz (independiente del marco de referencia), i.e., de tal modo que la prescripción dual corresponde a la introducida en la formulación original a un lazo [81].

La manera de proceder para reformular LTD fue evaluar los residuos iterados para una selección inicial de topologías multilazo. Estas topologías, mostradas en la Fig. 9.1, codifican de un modo universal una amplia variedad de configuraciones internas. Las expresiones encontradas nos permiten identificar un patrón para formular un *Ansatz* a todos los órdenes perturbativos, el cual finalmente se demuestra por inducción. Es importante remarcar que la forma funcional obtenida no depende de la posición de los polos en el plano complejo.

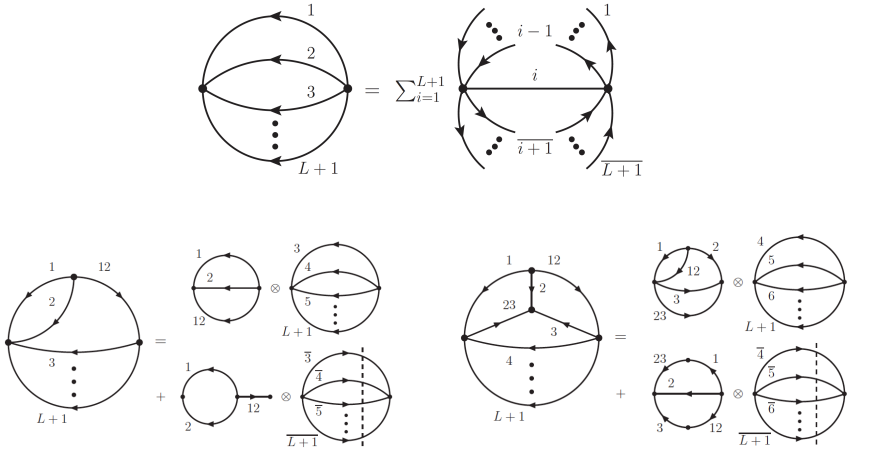

Figure 9.2: Representación diagramática de la apertura dual de las topologías multilazo MLT (arriba), NMLT (abajo/izquierda) y N^{2}MLT (abajo/derecha).

La primera amplitud multilazo analizada es conocida como Maximal Loop Topology (MLT), representada diagramáticamente en la Fig. 9.1(izquierda). Su apertura dual es extremadamente simple y simétrica,

$$\begin{aligned}&\mathcal{A}^{(L)}_{\text{MLT}}(1,\ldots,L+1)\\&=\int_{\ell_1,\ldots,\ell_L}\sum_{i=1}^{L+1}\mathcal{A}^{(L)}_{D}(1,\ldots,i-1,\overline{i+1},\ldots,\overline{L+1};i)\ ,\end{aligned}\tag{9.9}$$

con $\mathcal{A}^{(L)}_{D}(\overline{2},\ldots,\overline{L+1};1)$ y $\mathcal{A}^{(L)}_{D}(1,\ldots,L;L+1)$ como primer y último elemento de la suma, respectivamente. Las barras sobre los conjuntos indican una inversión del flujo de momento, que equivale a seleccionar los modos sobre la capa de masas con energía negativa respecto al flujo de momento original.

En cada término de la suma en el integrando de la Ec. (9.9), hay un conjunto i con todos sus propagadores fuera de la capa de masas, y en cada uno de los otros L conjuntos se tiene un propagador sobre la capa de masas. Esta es la condición necesaria para abrir la amplitud multilazo en árboles conectados. Nótese también, que hay una suma implícita considerando todas las posibles configuraciones sobre la capa de masas de los L conjuntos. La representación LTD en la Ec. (9.9) se muestra gráficamente en la Fig. 9.2(arriba),

y constituye el bloque de construcción básico para la apertura de cualquier topología.

La siguiente topología multilazo en complejidad aparece por primera vez a tres lazos, la representación diagramática se muestra en la Fig. 9.1(centro) y es conocida como Next-to-Maximal Loop topology (NMLT). Esta topología se caracterizada por tener $L+2$ conjuntos, uno de ellos denotado por 12. La representación LTD se muestra en la Fig. 9.2(abajo/izquierda) y se escribe de forma compacta y factorizada,

$$\begin{aligned}\mathcal{A}^{(L)}_{\rm NMLT}&(1,\ldots,L+1,12)\\ &= \mathcal{A}^{(2)}_{\rm MLT}(1,2,12)\otimes\mathcal{A}^{(L-2)}_{\rm MLT}(3,\ldots,L+1)\\ &+ \mathcal{A}^{(1)}_{\rm MLT}(1,2)\otimes\mathcal{A}^{(L-1)}_{\rm MLT}(\overline{3},\ldots,\overline{L+1})\ ,\end{aligned} \tag{9.10}$$

generando un número total de $3L-1$ términos. El primer término en el r.h.s. de la Ec. (9.10) representa una convolución de la subtopología MLT a dos lazos que involucra los conjuntos $(1,2,12)$ con el resto de la amplitud, que también es MLT. Cada componente MLT de la convolución se abre acorde a la la Ec. (9.9). En el segundo término del r.h.s. de la Ec. (9.10), el conjunto 12 permanece fuera de la capa de masas, mientras que en 1 o en $\overline{2}$ hay propagadores sobre la capa de masas, además, todos los conjuntos invertidos (desde 3 hasta $L+1$) contienen propagadores sobre la capa de masas.

Para hacer la notación más comprensible, $\mathcal{A}^{(L)}_{\rm N^{k-1}MLT}$ y $\mathcal{A}^{(L)}_{D}$ se referirán en lo sucesivo, al integrando de la topología correspondiente en la representación LTD; la integración sobre los momentos de lazo L será entendida de manera implícita. Una simplificación adicional es considerada, omitir la referencia explícita a los conjuntos con todos sus propagadores fuera de la capa de masas; por ejemplo,

$$\mathcal{A}^{(1)}_{\rm MLT}(1,2)\otimes\mathcal{A}^{(2)}_{\rm MLT}(\overline{3},\overline{4}) = \mathcal{A}^{(3)}_{D}(1,\overline{3},\overline{4};2,12)\ +\mathcal{A}^{(3)}_{D}(\overline{2},\overline{3},\overline{4};1,12)\ . \tag{9.11}$$

Esta notación se utilizará en lo venidero, asumiendo que los conjuntos omitidos están fuera de la capa de masas.

La última topología considera explícitamente en el estudio para la reformulación de la metodología LTD, es la Next-to-Next-to-Maximal Loop Topology ($\rm N^2MLT$) representada en la Fig. 9.1(izquierda). A tres lazos, cor-

responde a la bien conocida topología Mercedes-Benz. Además del conjunto 12, es necesario añadir un conjunto extra denotado por 23. Su representación LTD se muestra en Fig. 9.2(abajo/derecha), y viene dada por la siguiente convolución de subtopologías factorizadas

$$\begin{aligned}\mathcal{A}^{(L)}_{\mathrm{N^2MLT}}&(1,\ldots,L+1,12,23)\\ &= \mathcal{A}^{(3)}_{\mathrm{NMLT}}(1,2,3,12,23)\otimes\mathcal{A}^{(L-3)}_{\mathrm{MLT}}(4,\ldots,L+1)\\ &+\mathcal{A}^{(2)}_{\mathrm{MLT}}(1\cup 23,2,3\cup 12)\otimes\mathcal{A}^{(L-2)}_{\mathrm{MLT}}(\overline{4},\ldots,\overline{L+1})\ ,\end{aligned}\tag{9.12}$$

generando $8(L-1)$ términos duales. Los conjuntos $(1,2,3,12,23)$ forman una subtopología NMLT, por lo tanto, el primer componente del primer término en el r.h.s de la Ec. (9.12) se abre iterativamente. El segundo término en el r.h.s. de la Ec. (9.12) contiene una subtopología de dos lazos formada por cinco conjuntos de momentos, $\mathcal{A}^{(2)}_{\mathrm{MLT}}(1\cup 23,2,3\cup 12)$, que se agrupan en tres conjuntos y se dualizan a través de la Ec. (9.9). Por ejemplo, los propagadores de los conjuntos 1 y 23 no se fijan simultáneamente sobre la capa de masas.

A partir de la reformulación LTD, se logra escribir de manera muy compacta, y factorizada en términos de convoluciones de subtopologías conocidas como se observa en la Fig. 9.2. Las expresiones que se obtienen son totalmente independientes, a nivel integrando, de la configuración inicial de los flujos de momento en la representación de Feynman y, notablemente, manifiestamente libres de singularidades no causales.

La extensión de este resultado fue aplicado a topologías multilazo con mayor complejidad, aquellas que aparecen por primera vez a cuatro lazos. Esta familia multilazo está representada por tres topologías, las cuales son asimilables a la inserción de una subamplitud de cuatro puntos con vértices trivalentes en una topología mayor. Así pues, para lograr una descripción unificada, estas tres topologías son interpretadas como los canales t, s y u, respectivamente, de una *topología universal* $\mathrm{N^4MLT}$.

Las tres topologías contienen $L+4$ conjuntos comunes de propagadores, y uno adicional que es diferente en cada una de ellas. Los conjuntos diferentes son la clave para caracterizar los tres canales de la *topología universal*. Para ensamblar estos canales $\mathrm{N^4MLT}$ en una sola topología, se define la

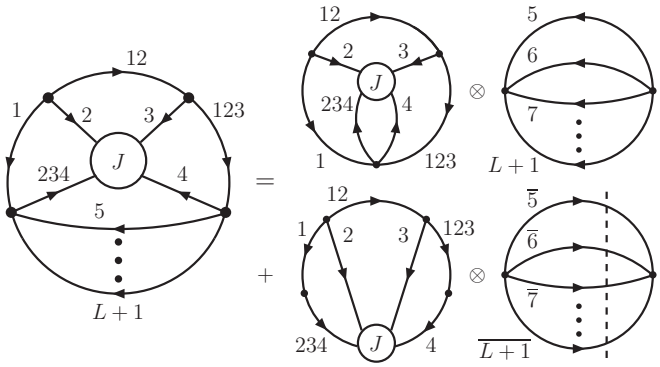

Figure 9.3: Representación diagramática de la apertura factorizada de la topología N^{4}MLT, la *topología universal*. Sólo los cortes de los propagadores sobre la capa de masas de la última subtopología MLT con flujos de momento invertidos se muestra explícitamente.

corriente J que incluye los tres conjuntos diferentes,

$$J \equiv 23 \cup 34 \cup 24 \ . \tag{9.13}$$

Notemos que debido a la conservación de momento, los tres subconjuntos no pueden contribuir al mismo diagrama de Feynman de forma individual, sino que todos contribuyen a nivel de la amplitud. Considerando el planteamiento descrito, la representación de Feynman de la topología universal N^{4}MLT puede expresarse como

$$\mathcal{A}^{(L)}_{\mathrm{N^4MLT}} = \int_{\ell_1,\ldots,\ell_L} \mathcal{A}^{(L)}_F(1,\ldots,L+1,12,123,234,J) \ . \tag{9.14}$$

La apertura dual de esta topología satisface una identidad de factorización en términos de topologías más simples, donde su representación diagramática se muesta en la Fig. 9.3. El procedimiento y las expresiones explícitas de la apertura para cada uno de los canales, son presentados de manera detallada en el Capítulo 5.

Basados en el aprendizaje adquirido a través de los Capítulos 4 y 5, se tiene que la apertura dual obtenida al aplicar los residuos anidados, a través de la metodología LTD, permite escribir cualquier integral de lazo o amplitud de dispersión de una forma factorizada. De manera más específica, una topología N^{k}MLT se puede simplificar por medio de convoluciones de subtopologías N^{j}MLT y MLT (con $j < k$). Además, la estructura singular

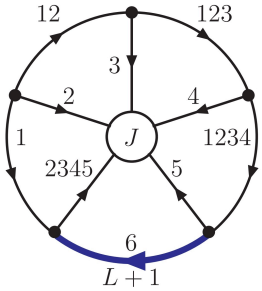

Figure 9.4: Representación diagramática de la topología universal N^{7}MLT. La corriente J considera todas las posibles combinaciones entre propagadores internos. La línea azul representa una inserción MLT con $L-5$ lazos y $L-4$ propagators.

de las topologías más complejas está condicionada por estas propiedades de factorización, lo que simplifica su tratamiento y cancelación.

Con estas propiedades en mente, en el Capítulo 6 se explora la aplicación del enfoque LTD para describir la familia de topologías que aparecen por primera vez a cinco lazos. Siguiendo las estrategias utilizadas en el análisis de las topologías de cuatro lazos, se define una *topología universal* N^{7}MLT que permita generar la representación LTD de cualquier posible diagrama de Feynman de cinco lazos o amplitud de dispersión. Aprovecha la formulación recursiva en términos de subtopologías más simples e inserciones MLT, con las cuales se extraen las principales características de los diagramas más complejos.

Las topologías representativas, en este caso son caracterizadas por un par de conjuntos de propagadores, los cuales surgen a partir de la interacción entre los conjuntos internos,

$$\{23, 24, 25, 34, 35, 45, 234, 235, 245, 345\} \ .$$

Inspirados en la *topología universal* N^{4}MLT [5], retomamos el concepto de corriente para codificar los conjuntos distintivos, como se representa diagramáticamente en la Fig. 9.4. El número total de pares distintivos es quince, y están convenientemente agrupados en cinco canales como se presenta en la Tabla 9.1. Cada par está asociado a un diagrama de Feynman en particular. El surgimiento de topologías no planares asciende a un número de diez respecto al total de quince. La representación general de la familia

J_1:	$\{234, 23\}$	$\{234, 24\}$ ⋆	$\{234, 34\}$
J_2:	$\{235, 23\}$ ⋆	$\{235, 25\}$ ⋆	$\{235, 35\}$ ⋆
J_3:	$\{245, 24\}$ ⋆	$\{245, 25\}$ ⋆	$\{245, 45\}$ ⋆
J_4:	$\{345, 34\}$	$\{345, 35\}$ ⋆	$\{345, 45\}$
J_5:	$\{23, 45\}$	$\{24, 35\}$ ⋆	$\{25, 34\}$ ⋆

Table 9.1: Conjunto de pares distintivos identificando las topologías representativas de la familia N^{7}MLT. La estrella indica que el conjunto está asociado a un diagrama noplanar.

N^{7}MLT se obtiene a través de la unión de los conjuntos presentados en la Tabla 6.1 en la corriente definida como J,

$$J = \cup_{i=1}^{5} J_i \ . \tag{9.15}$$

Este escenario permite ensamblar la representación de Feynman de la familia N^{7}MLT como

$$\mathcal{A}^{(L)}_{\mathrm{N^7MLT}} = \int_{\ell_1,\ldots,\ell_L} \mathcal{A}^{(L)}_{F}(1, \ldots, L+1, 12, 123, 1234, 2345, J) \ . \tag{9.16}$$

El análisis de apertura desarrollado en el Capítulo 6, confirma que la representación LTD de la Ec. (9.16) se expresa de manera factorizada en términos de convoluciones de subtopologías conocidas, abriendo cualqier topología multilazo N^{7}MLT a árboles conectados, además, la expresión es válida para todas las configuraciones N^{k-1}MLT con $k \leq 7$.

9.4 Representación causal

Sabemos que para cualquier integral o amplitud de dispersión con lazos, el surgimiento de una expresión causal se alcanza después de sumar todos los residuos anidados, sin embargo, debemos ser conscientes que el numerador del integrando puede resultar ser un polinomio de gran longitud, el cual depende de las energías sobre la capa de masas y las energías externas.

La estrategia introducida en Ref. [113] e implementada en el Capítulo 5 para derivar una representación causal más manejable, fue reinterpretar la expresión causal encontrada en términos de umbrales entrelazados, obte-

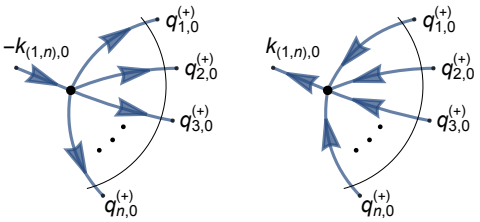

Figure 9.5: Interpretación gráfica de las configuraciones causales codificadas por $\lambda^{+}_{(1,n)}$ (izquierda) y $\lambda^{-}_{(1,n)}$ (derecha). Cuando el momento externo es saliente, $k_{(1,n),0} > 0$, aparece una singularidad de umbral cuando todos los momentos internos están en su capa de masas y los trimomentos direccionados hacia el vértice de interacción. La configuración opuesta, $\lambda^{+}_{(1,n)}$, genera una singularidad de umbral si $k_{(1,n),0} < 0$ (momento externo entrante).

niendo la siguiente representación causal general de LTD

$$\mathcal{A}_D^{(L)} = \int_{\vec{\ell}_1 \dots \vec{\ell}_L} \frac{1}{x_n} \sum_{\sigma \in \Sigma} \frac{\mathcal{N}_{\sigma(i_1,\dots,i_{n-L})}}{\lambda_{\sigma(i_1)}^{h_{\sigma(i_1)}} \cdots \lambda_{\sigma(i_{n-L})}^{h_{\sigma(i_{n+L})}}} + (\lambda_p^+ \leftrightarrow \lambda_p^-) \ , \tag{9.17}$$

con $x_n = \prod_{i=1}^{n} 2q_{i,0}^{(+)}$. Los propagadores de Feynman de la Ec. (9.5) son sustituidos en la Ec. (9.17) por propagadores causales $1/\lambda_p^{\pm}$ con

$$\lambda_p^{\pm} = \sum_{i \in p} q_{i,0}^{(+)} \pm k_{p,0} \ , \tag{9.18}$$

donde p es una partición de las energías sobre la capa de masas, y $k_{p,0}$ es combinación lineal de las componentes de energía de los momentos externos. Los propagadores causales pueden aparecer elevados a una potencia si los propagadores de Feynman en la representación original están elevados a una potencia, por ejemplo, debido a la presencia de una autoenergía. Cada $\lambda_p^{\pm}$ está asociado a una configuración cinemática, en la cual el flujo de momento de todos los propagadores contenidos en la partición p están alineados en la misma direción. En la Fig. 9.5 se muestra una interpretación gráfica. Cualquier otra configuración no puede ser interpretada como causal y no está considerada en Ec. (9.17). Dependiendo del signo de $k_{p,0}$, ya sea λ_p^+ o λ_p^- se vuelven singulares cuando todos los propagadores en p se asignan sobre la capa de masas.

El conjunto Σ en Ec. (9.17) contiene todas las combinaciones de propa-

gadores causales que se encuentran entrelazados, es decir, aquellas combinaciones cuyos flujos de momentos son compatibles entre ellas y así pues representan umbrales causales que pueden ocurrir simultaneamente. Cada elemento en Σ fija los flujos de momentos para todos los conjuntos en direcciones específicas. Sucesivamente, una vez que los flujos de momentos hayan sido fijados, la representación causal en Ec. (9.17) puede ser establecida.

La metodología descrita anteriormente, se aplica para extraer la representación causal LTD de una selección de topologías a cuatro lazos. En el Capítulo 5, explícitamente se trabaja con las configuraciones N^3MLT con un propagador por línea y cinco partículas externas; además de los canales t, s y u de la topología universal N^4MLT con un propagador por línea y seis partículas externas. Las expresiones derivadas están escritas exclusivamente en términos de propagadores causales [113], logrando así, en cada una de las configuraciones consideradas, la ausencia explícita de singularidades no causales en la representación LTD.

Para obtener la representación causal LTD con la estructura correspondiente a la Ec. (9.17), es crucial superar una dificulatad importante: la determinación de los umbrales causales de las integrales multilazo de Feynman a partir de la identificación de todas las configuraciones internas que cumplen las condiciones causales. Con el objetivo de plantear un algoritmo más eficiente, en la siguiente sección se presenta un método alternativo, basado en computación cuántica, para la búsqueda de las configuraciones singulares causales de diagramas de Feynman con lazos múltiples.

Antes de continuar, recordemos los conceptos de aristas y eloops [157, 158]. Las aristas se definen como la unión de un número arbitrario de propagadores, que conectan dos vértices de interacción. El algoritmo y la implementación se presentan en términos de eloops (lazos formados por aristas), dado que en un escenario de causalidad las configuraciones singulares causales sólo contemplan el escenario, donde el flujo de momento de todos los propagadores en una arista están alineados en la misma dirección.

9.5 Algoritmo cuántico para integrales de Feynman con lazos

Los algoritmos cuánticos [119] son considerados en la actualidad una alternativa muy prometedora para resolver aquellos problemas que resultan demasiado complejos, o incluso intratables, para los ordenadores clásicos debido a que escalan de forma exponencial o superpolinómica. De manera especial, se espera obtener ventaja en cuestión de velocidad sobre los algoritmos clásicos equivalentes cuando el escenario analizado incluye problemas en los que los principios cuánticos de superposición y entrelazamiento pueden ser explotados. Se trata, por ejemplo, de los casos bien estudiados de búsqueda en bases de datos [120] y de factorización de números enteros en términos de números primos [121]. Otras aplicaciones recientes, están relacionadas con la eficiencia y capacidades de los sistemas cuánticos para minimizar Hamiltonianos [122, 123], conduciendo así a una amplia gama de aplicaciones en problemas de optimización. Por ejemplo, en química cuántica [124], en física nuclear [125, 126], e inclusive en finanzas, donde la optimización de carteras de valores [127] es la aplicación de referencia.

En el área de física de partículas, los algoritmos cuánticos han empezado a ser objeto de atención, considerándolos como una alternativa prometedora para la solución de una amplia variedad de problemas. Algunas aplicaciones son: la aceleración de los algoritmos de clusterización de jets [128–131], el estudio de las propiedades de jets en un medio [132, 133], la determinación de las densidades de partones [134], la simulación de cascadas de partones [135–137], colisiones de iones pesados [137], aprendizaje automático cuántico [138–140] y teorías gauge en el retículo [141–146].

A pesar de recientes propuestas relacionadas con la evaluación numérica de amplitudes de helicidad [147] y de secciones eficaces [148] a nivel de árbol, se asume de forma generalizada que la descripción perturbativa de los procesos de dispersión a altas energías está fuera del alcance de los ordenadores cuánticos, ya que requeriría un número prohibitivo de qubits. En esta sección se presentan dos algoritmos cuánticos aplicados a la teoría cuántica de campos perturbativos, aprovechando las propiedades causales de las integrales de Feynman con lazos en la representación LTD, para establecer que un enfoque de computación cuántica es completamente apropiado.

La viabilidad de asociación entre la computación cuántica y las integrales de

Feynman con lazos se debe a que los dos estados de un propagador de Feynman sobre la capa de masas pueden codificarse en un qubit. En concreto, el problema que abordamos es la extracción de la representación causal de las integrales de Feynman multilazo en el formalismo de la Dualidad Lazo-Árbol, a partir de la identificación de todas las configuraciones internas que cumplen las condiciones de causalidad entre las $N = 2^n$ posibles soluciones, donde n es el número de propagadores de Feynman internos. Como se mostrará, este es un problema de satisfabilidad que puede ser resuelto con una modificación bien diseñada del algoritmo de Grover [120].

La situación más común en la que se emplea este algoritmo consiste en encontrar una única solución entre un gran conjunto no estructurado de N configuraciones. Mientras que un algoritmo clásico requiere probar la condición de satisfacción para todos los casos, es decir, $\mathcal{O}(N)$ iteraciones, el algoritmo cuántico considera todos los estados posibles en una superposición uniforme, y prueba la condición de satisfacción en un sólo intento. Finalmente, la complejidad del algoritmo pasa de $\mathcal{O}(N)$ en el caso clásico, a $\mathcal{O}(\sqrt{N})$ en el caso cuántico. Esto constituye una gran motivación para explorar la aplicabilidad de los algoritmos de búsqueda en el cálculo de diagramas e integrales de Feynman.

El algoritmo estándar de búsqueda de Grover [120] sobre bases de datos no estructuradas se basa en tres conceptos fundamentales: la superposición uniforme de todos los estados posibles, un operador de oráculo para marcar los estados de interés y un operador de difusión para amplificar la probabilidad de estos elementos.

i) La superposición uniforme del total de $N = 2^n$ estados se denota como

$$|q\rangle = \frac{1}{\sqrt{N}} \sum_{x=0}^{N-1} |x\rangle \ , \tag{9.19}$$

donde n es el número de aristas o propagadores del diagrama de Feynman. La Ec. 9.19 puede ser entendida y escrita como la superposición de dos estados, el estado ganador $|w\rangle$ y el estado ortogonal $|q_\perp\rangle$,

$$|q\rangle = \cos\theta\,|q_\perp\rangle + \sin\theta\,|w\rangle \ . \tag{9.20}$$

El estado $|w\rangle$ codifica todas las soluciones causales en superposición,

mientras que el estado $|q_\perp\rangle$ representa todas las soluciones ortogonales,

$$|w\rangle = \frac{1}{\sqrt{r}} \sum_{x \in w} |x\rangle \ , \qquad |q_\perp\rangle = \frac{1}{\sqrt{N-r}} \sum_{x \notin w} |x\rangle \ , \tag{9.21}$$

con r el número de soluciones causales, y N el número total de configuraciones posibles. El ángulo de mezcla está dado por

$$\theta = \arcsin \sqrt{r/N} \ , \tag{9.22}$$

midiendo así la proporción de estados a consultar.

ii) El operador del oráculo dado por

$$U_w = \boldsymbol{I} - 2|w\rangle\langle w| \ , \tag{9.23}$$

invierte el estado $|x\rangle$ si $x \in w$, $U_w|x\rangle = -|x\rangle$, y lo deja sin modificaciones en otro caso, $U_w|x\rangle = |x\rangle$ si $x \notin w$.

iii) El operador de difusión expresado como

$$U_q = 2|q\rangle\langle q| - \boldsymbol{I} \ , \tag{9.24}$$

realiza una reflexión alrededor del estado inicial $|q\rangle$, para amplificar la probabilidad de las configuraciones singulares causales.

En función del problema de interés, se define si es necesaria la aplicación de los operadores de oráculo y difusión repetidamente. La aplicación iterativa de ambos operadores t veces conduce a

$$(U_q U_w)^t |q\rangle = \cos\theta_t \, |q_\perp\rangle + \sin\theta_t \, |w\rangle \ , \tag{9.25}$$

donde $\theta_t = (2t+1)\,\theta$.

El ángulo de mezcla juega un papel crítico para definir un número adecuado de iteraciones, θ_t tiene que ser elegido de acuerdo a la siguiente condición:

$$\frac{\cos^2\theta_t}{N-r} \ll \frac{\sin^2\theta_t}{r} \ . \tag{9.26}$$

El objetivo general es obtener un estado final de tal forma, que la probabilidad de cada uno de los componentes en el estado ortogonal sea mucho menor que la probabilidad de cada una de las soluciones causales, el cual

se obtiene cuando $\sin^2\theta_t \sim 1$. Dada la relación en Ec. (9.26), el algoritmo cuántico de Grover muestra un desempeño óptimo cuando θ es menor o similar a $\pi/6$, equivalente a tener r menor o similar a $N/4$. En el caso de ángulos mucho mayores, la amplificación de la probabilidad de amplitud de los estados ganadores es inadecuada.

Considerando las características de nuestro problema, sabemos por el cálculo clásico [5, 113] que el número de estados causales asociado a las topologías multilazo mostradas en la Fig. 7.2, es considerablemente mayor que $N/4$. Para ajustar el escenario, se proponen dos estrategias para la modificación del algoritmo cuántico de Grover con el fin de lograr su viabilidad. Una de las estrategias opcionales, que también es válida para otros problemas en los que el número de soluciones es mayor que $N/4$, es ampliar el número total de estados sin aumentar el número de soluciones, introduciendo qubits auxiliares en el registro que codifica las aristas del diagrama del lazo[1]. En general, el número máximo de qubits auxiliares necesarios es dos, ya que esto aumenta el número de estados totales en un factor 4.

En particular, para los diagramas de Feynman con lazos tenemos una ventaja importante; el hecho de que dada una solución causal (equivalente en teoría de grafos a una configuración acíclica orientada), el estado espejo en el que se invierten todos los flujos de momento internos es también una solución causal. Por lo tanto, la estrategia más eficiente consiste en fijar una de las aristas y considerar que sólo uno de sus estados contribuye al conjunto ganador. Los estados espejo se deducen directamente de las soluciones causales seleccionadas. Como resultado, el conjunto completo de soluciones causales puede determinarse con la ayuda de a lo más un qubit auxiliar.

Antes de continuar, recordemos el concepto de profundidad[2] de un circuito cuántico usado para codificar un algoritmo cuántico. Éste proporciona el número de puertas lógicas que deben ejecutarse a lo largo del camino más largo del circuito, desde la entrada hasta la salida, avanzando en el tiempo a lo largo de los cables de los qubits, representando una estimación de la eficiencia de un circuito cuántico. La entrada se entiende como la preparación de los qubits y la salida como la puerta de medición. En la implementación que se presentará, la profundidad del circuito cuántico se cálcula a través

[1] Esta estrategia ha sido discutida previamente en la Ref. [160].
[2] https://quantumcomputing.stackexchange.com

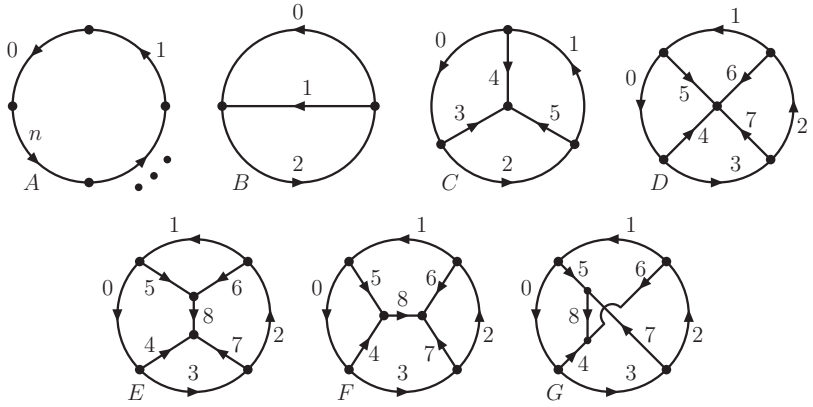

Figure 9.6: Topologías multilazo representativas con, hasta cuatro lazos. La dirección de las flechas corresponde a los estados $|1\rangle$. Los vértices pueden tener o no momentos externos adjuntos. Más allá de un lazo, cada línea puede estar compuesta por aristas n_i que introducen vértices adicionales. De izquierda a derecha y de arriba abajo: un lazo con n vértices, dos lazos (MLT), tres lazos (N^2MLT), cuatro lazos con un vértice de cuatro partículas (N^3MLT), y cuatro lazos con interacciones trivalentes (N^4MLT), canales t, s y u.

de `QuantumCircuit.depth()`[1], una rutina proporcionada por Qiskit. Una característica importante de la profundidad del circuito cuántico es el impacto de las puertas cuánticas que actúan en qubits no comunes, lo que permite realizarlas en el mismo paso. Por otro lado, si las puertas actúan en al menos un qubit en común, tienen que ser aplicadas en diferentes pasos, aumentando la profundidad del circuito cuántico.

9.5.1 Algoritmo cuántico para la búsqueda causal

Continuando con la implementación del algoritmo, la adaptación del algoritmo cuántico de Grover requiere tres registros, junto con un qubit adicional utilizado como marcador por el oráculo de Grover. El primer registro, cuyos qubits se etiquetan como q_i, codifica los estados de las aristas. El qubit q_i está en el estado $|1\rangle$ si el flujo de momento de la arista correspondiente está orientado en la dirección de la asignación inicial (ver Fig. 9.6) y en $|0\rangle$ si está en la dirección contraria. En cualquier caso, el resultado físico final es independiente de la asignación inicial, utilizándose únicamente como refer-

[1] https://qiskit-test.readthedocs.io

encia.

El segundo registro, llamado c_{ij}, almacena las cláusulas Booleanas que prueban si dos qubits que representan dos aristas adyacentes están o no en el mismo estado (si sus momentos están orientados en la misma dirección). Estas cláusulas binarias se definen como

$$\begin{aligned} c_{ij} &\equiv (q_i = q_j) \ , \\ \bar{c}_{ij} &\equiv (q_i \neq q_j) \ , \qquad i,j \in \{0,\ldots,n-1\} \ . \end{aligned} \tag{9.27}$$

El tercer registro, $a_k(\{c_{ij}\},\{\bar{c}_{ij}\})$, codifica las cláusulas de lazo que prueban si todos los qubits (aristas) de cada uno de los lazos que forman parte del diagrama generan un circuito cíclico.

La implentación del algoritmo cuántico causal se describe a continuación. La superposición uniforme inicial se obtiene aplicando puertas Hadamard a cada uno de los qubits en el registro q, $|q\rangle = H^{\otimes n}|0\rangle$, mientras que el qubit que se utiliza como marcador de Grover se inicializa con

$$|out_0\rangle = \frac{|0\rangle - |1\rangle}{\sqrt{2}} \equiv |-\rangle \, , \tag{9.28}$$

correspondiente al estado de Bell en la base $\{|0\rangle,|1\rangle\}$. Los otros registros, $|c\rangle$ and $|a\rangle$, usados para almacenar las cláusulas binarias y las cláusulas de lazo, son inicializados en $|0\rangle$. Cada cláusula binaria $\bar{c}_{ij}$ requiere dos puertas CNOT que operan entre dos qubits en el registro $|q\rangle$ y un qubit en el registro $|c\rangle$. Una puerta XNOT adicional que actúa sobre el qubit correspondiente en $|c\rangle$ para implementar una cláusula binaria c_{ij}.

El oráculo es definido como

$$U_w|q\rangle|c\rangle|a\rangle|out_0\rangle = (-1)^{f(a,q)}\,|q\rangle|c\rangle|a\rangle|out_0\rangle \ , \tag{9.29}$$

por tanto, si se cumplen todas las condiciones causales, $f(a,q) = 1$, los estados correspondientes se marcan; en caso contrario, si $f(a,q) = 0$, se mantienen sin cambios. Después del marcado, los registros $|c\rangle$ y $|a\rangle$ se reestablecen a $|0\rangle$ aplicando las operaciones del oráculo en orden inverso. A continuación, el difusor U_q se aplica al registro $|q\rangle$, siendo éste el descrito en el sitio web de IBM Qiskit[1].

[1] `http://qiskit.org/`

Se emplean dos simuladores cuántico diferentes: *IBM Quantum* proporcionado por el recurso de código abierto Qiskit; and *Quantum Testbed* (QUTE) [161], un simulador cuántico de alto rendimiento desarrollado y mantenido por la Fundación Centro Tecnológico de la Información y la Comunicación (CTIC)[1].

El resultado del algoritmo de Grover descrito anteriormente, es un estado cuántico que es predominantemente una superposición de todo el conjunto de soluciones causales, con una pequeña contribución de los estados ortogonales. Tras una medición, se determina una única configuración y se pierde la superposición. Si se requiere conocer todas las soluciones y no sólo una, la salida original del algoritmo de Grover tiene entonces que prepararse y medirse un cierto número de veces, también llamadas disparos, lo suficientemente numeroso como para escanear todas las soluciones causales, y distinguirlas de los estados no causales menos probables.

El resultado final se representa mediante histogramas de frecuencia y se ve afectado por las fluctuaciones estadísticas inherentes a las mediciones de un sistema cuántico. Estimamos que el número de disparos necesarios para distinguir las configuraciones causales de las no causales con una significancia estadística de $\Delta\sigma$ desviaciones estándar en un simulador cuántico viene dado por

$$N_{\text{shots}} \approx r\,(\Delta\sigma)^2\left(1+\mathcal{O}(\cos^2(\theta_t))\right)\,, \tag{9.30}$$

obteniendo una amplificación eficiente de los estados causales, es decir, $\cos(\theta_t) \sim 0$. A continuación, consideraremos $\Delta\sigma \gtrsim 3$, que proporciona un rendimiento discriminante suficientemente fiable con un número mínimo de disparos.

La implementación del algoritmo se realiza explícitamente para las topologías multilazo mostradas en la Fig. 9.6, considerando un propagador por arista. A pesar de la complejidad de estas topologías, el algoritmo cuántico está bien sustentado, ya sea por la capacidad del simulador cuántico de IBM o de QUTE Testbed, logrando así identificar de manera eficiente todas las configuraciones causales asociadas a cada una de las topologás implementadas.

[1] `http://qute.ctic.es/`

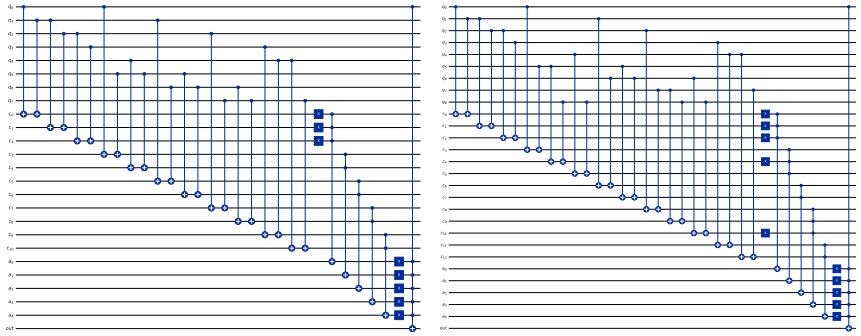

(a) N^3MLT (b) Canal t

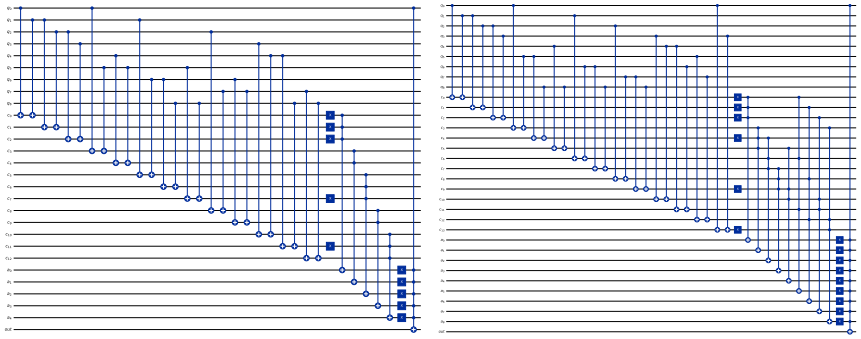

(c) Canal s (d) Canal u

Figure 9.7: Oráculos de los circuitos cuánticos de las topologías a cuatro lazos (omitiendo la reflexión de las puertas cuánticas): (a) N^3MLT, (b) canal t, (c) canal s y (d) canal u del N^4MLT.

Por ejemplo, en relación a las topologías con mayor complejidad, los oráculos del circuito cuántico asociados a la topología N^3MLT y a los canales t, s y u de la topología N^4MLT se muestran en la Fig. 9.7. Cada una de estas topologías, con excepción del canal u, fue implementada con el simulador cuántico de IBM, obteniendo como resultado las primeras tres salidas mostradas en la Fig. 9.8, la distribución de probabilidades de estados causales y no causales. En el caso del canal u, el requerimiento de implementación en términos de número de quibits es de 33, lo cual está fuera de las capacidades de Qiskit.

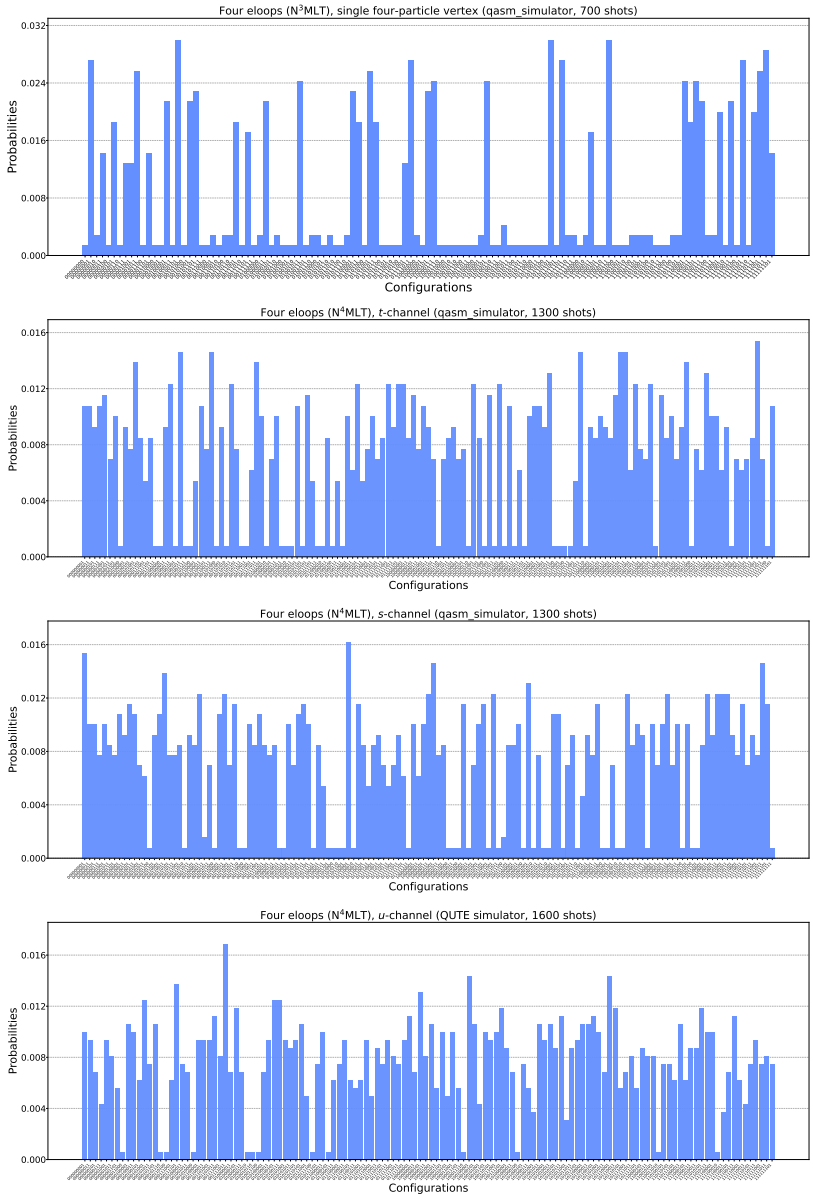

Figure 9.8: Distribución de probabilidades de configuraciones causales y no causales para las topologías a cuatro lazos después de 700, 1300, 1300 and 1600 disparos, respectivamente. Se utilizaron los simuladores *qasm_simulator* de IBM y QUTE Testbed para el canal u. De arriba a abajo: N^3MLT, canales t, s and u del N^4MLT con $n_i = 1$. El número de estados seleccionados es 39/256, 102/512, 102/512 y 115/512, respectivamente.

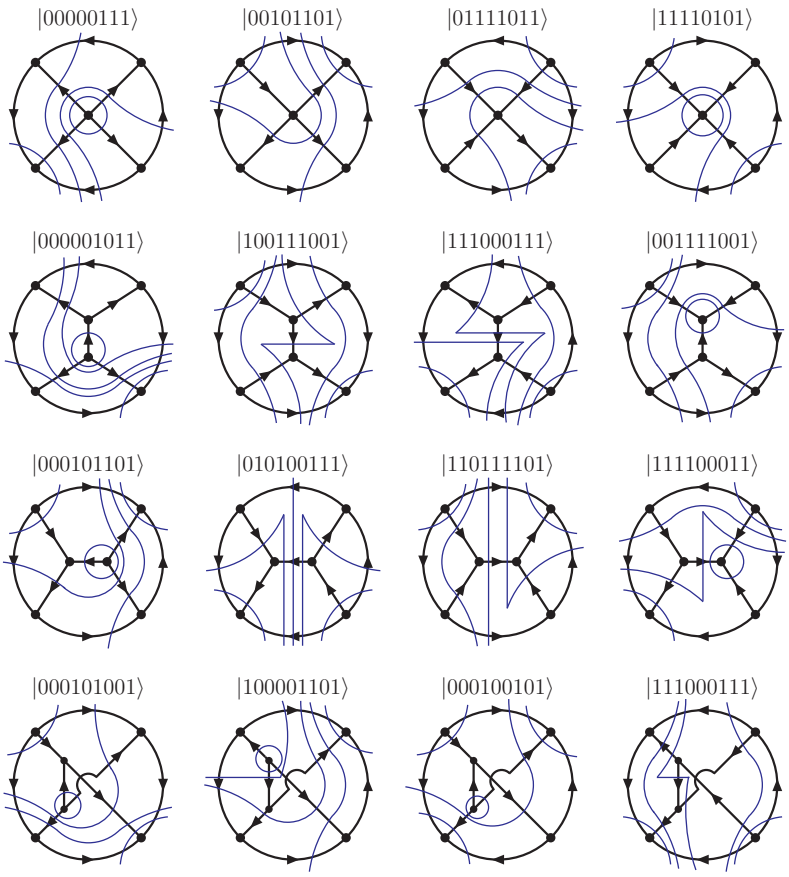

Figure 9.9: Diagramas representativos de umbrales entrelazados a cuatro eloops, asociados a la salida del algoritmo cuántico mostrado en la Fig. 9.8.

La implementación del canal u se realizó con el simulador QUTE Testbed, el cual acepta más de 32 qubits, teniendo como resultado la distribución de probabilidades causales y no causales mostrada en la gráfica inferior de la Fig. 9.8.

La interpretación diagramática de la distribución de probabilidades causales y no causales, se realiza mediante diagramas con umbrales entrelazados. En la Fig. 9.9 se muestra una selección de diagramas con umbrales entrelazados representativos, asociados a las salidas mostradas en la Fig. 9.8.

9.6 Conclusiones

La evolución de la metodología LTD ha experimentado mejoras sumamente importantes en los últimos años. Una nueva estrategia basada en la aplicación de residuos anidados, para abrir cualquier amplitud de dispersión multilazo a árboles conectados, permitió reformular la Dualidad Lazo-Árbol a todos los órdenes perturbativos. El desarrollo para lograr esta reformulación se presenta en el Capítulo 4, considerando una selección de topologías multilazo con $L + 3$ conjuntos de propagadores. La representación LTD se logra expresar analíticamente de forma muy compacta, y factorizada en términos de subtopologías más simples. Dado que esta estructura factorizada viene impuesta por la apertura en árboles conectados y por causalidad, se espera que este comportamiento se mantenga a todos los órdenes y topologías. Es de destacar que las expresiones duales presentadas están libres de singularidades no físicas y son independientes del flujo de momentos inicial. Esta propiedad se ha probado con todas las topologías y varias configuraciones internas. También conjeturamos que las representaciones duales analíticas en términos de sólo denominadores causales son siempre posibles.

Los resultados encontrados en el Capítulo 4 se han extendido al análisis de las topologías multilazo que aparecen por primera vez a cuatro lazos en el Capítulo 5. Se encontró que esta familia puede ser representada por tres topologías principales, además, estas fueron unificadas en una única representación, la *topología universal* N^4MLT. Hemos descrito su apertura en términos de árboles conectados mediante la Dualidad Lazo-Árbol. Como esperábamos, la apertura admite una interpretación factorizada muy estructurada y compacta en términos de convoluciones de subtopologías conocidas, que finalmente determinan la estructura causal interna de toda la amplitud. La representación LTD presentada es válida en sistemas de coordenadas y dimensiones espacio-temporales arbitrarias.

La topología N^4MLT es llamada universal porque unifica en una sola expresión todos los ingredientes necesarios para abrir cualquier amplitud de dispersión de hasta cuatro lazos. En relación a la causalidad, hemos comprobado que la representación LTD de N^4MLT es causal, es decir, que la expresión analítica LTD es manifiestamente libre de singularidades no causales. Además, las ideas y resultados del análisis causal de la Ref. [113] se amplían en un orden perturbativo, se encuentra explícitamente la rep-

resentación causal LTD y se reinterpreta en términos de umbrales causales entrelazados, para la topología N^3MLT y los canales t, s y u de la topología N^4MLT. Hemos demostrado un comportamiento de estabilidad numérica deseado a nivel integrando a partir del análisis de una expresión causal explícita de LTD. El escenario causal permite trabajar con condiciones favorables, la ausencia de singularidades no causales permite obtener una evaluación numérica de las amplitudes de dispersión multilazo más eficiente. Además, todos estos resultados confirman la conjetura a todos los órdenes de la Ref. [6].

Más allá de cuatro lazos, la metodología presentada en el Capítulo 5 se utilizó como guía para lograr una descripción detallada de las topologías que surgen por primera vez a cinco lazos. En el Capítulo 6 se encuentra la expresión factorizada de la apertura dual de aquellas topologías que aparecen por primera vez a cinco lazos, la cual es suficiente para describir cualquier amplitud de dispersión hasta cinco lazos. De manera general, la reformulación de la metodología LTD presentada a lo largo de los Capítulos 4, 5 and 6, permite una aplicación directa y eficiente a los procesos físicos de dispersión, y también es ventajosa para descubrir aspectos formales de las amplitudes de dispersión multilazo.

Profundizando en el escenario de la representación causal, se presentó en el Capítulo 7 una propuesta para la solución a un ejercicio desafiante en órdenes superiores, la búsqueda de todas las configuraciones causales internas entre las 2^n soluciones potenciales, donde n es el número de aristas. Para abordar este problema, exploramos metodologías alternativas mediante un enfoque de computación cuántica. Hemos presentado la primera prueba de concepto de un algoritmo cuántico para reconstruir eficientemente integrales de Feynman multilazo explotando la Dualidad Lazo-Árbol y la causalidad. El problema concreto que se abordó, fue la identificación de todas las configuraciones singulares causales del integrando resultante de establecer propagadores internos de Feynman sobre su capa de masas. Esta información es útil tanto para identificar las discontinuidades físicas de la integral de Feynman con lazos, como para hacer una reconstrucción de su representación causal en la Dualidad Lazo-Árbol.

Hemos propuesto una modificación del algoritmo cuántico de Grover, el cual hemos descrito en términos generales y proporcionado detalles específicos sobre su aplicación a una selección de configuraciones multilazo. Estos ca-

sos fueron exitósamente implementados en los simuladores cuánticos de IBM Quantum y QUTE Testbed. Dada la profundidad cuántica del algoritmo, su ejecución en dispositivos reales conduce a resultados poco fiables debido a las limitaciones acuales del hardware. Sin embargo, los simuladores cuánticos identifican con éxito todos los estados causales, incluso para las configuraciones multilazo más complejas consideradas. Dados los constantes avances que se están produciendo en este campo, se espera que pronto se superen las actuales limitaciones tecnológicas.

Los conocimientos y la experiencia adquiridos a través de los desarrollos presentados en esta tesis, han ido preparando el camino para retomar el algoritmo FDU, un método desarrollado para construir una representación puramente cuatridimensional de las contribuciones perturbativas de orden superior a las secciones eficaces y tasas de desintegración físicas, esta vez, convenientemente a través de un escenario causal. Este es un trabajo en curso que implica la identificación de mapeos adecuados entre los momentos externos y de lazo de las amplitudes de dispersión virtuales, y los momentos externos de las contribuciones de emisión reales a través de la Dualidad Lazo-Árbol en su versión explícitamente causal. Para lograr la cancelación de las divergencias infrarrojas localmente sin introducir contra-términos de sustracción, se tomará ventaja de las representación causal de las contribuciones virtuales y reales, con el fin de realizar la suma sobre los estados infrarrojos degenerados a nivel del integrando.

Bibliography

[1] S. Ramírez-Uribe, R. J. Hernández-Pinto, G. Rodrigo and G. F. R. Sborlini, *From five-loop scattering amplitudes to open trees with the loop-tree duality*, *Symmetry* **14** (2022) .

[2] G. Clemente, A. Crippa, K. Jansen, S. Ramírez-Uribe, A. E. Rentería-Olivo, G. Rodrigo et al., *Variational quantum eigensolver for causal loop Feynman diagrams and acyclic directed graphs*, 2210.13240.

[3] S. Ramírez-Uribe, A. E. Rentería-Olivo, G. Rodrigo, G. F. R. Sborlini and L. Vale Silva, *Quantum algorithm for Feynman loop integrals*, *JHEP* **05** (2022) 100, [2105.08703].

[4] J. de Jesús Aguilera-Verdugo et al., *A Stroll through the Loop-Tree Duality*, *Symmetry* **13** (2021) 1029, [2104.14621].

[5] S. Ramírez-Uribe, R. J. Hernández-Pinto, G. Rodrigo, G. F. R. Sborlini and W. J. Torres Bobadilla, *Universal opening of four-loop scattering amplitudes to trees*, *JHEP* **04** (2021) 129, [2006.13818].

[6] J. J. Aguilera-Verdugo, F. Driencourt-Mangin, R. J. Hernández-Pinto, J. Plenter, S. Ramirez-Uribe, A. E. Renteria Olivo et al., *Open Loop Amplitudes and Causality to All Orders and Powers from the Loop-Tree Duality*, *Phys. Rev. Lett.* **124** (2020) 211602, [2001.03564].

[7] J. J. Aguilera-Verdugo, F. Driencourt-Mangin, J. Plenter, S. Ramírez-Uribe, G. Rodrigo, G. F. R. Sborlini et al., *Causality, unitarity thresholds, anomalous thresholds and infrared singularities from the loop-tree duality at higher orders*, *JHEP* **12** (2019) 163, [1904.08389].

[8] FCC collaboration, A. Abada et al., *HE-LHC: The High-Energy Large Hadron Collider: Future Circular Collider Conceptual Design Report Volume 4*, *Eur. Phys. J. ST* **228** (2019) 1109–1382.

[9] FCC collaboration, A. Abada et al., *FCC-hh: The Hadron Collider: Future Circular Collider Conceptual Design Report Volume 3*, *Eur. Phys. J. ST* **228** (2019) 755–1107.

[10] FCC collaboration, A. Abada et al., *FCC-ee: The Lepton Collider: Future Circular Collider Conceptual Design Report Volume 2*, *Eur. Phys. J. ST* **228** (2019) 261–623.

[11] FCC collaboration, A. Abada et al., *FCC Physics Opportunities: Future Circular Collider Conceptual Design Report Volume 1*, *Eur. Phys. J. C* **79** (2019) 474.

[12] N. S. Ramírez Uribe, *Quantum algorithm for querying causality of multiloop scattering amplitudes*, *PoS* **ICHEP2022** (11, 2022) 418, [2211.05487].

[13] N. S. Ramírez Uribe, S. Ramírez-Uribe, R. J. Hernández-Pinto, A. E. Rentería-Olivo, G. Rodrigo, G. F. R. Sborlini et al., *Four-loop scattering amplitudes journey into the forest*, *PoS* **EPS-HEP2021** (2022) 732, [2110.10605].

[14] N. S. R. Uribe, *Four-loop scattering amplitudes through the loop-tree duality*, *Rev. Mex. Fis. Suppl.* **3** (2022) 020720, [2112.05584].

[15] S. Ramírez-Uribe, *From Causal Representation of Multiloop Scattering Amplitudes to Quantum Computing*, *Acta Phys. Polon. Supp.* **15** (2022) 1, [2201.04381].

[16] A. Blondel, J. Gluza, S. Jadach, P. Janot and T. Riemann, eds., *Theory for the FCC-ee: Report on the 11th FCC-ee Workshop Theory and Experiments*, vol. 3/2020 of *CERN Yellow Reports: Monographs*, (Geneva), CERN, 5, 2019. 10.23731/CYRM-2020-003.

[17] J. J. Aguilera-Verdugo, F. Driencourt-Mangin, J. Plenter, S. Ramírez-Uribe, G. Rodrigo, G. F. R. Sborlini et al., *Unsubtractions at NNLO*, *CERN Yellow Reports: Monographs* **3** (2020) 169–176.

[18] N. Selomit Ramírez-Uribe, R. J. Hernández-Pinto and G. Rodrigo, *QED and QCD self-energy corrections through the loop-tree duality*, *J. Phys. Conf. Ser.* **912** (2017) 012013, [1709.07802].

[19] R. K. Ellis et al., *Physics Briefing Book: Input for the European Strategy for Particle Physics Update 2020*, 1910.11775.

[20] F. Gianotti et al., *Physics potential and experimental challenges of the LHC luminosity upgrade*, *Eur. Phys. J. C* **39** (2005) 293–333, [hep-ph/0204087].

[21] P. Bambade et al., *The International Linear Collider: A Global Project*, 1903.01629.

[22] ILC collaboration, G. Aarons et al., *International Linear Collider Reference Design Report Volume 2: Physics at the ILC*, 0709.1893.

[23] CLIC, CLICdp collaboration, *The Compact Linear e^+e^- Collider (CLIC): Physics Potential*, 1812.07986.

[24] CEPC Study Group collaboration, M. Dong et al., *CEPC Conceptual Design Report: Volume 2 - Physics & Detector*, 1811.10545.

[25] G. Heinrich, *Collider Physics at the Precision Frontier*, *Phys. Rept.* **922** (2021) 1–69, [2009.00516].

[26] P. Ramond, *Journeys beyond the standard model*, vol. 101. 1999.

[27] J. Chadwick, *Possible Existence of a Neutron*, *Nature* **129** (1932) 312.

[28] P. A. M. Dirac, *A Theory of Electrons and Protons*, *Proc. Roy. Soc. Lond. A* **126** (1930) 360–365.

[29] E. Fermi, *Tentativo di una teoria dell'emissione dei raggi beta*, *Ric. Sci.* **4** (1933) 491–495.

[30] H. Yukawa, *On the Interaction of Elementary Particles I*, *Proc. Phys. Math. Soc. Jap.* **17** (1935) 48–57.

[31] J. C. Street and E. C. Stevenson, *New Evidence for the Existence of a Particle of Mass Intermediate Between the Proton and Electron*, *Phys. Rev.* **52** (1937) 1003–1004.

[32] F. J. Dyson, *The Radiation theories of Tomonaga, Schwinger, and Feynman*, *Phys. Rev.* **75** (1949) 486–502.

[33] G. D. Rochester and C. C. Butler, *Evidence for the Existence of New Unstable Elementary Particles*, *Nature* **160** (1947) 855–857.

[34] V. D. Hopper and S. Biswas, *Evidence concerning the existence of the new unstable elementary neutral particle*, *Phys. Rev.* **80** (Dec, 1950) 1099–1100.

[35] M. Gell-Mann, *Isotopic Spin and New Unstable Particles*, *Phys. Rev.* **92** (1953) 833–834.

[36] C.-N. Yang and R. L. Mills, *Conservation of Isotopic Spin and Isotopic Gauge Invariance*, *Phys. Rev.* **96** (1954) 191–195.

[37] F. Reines and C. L. Cowan, *The neutrino*, *Nature* **178** (1956) 446–449.

[38] T. D. Lee and C.-N. Yang, *Question of Parity Conservation in Weak Interactions*, *Phys. Rev.* **104** (1956) 254–258.

[39] E. C. G. Sudarshan and R. e. Marshak, *Chirality invariance and the universal Fermi interaction*, *Phys. Rev.* **109** (1958) 1860–1860.

[40] R. P. Feynman and M. Gell-Mann, *Theory of Fermi interaction*, *Phys. Rev.* **109** (1958) 193–198.

[41] M. Gell-Mann and Y. Ne'eman, *Current-generated algebras*, *Annals Phys.* **30** (1964) 360–369.

[42] M. Gell-Mann, *A Schematic Model of Baryons and Mesons*, *Phys. Lett.* **8** (1964) 214–215.

[43] G. Zweig, *An SU(3) model for strong interaction symmetry and its breaking. Version 2*, pp. 22–101. 2, 1964.

[44] J. D. Bjorken and S. L. Glashow, *Elementary Particles and SU(4)*, *Phys. Lett.* **11** (1964) 255–257.

[45] J. S. Schwinger, *A Theory of the Fundamental Interactions*, *Annals Phys.* **2** (1957) 407–434.

[46] S. L. Glashow, *Partial Symmetries of Weak Interactions*, *Nucl. Phys.* **22** (1961) 579–588.

[47] A. Salam and J. C. Ward, *Electromagnetic and weak interactions*, *Phys. Lett.* **13** (1964) 168–171.

[48] S. Weinberg, *A Model of Leptons*, *Phys. Rev. Lett.* **19** (1967) 1264–1266.

[49] G. Danby, J. M. Gaillard, K. A. Goulianos, L. M. Lederman, N. B. Mistry, M. Schwartz et al., *Observation of High-Energy Neutrino Reactions and the Existence of Two Kinds of Neutrinos*, *Phys. Rev. Lett.* **9** (1962) 36–44.

[50] J. H. Christenson, J. W. Cronin, V. L. Fitch and R. Turlay, *Evidence for the* 2π *Decay of the* K_2^0 *Meson*, *Phys. Rev. Lett.* **13** (1964) 138–140.

[51] J. D. Bjorken, *Asymptotic Sum Rules at Infinite Momentum*, *Phys. Rev.* **179** (1969) 1547–1553.

[52] S. L. Glashow, J. Iliopoulos and L. Maiani, *Weak Interactions with Lepton-Hadron Symmetry*, *Phys. Rev. D* **2** (1970) 1285–1292.

[53] G. 't Hooft, *Renormalizable Lagrangians for Massive Yang-Mills Fields*, *Nucl. Phys. B* **35** (1971) 167–188.

[54] H. Fritzsch and M. Gell-Mann, *Current algebra: Quarks and what else?*, *eConf* **C720906V2** (1972) 135–165, [hep-ph/0208010].

[55] H. Fritzsch, M. Gell-Mann and H. Leutwyler, *Advantages of the Color Octet Gluon Picture*, *Phys. Lett. B* **47** (1973) 365–368.

[56] D. J. Gross and F. Wilczek, *Ultraviolet Behavior of Nonabelian Gauge Theories*, *Phys. Rev. Lett.* **30** (1973) 1343–1346.

[57] H. D. Politzer, *Reliable Perturbative Results for Strong Interactions?*, *Phys. Rev. Lett.* **30** (1973) 1346–1349.

[58] M. Kobayashi and T. Maskawa, *CP Violation in the Renormalizable Theory of Weak Interaction*, *Prog. Theor. Phys.* **49** (1973) 652–657.

[59] Gargamelle Neutrino collaboration, F. J. Hasert et al., *Observation of Neutrino Like Interactions Without Muon Or Electron in the Gargamelle Neutrino Experiment*, *Phys. Lett. B* **46** (1973) 138–140.

[60] M. L. Perl, *The Discovery of The Tau Lepton*, *NATO Sci. Ser. B* **352** (1996) 277–302.

[61] C. Y. Prescott et al., *Parity Nonconservation in Inelastic Electron Scattering*, *Phys. Lett. B* **77** (1978) 347–352.

[62] C. Y. Prescott et al., *Further Measurements of Parity Nonconservation in Inelastic electron Scattering*, *Phys. Lett. B* **84** (1979) 524–528.

[63] UA1 collaboration, G. Arnison et al., *Experimental Observation of Isolated Large Transverse Energy Electrons with Associated Missing Energy at* $\sqrt{s} = 540$ *GeV*, *Phys. Lett. B* **122** (1983) 103–116.

[64] UA1 collaboration, G. Arnison et al., *Experimental Observation of Lepton Pairs of Invariant Mass Around 95-GeV/c**2 at the CERN SPS Collider*, *Phys. Lett. B* **126** (1983) 398–410.

[65] CDF collaboration, F. Abe et al., *Observation of top quark production in* $\bar{p}p$ *collisions*, *Phys. Rev. Lett.* **74** (1995) 2626–2631, [hep-ex/9503002].

[66] D0 collaboration, S. Abachi et al., *Observation of the top quark*, *Phys. Rev. Lett.* **74** (1995) 2632–2637, [hep-ex/9503003].

[67] DONUT collaboration, K. Kodama et al., *Observation of tau neutrino interactions*, *Phys. Lett. B* **504** (2001) 218–224, [hep-ex/0012035].

[68] ATLAS collaboration, G. Aad et al., *Observation of a new particle in the search for the Standard Model Higgs boson with the ATLAS detector at the LHC*, *Phys. Lett. B* **716** (2012) 1–29, [1207.7214].

[69] CMS collaboration, S. Chatrchyan et al., *Observation of a New Boson at a Mass of 125 GeV with the CMS Experiment at the LHC*, *Phys. Lett. B* **716** (2012) 30–61, [1207.7235].

[70] J. S. Schwinger, *Quantum electrodynamics. I A covariant formulation*, *Phys. Rev.* **74** (1948) 1439.

[71] K. G. Wilson, *Confinement of Quarks*, *Phys. Rev. D* **10** (1974) 2445–2459.

[72] M. E. Peskin and D. V. Schroeder, *An Introduction to quantum field theory*. Addison-Wesley, Reading, USA, 1995.

[73] L. H. Ryder, *QUANTUM FIELD THEORY*. Cambridge University Press, 6, 1996.

[74] C. G. Bollini and J. J. Giambiagi, *Dimensional Renormalization: The Number of Dimensions as a Regularizing Parameter*, *Nuovo Cim. B* **12** (1972) 20–26.

[75] G. 't Hooft and M. J. G. Veltman, *Regularization and Renormalization of Gauge Fields*, *Nucl. Phys. B* **44** (1972) 189–213.

[76] T. Kinoshita, *Mass singularities of Feynman amplitudes*, *J. Math. Phys.* **3** (1962) 650–677.

[77] T. D. Lee and M. Nauenberg, *Degenerate Systems and Mass Singularities*, *Phys. Rev.* **133** (1964) B1549–B1562.

[78] R. K. Ellis and G. Zanderighi, *Scalar one-loop integrals for QCD*, *JHEP* **02** (2008) 002, [0712.1851].

[79] G. F. R. Sborlini, D. de Florian and G. Rodrigo, *Double collinear splitting amplitudes at next-to-leading order*, *JHEP* **01** (2014) 018, [1310.6841].

[80] G. F. R. Sborlini, F. Driencourt-Mangin, R. Hernandez-Pinto and G. Rodrigo, *Four-dimensional unsubtraction from the loop-tree duality*, *JHEP* **08** (2016) 160, [1604.06699].

[81] S. Catani, T. Gleisberg, F. Krauss, G. Rodrigo and J.-C. Winter, *From loops to trees by-passing Feynman's theorem*, *JHEP* **09** (2008) 065, [0804.3170].

[82] R. P. Feynman, *Quantum theory of gravitation*, *Acta Phys. Polon.* **24** (1963) 697–722.

[83] R. P. Feynman, *CLOSED LOOP AND TREE DIAGRAMS. (TALK)*, .

[84] I. Bierenbaum, S. Catani, P. Draggiotis and G. Rodrigo, *A Tree-Loop Duality Relation at Two Loops and Beyond*, *JHEP* **10** (2010) 073, [1007.0194].

[85] I. Bierenbaum, S. Buchta, P. Draggiotis, I. Malamos and G. Rodrigo, *Tree-Loop Duality Relation beyond simple poles*, *JHEP* **03** (2013) 025, [1211.5048].

[86] K. G. Chetyrkin and F. V. Tkachov, *Integration by Parts: The Algorithm to Calculate beta Functions in 4 Loops*, *Nucl. Phys. B* **192** (1981) 159–204.

[87] A. V. Smirnov, *An Algorithm to construct Grobner bases for solving integration by parts relations*, *JHEP* **04** (2006) 026, [hep-ph/0602078].

[88] S. Buchta, G. Chachamis, P. Draggiotis, I. Malamos and G. Rodrigo, *On the singular behaviour of scattering amplitudes in quantum field theory*, *JHEP* **11** (2014) 014, [1405.7850].

[89] G. F. Sterman, *Mass Divergences in Annihilation Processes. 1. Origin and Nature of Divergences in Cut Vacuum Polarization Diagrams*, *Phys. Rev. D* **17** (1978) 2773.

[90] S. Mandelstam, *Unitarity Condition Below Physical Thresholds in the Normal and Anomalous Cases*, *Phys. Rev. Lett.* **4** (1960) 84–87.

[91] H. Rechenberg and E. C. G. Sudarshan, *Analyticity in quantum field theory. 1. The triangle graph revisited*, *Nuovo Cim. A* **12** (1972) 541–568.

[92] G. F. R. Sborlini, D. de Florian and G. Rodrigo, *Triple collinear splitting functions at NLO for scattering processes with photons*, *JHEP* **10** (2014) 161, [1408.4821].

[93] R. J. Hernandez-Pinto, G. F. R. Sborlini and G. Rodrigo, *Towards gauge theories in four dimensions*, *JHEP* **02** (2016) 044, [1506.04617].

[94] S. Buchta, G. Chachamis, P. Draggiotis and G. Rodrigo, *Numerical implementation of the loop–tree duality method*, *Eur. Phys. J. C* **77** (2017) 274, [1510.00187].

[95] S. Buchta, *Theoretical foundations and applications of the Loop-Tree Duality in Quantum Field Theories*. PhD thesis, Valencia U., IFIC, 2015. 1509.07167.

[96] G. F. R. Sborlini, F. Driencourt-Mangin and G. Rodrigo, *Four-dimensional unsubtraction with massive particles*, *JHEP* **10** (2016) 162, [1608.01584].

[97] F. Driencourt-Mangin, *Four-dimensional representation of scattering amplitudes and physical observables through the application of the Loop-Tree Duality theorem*. PhD thesis, U. Valencia (main), 2019. 1907.12450.

[98] T. Hahn and M. Perez-Victoria, *Automatized one loop calculations in four-dimensions and D-dimensions*, *Comput. Phys. Commun.* **118** (1999) 153–165, [hep-ph/9807565].

[99] S. Borowka, G. Heinrich, S. P. Jones, M. Kerner, J. Schlenk and T. Zirke, *SecDec-3.0: numerical evaluation of multi-scale integrals beyond one loop*, *Comput. Phys. Commun.* **196** (2015) 470–491, [1502.06595].

[100] S. Becker, C. Reuschle and S. Weinzierl, *Numerical NLO QCD calculations*, *JHEP* **12** (2010) 013, [1010.4187].

[101] F. Driencourt-Mangin, G. Rodrigo and G. F. R. Sborlini, *Universal dual amplitudes and asymptotic expansions for $gg \to H$ and $H \to \gamma\gamma$ in four dimensions*, *Eur. Phys. J. C* **78** (2018) 231, [1702.07581].

[102] F. Driencourt-Mangin, G. Rodrigo, G. F. R. Sborlini and W. J. Torres Bobadilla, *Universal four-dimensional representation of $H \to \gamma\gamma$ at two loops through the Loop-Tree Duality*, *JHEP* **02** (2019) 143, [1901.09853].

[103] J. Plenter, *Asymptotic Expansions Through the Loop-Tree Duality*, *Acta Phys. Polon. B* **50** (2019) 1983–1992.

[104] J. Plenter and G. Rodrigo, *Asymptotic expansions through the loop-tree duality*, *Eur. Phys. J. C* **81** (2021) 320, [2005.02119].

[105] G. Rodrigo, S. Catani, T. Gleisberg, F. Krauss and J.-C. Winter, *From multileg loops to trees (by-passing Feynman's Tree Theorem)*, *Nucl. Phys. B Proc. Suppl.* **183** (2008) 262–267, [0807.0531].

[106] J. L. Jurado, G. Rodrigo and W. J. Torres Bobadilla, *From Jacobi off-shell currents to integral relations*, *JHEP* **12** (2017) 122, [1710.11010].

[107] F. Driencourt-Mangin, G. Rodrigo, G. F. R. Sborlini and W. J. Torres Bobadilla, *Interplay between the loop-tree duality and helicity amplitudes*, *Phys. Rev. D* **105** (2022) 016012, [1911.11125].

[108] R. M. Prisco and F. Tramontano, *Dual subtractions*, *JHEP* **06** (2021) 089, [2012.05012].

[109] R. Runkel, Z. Szőr, J. P. Vesga and S. Weinzierl, *Causality and loop-tree duality at higher loops*, *Phys. Rev. Lett.* **122** (2019) 111603, [1902.02135].

[110] R. Runkel, Z. Szőr, J. P. Vesga and S. Weinzierl, *Integrands of loop amplitudes within loop-tree duality*, *Phys. Rev. D* **101** (2020) 116014, [1906.02218].

[111] Z. Capatti, V. Hirschi, D. Kermanschah and B. Ruijl, *Loop-Tree Duality for Multiloop Numerical Integration*, *Phys. Rev. Lett.* **123** (2019) 151602, [1906.06138].

[112] Z. Capatti, V. Hirschi, D. Kermanschah, A. Pelloni and B. Ruijl, *Numerical Loop-Tree Duality: contour deformation and subtraction*, *JHEP* **04** (2020) 096, [1912.09291].

[113] J. J. Aguilera-Verdugo, R. J. Hernandez-Pinto, G. Rodrigo, G. F. R. Sborlini and W. J. Torres Bobadilla, *Causal representation of multi-loop Feynman integrands within the loop-tree duality*, *JHEP* **01** (2021) 069, [2006.11217].

[114] P. Nogueira, *Automatic Feynman graph generation*, *J. Comput. Phys.* **105** (1993) 279–289.

[115] A. von Manteuffel and R. M. Schabinger, *A novel approach to integration by parts reduction*, *Phys. Lett. B* **744** (2015) 101–104, [1406.4513].

[116] T. Peraro, *Scattering amplitudes over finite fields and multivariate functional reconstruction*, *JHEP* **12** (2016) 030, [1608.01902].

[117] T. Peraro, *FiniteFlow: multivariate functional reconstruction using finite fields and dataflow graphs*, *JHEP* **07** (2019) 031, [1905.08019].

[118] J. Jesús Aguilera-Verdugo, R. J. Hernández-Pinto, G. Rodrigo, G. F. R. Sborlini and W. J. Torres Bobadilla, *Mathematical properties of nested residues and their application to multi-loop scattering amplitudes*, *JHEP* **02** (2021) 112, [2010.12971].

[119] R. P. Feynman, *Simulating physics with computers*, *Int. J. Theor. Phys.* **21** (1982) 467–488.

[120] L. K. Grover, *Quantum mechanics helps in searching for a needle in a haystack*, *Phys. Rev. Lett.* **79** (1997) 325–328, [quant-ph/9706033].

[121] P. W. Shor, *Polynomial time algorithms for prime factorization and discrete logarithms on a quantum computer*, *SIAM J. Sci. Statist. Comput.* **26** (1997) 1484, [quant-ph/9508027].

[122] B. Apolloni, C. Carvalho and D. de Falco, *Quantum stochastic optimization*, *Stochastic Processes and their Applications* **33** (1989) 233–244.

[123] T. Kadowaki and H. Nishimori, *Quantum annealing in the transverse ising model*, *Phys. Rev. E* **58** (Nov, 1998) 5355–5363.

[124] J. Liu and Y. Xin, *Quantum simulation of quantum field theories as quantum chemistry*, *JHEP* **12** (2020) 011, [2004.13234].

[125] J. E. Lynn, I. Tews, S. Gandolfi and A. Lovato, *Quantum Monte Carlo Methods in Nuclear Physics: Recent Advances*, *Ann. Rev. Nucl. Part. Sci.* **69** (2019) 279–305, [1901.04868].

[126] E. T. Holland, K. A. Wendt, K. Kravvaris, X. Wu, W. Erich Ormand, J. L. DuBois et al., *Optimal Control for the Quantum Simulation of Nuclear Dynamics*, *Phys. Rev. A* **101** (2020) 062307, [1908.08222].

[127] R. Orús, S. Mugel and E. Lizaso, *Quantum computing for finance: Overview and prospects*, *Reviews in Physics* **4** (2019) 100028.

[128] A. Y. Wei, P. Naik, A. W. Harrow and J. Thaler, *Quantum Algorithms for Jet Clustering*, *Phys. Rev. D* **101** (2020) 094015, [1908.08949].

[129] D. Pires, P. Bargassa, J. a. Seixas and Y. Omar, *A Digital Quantum Algorithm for Jet Clustering in High-Energy Physics*, 2101.05618.

[130] D. Pires, Y. Omar and J. a. Seixas, *Adiabatic Quantum Algorithm for Multijet Clustering in High Energy Physics*, 2012.14514.

[131] J. J. M. de Lejarza, L. Cieri and G. Rodrigo, *Quantum clustering and jet reconstruction at the LHC*, *Phys. Rev. D* **106** (2022) 036021, [2204.06496].

[132] J. a. Barata and C. A. Salgado, *A quantum strategy to compute the jet quenching parameter $\hat{q}$*, *Eur. Phys. J. C* **81** (2021) 862, [2104.04661].

[133] J. a. Barata, X. Du, M. Li, W. Qian and C. A. Salgado, *Medium induced jet broadening in a quantum computer*, *Phys. Rev. D* **106** (2022) 074013, [2208.06750].

[134] A. Pérez-Salinas, J. Cruz-Martinez, A. A. Alhajri and S. Carrazza, *Determining the proton content with a quantum computer*, *Phys. Rev. D* **103** (2021) 034027, [2011.13934].

[135] C. W. Bauer, W. A. de Jong, B. Nachman and D. Provasoli, *Quantum Algorithm for High Energy Physics Simulations*, *Phys. Rev. Lett.* **126** (2021) 062001, [1904.03196].

[136] C. W. Bauer, M. Freytsis and B. Nachman, *Simulating Collider Physics on Quantum Computers Using Effective Field Theories*, *Phys. Rev. Lett.* **127** (2021) 212001, [2102.05044].

[137] W. A. De Jong, M. Metcalf, J. Mulligan, M. Płoskoń, F. Ringer and X. Yao, *Quantum simulation of open quantum systems in heavy-ion collisions*, *Phys. Rev. D* **104** (2021) 051501, [2010.03571].

[138] W. Guan, G. Perdue, A. Pesah, M. Schuld, K. Terashi, S. Vallecorsa et al., *Quantum Machine Learning in High Energy Physics*, *Mach. Learn. Sci. Tech.* **2** (2021) 011003, [2005.08582].

[139] S. L. Wu et al., *Application of quantum machine learning using the quantum variational classifier method to high energy physics analysis at the LHC on IBM quantum computer simulator and hardware with 10 qubits*, *J. Phys. G* **48** (2021) 125003, [2012.11560].

[140] T. Felser, M. Trenti, L. Sestini, A. Gianelle, D. Zuliani, D. Lucchesi et al., *Quantum-inspired machine learning on high-energy physics data*, *npj Quantum Inf.* **7** (2021) 111, [2004.13747].

[141] S. P. Jordan, K. S. M. Lee and J. Preskill, *Quantum Algorithms for Quantum Field Theories*, *Science* **336** (2012) 1130–1133, [1111.3633].

[142] M. C. Bañuls et al., *Simulating Lattice Gauge Theories within Quantum Technologies*, *Eur. Phys. J. D* **74** (2020) 165, [1911.00003].

[143] E. Zohar, J. I. Cirac and B. Reznik, *Quantum Simulations of Lattice Gauge Theories using Ultracold Atoms in Optical Lattices*, *Rept. Prog. Phys.* **79** (2016) 014401, [1503.02312].

[144] T. Byrnes and Y. Yamamoto, *Simulating lattice gauge theories on a quantum computer*, *Phys. Rev. A* **73** (2006) 022328, [quant-ph/0510027].

[145] R. R. Ferguson, L. Dellantonio, K. Jansen, A. A. Balushi, W. Dür and C. A. Muschik, *Measurement-Based Variational Quantum Eigensolver*, *Phys. Rev. Lett.* **126** (2021) 220501, [2010.13940].

[146] A. Kan, L. Funcke, S. Kühn, L. Dellantonio, J. Zhang, J. F. Haase et al., *Investigating a (3+1)D topological θ-term in the Hamiltonian formulation of lattice gauge theories for quantum and classical simulations*, *Phys. Rev. D* **104** (2021) 034504, [2105.06019].

[147] K. Bepari, S. Malik, M. Spannowsky and S. Williams, *Towards a quantum computing algorithm for helicity amplitudes and parton showers*, *Phys. Rev. D* **103** (2021) 076020, [2010.00046].

[148] G. Agliardi, M. Grossi, M. Pellen and E. Prati, *Quantum integration of elementary particle processes*, *Phys. Lett. B* **832** (2022) 137228, [2201.01547].

[149] C. Squires, S. Magliacane, K. Greenewald, D. Katz, M. Kocaoglu and K. Shanmugam, *Active structure learning of causal dags via directed clique trees*, in *Advances in Neural Information Processing Systems* (H. Larochelle, M. Ranzato, R. Hadsell, M. Balcan and H. Lin, eds.), vol. 33, pp. 21500–21511, Curran Associates, Inc., 2020.

[150] G. Chiribella, G. M. D'Ariano and P. Perinotti, *Theoretical framework for quantum networks*, *Phys. Rev. A* **80** (Aug, 2009) 022339.

[151] S. Even, *Graph Algorithms*. Cambridge University Press, 2 ed., 2011. 10.1017/CBO9781139015165.

[152] M. Boyer, G. Brassard, P. Hoyer and A. Tapp, *Tight bounds on quantum searching*, *Fortsch. Phys.* **46** (1998) 493–506, [quant-ph/9605034].

[153] G. Brassard and P. Hoyer, *An Exact quantum polynomial- time algorithm for Simon's problem*, in *5th Israeli Symposium on Theory of Computing and Systems (ISTCS 97)*, 4, 1997. quant-ph/9704027.

[154] L. K. Grover, *Quantum computers can search rapidly by using almost any transformation*, *Phys. Rev. Lett.* **80** (1998) 4329–4332, [quant-ph/9712011].

[155] G. Brassard, P. Hoyer and A. Tapp, *Quantum algorithm for the collision problem*, quant-ph/9705002.

[156] L. K. Grover and J. Radhakrishnan, *Is partial quantum search of a database any easier?*, in *Proceedings of the seventeenth annual ACM symposium on Parallelism in algorithms and architectures*, pp. 186–194, 2005.

[157] W. J. Torres Bobadilla, *Loop-tree duality from vertices and edges*, *JHEP* **04** (2021) 183, [2102.05048].

[158] G. F. R. Sborlini, *Geometrical approach to causality in multiloop amplitudes*, *Phys. Rev. D* **104** (2021) 036014, [2102.05062].

[159] G. F. R. Sborlini, *Geometry and causality for efficient multiloop representations*, in *15th International Symposium on Radiative Corrections: Applications of Quantum Field Theory to Phenomenology AND LoopFest XIX: Workshop on Radiative Corrections for the LHC and Future Colliders*, 9, 2021. 2109.07808.

[160] M. A. Nielsen and I. L. Chuang, *Quantum Computation and Quantum Information: 10th Anniversary Edition*. Cambridge University Press, 2010. 10.1017/CBO9780511976667.

[161] R. Alonso, A. Arias, P. Coca, F. Díez, A. García and L. Meijueiro, *Qute: Quantum computing simulation platform*, Oct., 2021. 10.5281/zenodo.5561050.

[162] T. Satoh, Y. Ohkura and R. Van Meter, *Subdivided phase oracle for nisq search algorithms*, *IEEE Transactions on Quantum Engineering* **1** (2020) 1–15.

[163] Y. Wang and P. S. Krstic, *Prospect of using grover's search in the noisy-intermediate-scale quantum-computer era*, *Phys. Rev. A* **102** (Oct, 2020) 042609.

[164] K. Zhang, P. Rao, K. Yu, H. Lim and V. Korepin, *Implementation of efficient quantum search algorithms on nisq computers*, *Quantum Information Processing* **20** (2021) 1–27.